STRUCTURE AND PROPERTIES OF INCOMMENSURATE AND COMMENSURATE PHASES OF GRAPHENE ON SIC(0001)

A Dissertation
Presented to
The Academic Faculty

By

Matthew D. Conrad

In Partial Fulfillment
of the Requirements for the Degree
Doctor of Philosophy in the
School of Georgia Institute of Technology

Georgia Institute of Technology

August 2017

STRUCTURE AND PROPERTIES OF INCOMMENSURATE AND COMMENSURATE PHASES OF GRAPHENE ON SIC(0001)

Approved by:

Dr. Edward Conrad, Advisor
School of Physics
Georgia Institute of Technology

Dr. Phillip N. First
School of Physics
Georgia Institute of Technology

Dr. Zhigang Jiang
School of Physics
Georgia Institute of Technology

Dr. Martin Mourigal
School of Physics
Georgia Institute of Technology

Dr. Thomas Orlando
School of Chemistry and Biochemistry
Georgia Institute of Technology

Date Approved: May 8, 2017

To Christina

ACKNOWLEDGEMENTS

My deepest appreciation is for my wife, Christina. Her support, patience, sacrifice and clarity of mind is more than I could have asked for. I would also like to acknowledge the support from parents, Karen and David, and my sister Rebecca throughout my life.

My PhD program begin with countless hours of study and I am thankful for the many discussions with my peers Jean-Philipe Turmaud, Stephen Spitz, Simon Berman, Benedikt Brandt, and Oliver Pierson as well as my professors Dr. Andrew Zangwill, Dr. Brian Kennedy, Dr. Shina Tan, Dr. Alberto Fernandez-Nieves, and Dr. Roman Grigoriev. As I entered my research, I greatly benefitted from the knowledge and training from Dr. Feng Wang, Dr. James Palmer, Dr. Meredith Nevius, Dr. Yuntao Li, Dr. Maya Nair, Dr. Arlensiú Celis. I appreciate Dr. Walter de Heer and Dr. Claire Berger for facilitating use of the characterization tools in the Keck Lab. I am thankful for all the members of the IEN staff who trained and maintained the characterization and processing tools. I greatly benefitted from conversations with regarding my computational studies with Dr. Yan Kunc, Dr. Angelo Bongiorno, Dr. Markus Kindermann and Dr. Mei-Yin Chou. Dr. Paul Miceli, Dr. Alessandro Coati, Dr. Yves Garreau, Dr. Alina Vlad, Dr. Antonio Tejeda, Dr. Amina Taleb-Ibrahimi, Dr. Julien Rault, and Dr. Jean-Pascal Reuff were indispensible in my experimental analysis and modeling. I would also like to express my gratitude to my thesis committee members, Dr. Martin Mourigal for his discussions on incommensurate systems, Dr. Phillip First for his course lectures and many helpful discussions, Dr. Zhigang Jiang for his feedback on my research presentations and Dr. Thomas Orlando for his collaboration in some experiments early on in my research.

Finally, I would like to acknowledge my advisor Dr. Edward Conrad. I am grateful for the liberty he provided to me to pursue the topic of my interest and to pursue computational studies in addition to our experiments. He was an excellent example of mentorship that I will take forward in my future research efforts.

TABLE OF CONTENTS

LIST OF TABLES

LIST OF FIGURES

SUMMARY

Realizing a technologically relevant graphene semiconductor has been one of the key challenges for advancing graphene electronics. Recently, a semiconducting form of graphene was discovered in the first graphene layer that grows on SiC, often called the "buffer layer." Its semiconductor character has been attributed to functionalization through sp^3 bonding to the SiC interface. As such, the buffer layer is the only known highly ordered functionalized graphene system and it has correspondingly gone from being a "dead layer" and a nuisance in the production of monolayer graphene to one of the most important examples of functionalized graphene. However, the mechanism (bonding geometry, strain, confinement, etc.) causing the buffer layer's semiconducting properties has remained elusive due to the dual challenge of a large, computationally demanding, interface structure and the experimental difficulty of uniform buffer layer growth. In this thesis I present the first surface x-ray diffraction (SXRD) measurements of the interface structure using improved buffer growth conditions. SXRD measurements reveal a new interface system with an incommensurate mutual modulation of the graphene and SiC interface. For the first time, electronic structure calculations using the SXRD derived interface structure provide an explanation for the semiconducting buffer. The structure of the buffer layer and SiC interface is investigated further through a combined x-ray standing wave (XSW) and x-ray reflectivity (XRR) analysis to reveal possible origins of the incommensurate structure resulting from a depleted Si interface. Additionally, I compare films (buffer only and buffer+monolayer) formed under different growth conditions. This work demonstrates that the properties of the buffer layer are malleable. These results indicate that controlling the buffer layer interface produces a viable platform for graphene band gap engineering and paves the way for advancing graphene electronics.

CHAPTER 1
INTRODUCTION AND BACKGROUND

Graphene was one of the first truly two dimensional materials and has received extensive interest for the past decade due to its record setting electron mobility and unique electronic structure [1, 2, 3, 4]. For the physicist, graphene serves as a way to investigate quantum electrodynamics in a condensed matter system because its low energy excitations resemble those of massless Dirac fermions. For the engineer, graphene holds the promise of many technological applications, especially in electronics. Towards this goal, a semiconducting form of graphene is essential. To understand the route towards producing a graphene semiconductor, this section reviews the real space and electronic structure of graphene, band gap formation in graphene, graphene growth from SiC and a review of what's known regarding the initial phases of graphene growth on SiC.

1.1 Graphene

Graphene is a planar two-dimensional hexagonal crystal of carbon atoms [see Figure 1.1(a)]. The positions of the atoms are described by lattice and basis vectors, $\mathbf{R} = \mathbf{R}_{m,n} + \mathbf{R}_B$. The lattice positions are determined by integer multiples of the lattice vectors, $\mathbf{R}_{m,n} = m\mathbf{a} + n\mathbf{b}$, where it is my convention for the lattice vectors to be rotated from one another by 120°, as opposed to 60°. The magnitude of $\mathbf{a}$ and $\mathbf{b}$ are equal and define the graphene lattice parameter, a_g. For the orientation shown in Figure 1.1(a) the lattice vectors are,

$$\mathbf{a} = a_g \left(\frac{1}{2}, \frac{\sqrt{3}}{2} \right) ; \quad \mathbf{b} = a_g \left(\frac{1}{2}, -\frac{\sqrt{3}}{2} \right) . \tag{1.1}$$

The honeycomb structure is formed by having two equivalent basis atoms. The "A" atom is located at the origin and the "B" atom at $\mathbf{R}_B = 1/3\,(\mathbf{a} - \mathbf{b}) = a_c(0, 1)$, where $a_c =$

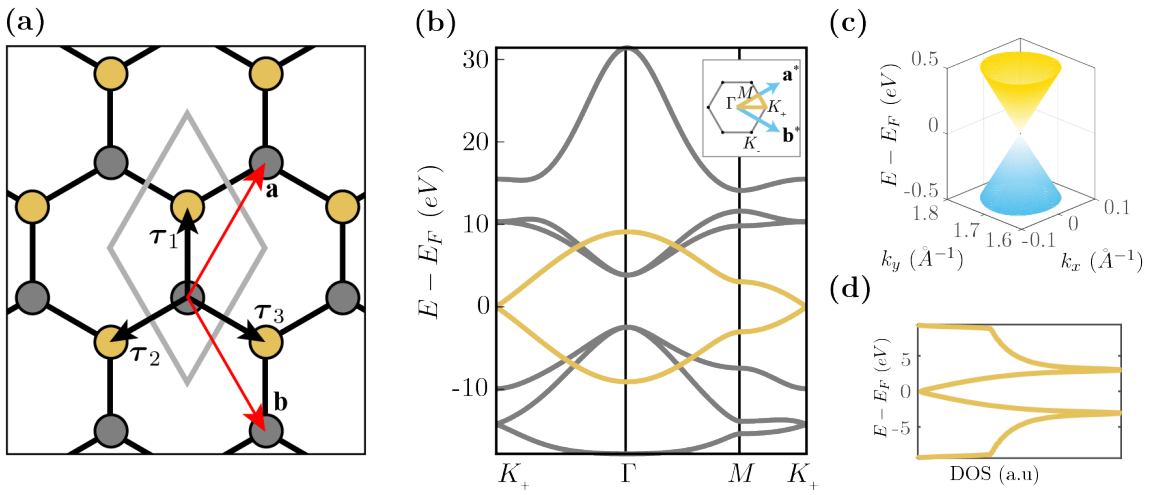

Figure 1.1: (a) Atomic structure of graphene. The gray diamond represents the unit cell. "A" ("B") atoms are in gray (gold). The red arrows represent the lattice vectors. Black arrows represent the vectors for the three nearest neighbors to an A atom. (b) Band structure of graphene π-bands (yellow) and σ-bands (gray) calculated from the tight binding method in ref. [5]. The two π-bands touch at the K_+-point(and K_-) with a linear dispersion that gives rise to a Dirac cone shown in (c). The insert is a schematic of reciprocal space. The reciprocal lattice vectors in blue, $\mathbf{a}^*$ and $\mathbf{b}^*$, are determined from the lattice vectors in (a), $\mathbf{a}$ and $\mathbf{b}$, respectively. The boundary of the first Brillouin zone is indicated by the gray hexagon. The band structure was calculated along the path shown in yellow. (d) Density of states of graphene π-bands.

$a_g/\sqrt{3} \approx 1.42$ Å is the graphene bond length. Since an accurate knowledge of a_g is important for measuring various quantities such as strain, this thesis will spend some time addressing the value of a_g. a_g is often assumed to be the lattice constant of graphite (2.460±0.002 Å) [6, 7, 8, 9]. However, interplanar interactions are known to affect the lattice parameter of layered systems [10]. Furthermore, no truly isolated graphene sheet exists and therefore a_g has never been measured. An isolated graphene sheet only exists in theory and can only have a theoretical lattice constant. The theoretically isolated lattice parameter for graphene obtained from results in the literature is (2.453±0.004) [11, 12, 13]. This value is smaller than the graphite lattice parameter. This is expected since interplanar interactions are known to increase the lattice constant [10].

The reciprocal lattice of graphene is also hexagonal where $\mathbf{a}^*$ and $\mathbf{b}^*$ are determined by the relations $\mathbf{a} \cdot \mathbf{a}^* = 2\pi$, $\mathbf{a} \cdot \mathbf{b}^* = 0$, $\mathbf{b} \cdot \mathbf{b}^* = 2\pi$, $\mathbf{b} \cdot \mathbf{a}^* = 0$. The result is that $\mathbf{a}^*$ and $\mathbf{b}^*$ are rotated from one another by 60° as opposed to 120°. A schematic of the reciprocal lattice is shown in Figure 1.1(b). The magnitude of the primitive reciprocal lattice vectors is $4\pi/a_g\sqrt{3}$. There are four symmetry points of interest in the Brillouin Zone (BZ) of graphene: $\Gamma = 0$, $M = 1/2\mathbf{a}^*$, $K_\pm = \pm 1/3(\mathbf{a}^* + \mathbf{b}^*)$. Note that the $K_\pm$-points are distinct as an integer multiple sum of the reciprocal lattice vectors cannot connect K_+ and K_-.

In graphene, carbon atoms populate both A and B basis positions. A similar hexagonal lattice has also been applied to other elemental species such as Si [14] and P [15], molecules such as $RuCl_3$ [16], and distinct elements for A and B atoms such as MoS_2.[17] Depending on the chemical composition of the basis atoms, the properties and stability may vary substantially.

Since carbon has four valence electrons, three of the electrons in the $2s$, $2p_x$, and $2p_y$ orbitals sp^2 hybridize to form strong σ-bonds to the three neighboring carbon atoms in the hexagonal lattice. The remaining electron in the $2p_z$ state delocalizes and forms π-bonds with the neighboring carbon atoms. In perfectly flat graphene the π-bonds can be considered separately because they are orthogonal to the σ-bonds. Furthermore, the π-electrons

are responsible for the low energy electronic structure and were first studied theoretically using the tight binding method to serve as a building block for understanding the electronic properties of graphite [18]. Despite its simplicity, the tight binding (TB) model predicts experimental results [19] and agrees with more rigorous ab initio calculations [20]. For this reason, TB models are often the starting point for exploring new phenomena in the electronic structure of graphene systems.

The electronic structure of the graphene π-bands and σ-bands are shown in Figure 1.1(b) and calculated by the nearest neighbor formalism in ref. [5] and [21]. The electronic structure of the π-bands was originally calculated by Wallace [18] and has the analytical form,

$$E_{\pm} = \frac{\varepsilon_{2p} \pm t|f(\mathbf{k})|}{1 \pm s_o|f(\mathbf{k})|}, \tag{1.2}$$

where ε_{2p} is the energy of the $2p_z$ orbital. Often, energy is referenced to this energy by setting $\varepsilon_{2p} = 0$. $t = -3.03$ eV is the hopping parameter, s_o is the orbital overlap and $f(\mathbf{K}) = \sum_{i=1}^{3} e^{i\mathbf{k}\cdot\boldsymbol{\tau}_i}$ is the phase factor describing nearest neighbor hopping, where nearest neighbor vectors $\boldsymbol{\tau}_i$ are shown in Figure 1.1(a). At low energy, the band structure of the π-electrons has two bands (bonding and anti-bonding) that touch at the $K_{\pm}$-points with linear dispersion and azimuthal symmetry [See Figure 1.1(b) and (c)]. This can be seen by noting that $f(\mathbf{K}_{\pm}) = 0$ and expanding equation 1.2 about the K-points. Defining the momentum as $\mathbf{p} = \hbar(\mathbf{k} - \mathbf{K}) = |\mathbf{p}|(\xi\cos\varphi, \sin\varphi, 0)$, where $\xi = \pm 1$ for the bonding and antibonding bands and φ is the polar angle of momentum in the plane, the effective Dirac-like Hamiltonian near $K_{\pm}$ is $H_e = v_F\mathbf{p}\cdot\boldsymbol{\sigma}$, where $\boldsymbol{\sigma}$ is the Pauli spin matrices. The energy dispersion around $K_{\pm}$ is $E = v_f|\mathbf{p}|$, where $v_F = -\sqrt{3}a_g t/(2\hbar) \approx c/300$ and c is the speed of light. The wave function in this approximation is,

$$\psi = \frac{1}{\sqrt{2}} \begin{pmatrix} 1 \\ \pm\xi e^{i\xi\varphi} \end{pmatrix} e^{i\mathbf{p}\cdot\mathbf{r}/\hbar}. \tag{1.3}$$

.

Determination of the Fermi level, E_F, which is at $E - E_F = 0$ in Figure 1.1(b), for a charge neutral scenario at 0 K results in a complete filling of the bonding π-band. Also, because of the linear dispersion, the density of states reaches its minimum at the charge neutrality point. The culmination of these effects results in the electronic structure classification of graphene as a semimetal. Although the band dispersion is the same at $K_{\pm}$-points, pseudospin arises from the inequivalence of the wave functions at $K_{\pm}$-points. The wave functions are also chiral, i.e. dependent on the momentum direction, which produces a backscattering probability of zero. The presence of linear dispersion and pseudospin at low energy indicate that the quasiparticles in graphene behave like massless Dirac fermions [3]. As such, the shape of the low energy dispersion is characterized by a Dirac cone and the two bands touch at the Dirac point [see Figure 1.1(c)].

1.2 Band Gap Formation in Graphene

The reason for this unique zero gap electronic structure in graphene is due to sublattice symmetry, i.e. both A and B atoms are carbon, and hexagonal symmetry. The combination of these symmetries ensures a degeneracy in energy at the $K_{\pm}$-points [5]. As such, the methods for producing band gaps in graphene involve breaking either or both of these symmetries. Symmetry-breaking methods fall into three broad classes: quantum confinement, strain and functionalization.

1.2.1 Quantum Confinement

Theoretically, breaking translational symmetry by defining graphene into certain shapes of sufficiently small size may induce band gaps. Two notable examples are nanoribbons [22] and antidots [23]. Both quantum confinement and edge termination play important roles in these systems. Figure 1.2 demonstrates the effects of quantum confinement for "armchair" graphene nanoribbons. There are two principal types of graphene nanoribbons classified by their edge termination as armchair or zig zag. For zig zag ribbons, conductive edge states

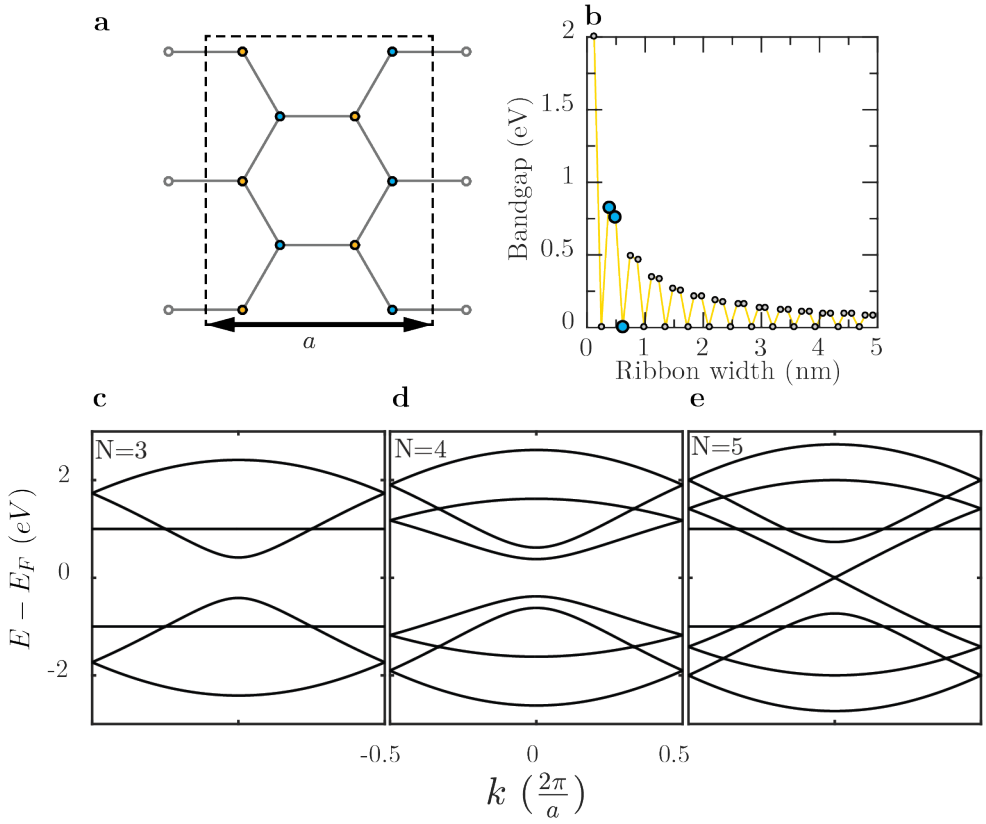

Figure 1.2: Band gap formation from quantum confinement in armchair graphene nanoribbons. Calculation of the electronic structure follows ref. [22]. (a) Armchair nanoribbon atomic structure for $N = 5$, where N is the number of horizontal atomic planes. The dashed rectangle represents the unit cell of lattice constant $a = \sqrt{3}a_g$. A (B) atoms are represented by yellow (blue) circles. (b) Band gap dependence on ribbon width. (c)-(e) example tight binding band structures for $N = 3 - 5$, respectively. The band gaps for these structures are highlighted by the blue circles in (b).

are predicted. While interesting in its own right, band gaps are not predicted for zig zag ribbons in the tight binding formulation [22]. However, ab initio calculations suggest that zig zag ribbons will have a small band gap based on edge termination [24]. For armchair ribbons, there are three ribbon classes based on the ribbon width [see Figure 1.2(c)-(e)] that produce band gaps of different size. One of the classes actually predicts a gapless state, though ab initio calculations predict a small gap [25].

Producing a gapped form of graphene from quantum confinement has two possibly insurmountable challenges. The ribbon width must first be small as well as crystallographically aligned. Figure 1.2(b) shows that the size of the band gap is inversely proportional to the ribbon width and substantial band gaps occur only when the width is on the order of a few nanometers. This is beyond most current lithography limits. Furthermore, edge disorder and deviations from a purely armchair direction do not lead to band gaps. Earlier transport measurements from lithographically patterned graphene found a transport gap, as opposed to a true band gap, due to ribbon disorder [26, 27].

1.2.2 Strain

Application of strain to the graphene lattice breaks hexagonal symmetry. Breaking the hexagonal symmetry will change the phase terms from nearest neighbor hopping such that $f(K_{\pm}) \neq 0$. There are numerous types of strain that can be considered, such as uniaxial [28], Peierls [29], and local [30]. The simplest example is uniaxial strain [28]. However, to achieve large gaps requires strains beyond the elastic limit and also reduces the Fermi velocity. Peierls distortions can occur when there is a net energy reduction through an energy gain from an elastic distortion and an energy reduction from the formation of an electronic energy gap. Peierls distortions of Kekulé order are predicted to open band gaps [29]. Recent reports claim to observe Kekulé ordering through scanning tunneling microscopy (STM) of graphene films grown on copper [31]. However, they did not report a Kekulé related band gap from their measurements, indicating that the distortion was either

too small or insufficiently ordered to induce a measurable band gap. Any band gaps found could not be separated from the interaction with the Cu substrate. Other types of local strain show promise of opening gaps [30], but have yet to be realized experimentally due to similar challenges facing quantum confinement.

1.2.3 Functionalization

Functionalization through chemical modification [32], graphene multilayers [33], or substrate interaction [34, 35] can open gaps by breaking sublattice symmetry in graphene. Chemical functionalization through the introduction of atomic species such as hydrogen or nitrogen can open band gaps up to 1 eV. However, the process is inherently random and often leads to insufficiently ordered systems. Bilayer graphene is also an example of functionalization as the interlayer interactions, breaks sublattice symmetry. Substrate functionalization is well known for SiC [36] and Ruthenium [35]. In both cases, the first layer of graphene has been referred to as a buffer layer because of less developed π-bands in ARPES measurements. Due to SiC being a wide band gap semiconductor, the buffer layer of SiC lends itself more readily to technological applications. Substrate interaction holds promise for developing a semiconducting form of graphene because it combines the ability to readily produce large band gaps through functionalization with an ordered interaction. Such an ordered interaction may hold the key to creating a more coherent electronic structure that maintains the high mobility observed in nearly freestanding graphene.

1.3 Epitaxial Graphene from SiC

There are many methods for preparing graphene samples, such as exfoliation [4], chemical vapor deposition [38], and reduction of graphene oxide [39]. The similar and critical challenge faced by these methods is in the difficulty to conduct systematic and reproducible studies. From one run to the next, these methods will necessarily result in different layer number, disorder, grain size and crystallographic alignment characteristics. As a result,

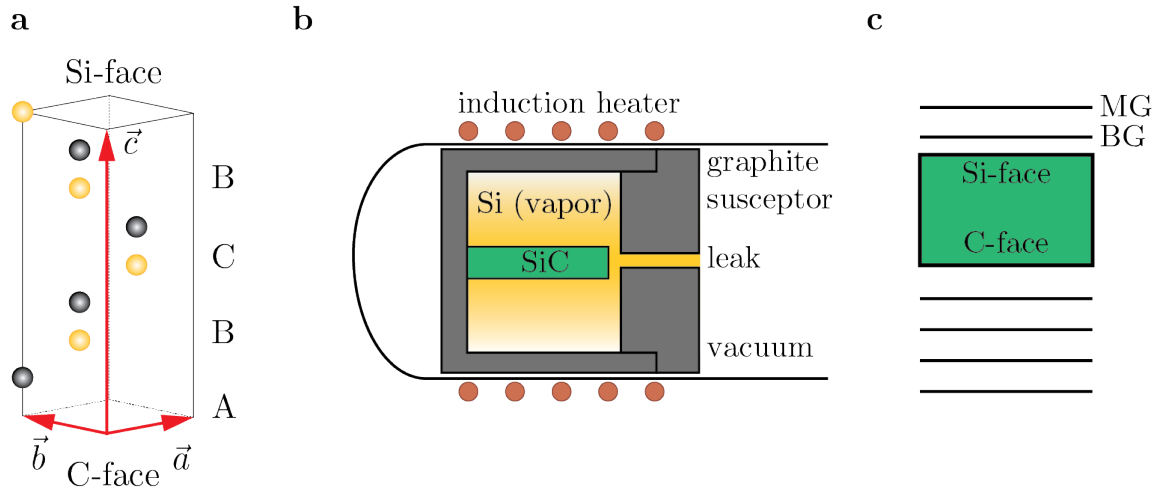

Figure 1.3: Epitaxial graphene on SiC. (a) Unit cell of 4H-SiC. Si (C) atoms are yellow (black). The graphene layer stacking sequence is ABCB on the bulk SiC(0001) surface, referred to as the Si-face because it terminates with a plane of Si atoms, conversely SiC(000$\bar{1}$) terminates with C atoms (C-face). (b) Schematic of graphene growth on SiC by confinement controlled sublimation [37]. (c) Schematic of graphene on SiC. Many layers of graphene will grow on the C-face with many commensurate rotations. Graphene growth is slower on the Si-face compared to the C-face. The first layer of graphene in the Si-face is called the buffer layer (BG), the second layer is called monolayer graphene (ML).

many advanced characterization techniques, such as Surface X-ray Diffraction, ARPES and other synchrotron based techniques are out of reach. Graphene grown from SiC, in principle, addresses these issues by producing graphene crystallographically aligned to SiC with reproducible disorder characteristics.

In 1975, Van Bommel *et al.* discovered that heating SiC to temperatures greater than 800°C caused silicon sublimation from the surface [40]. Once cooled, the subsequent excess carbon rearranged into monolayers with a graphitic lattice constant. Forty years later, graphene growth by thermal decomposition of SiC is one of the most promising growth methods for graphene based electronics [41, 37]. The appeal of epitaxial graphene, i.e. graphene grown from SiC, is that the layers are crystallographically aligned with SiC and precise layer control is possible [37].

There are many methods for growing graphene on SiC. The earliest growth methods consisted of heating in ultra high vacuum (UHV) [40, 42]. The challenge with UHV

graphene growth is that large area layer control is not possible due to high growth rates [43]. Currently, there are a few improved growth techniques such as growth in an Ar [41] or silane [44] and confinement controlled sublimation (CCS) [37].

All graphene samples studied for this thesis were produced by the CCS method. In this method, SiC is inductively heated inside a graphite enclosure [See Figure 1.3(b)]. The sublimated Si generates a partial pressure due to confinement within the enclosure. The partial Si pressure is determined by the temperature, crucible geometry and leak rate. The increased Si partial pressure slows the graphene growth process to a near equilibrium condition and causes growth to occur at higher temperatures. An important note is that the system is in *quasi*-equilibrium. This is achieved by multiple growth runs that build up Si in the crucible. The amount of Si is not entirely constant and the crucible must be conditioned from time to time to either add or remove Si. This is accomplished by an extended heating with or without a SiC sample in the crucible. For a conditioned crucible of a particular geometry, the number of layers grown is determined by the temperature and to a lesser extent, time.

Most studies of graphene growth have been on the two polar faces, the SiC(0001) Si-terminated face (Si-face) and SiC($000\bar{1}$) carbon-terminated face(C-face), of hexagonal 4H and 6H SiC [45, 36, 46]. Note that graphene growth also occurs on other faces [47, 48] and polytypes such as cubic β-SiC(111) [49]. The crystal structure of 4H-SiC is shown in Figure 1.3(a). Growth on the C-face and Si-face are quite different. On the C-face growth occurs more quickly and > 30 layers are possible with many commensurate rotations between the graphene layers [50, 51]. On the Si-face, growth is slower and only a few layers of graphene form [19]. Furthermore, the graphene layers are rotationally aligned with the SiC to form the so-called $(6\sqrt{3}\times 6\sqrt{3})_{\text{SiC}}\text{R}30^\circ$ reconstruction and ABC stacked [46, 19].

This thesis focuses on Si-face graphene growth. With the current crucible design, the first layer of graphene grown on the Si-face, commonly referred to as the buffer layer (BG_o), grows at 1400°C and the second layer (ML) grows at 1550°C [See Figure 1.3(c)].

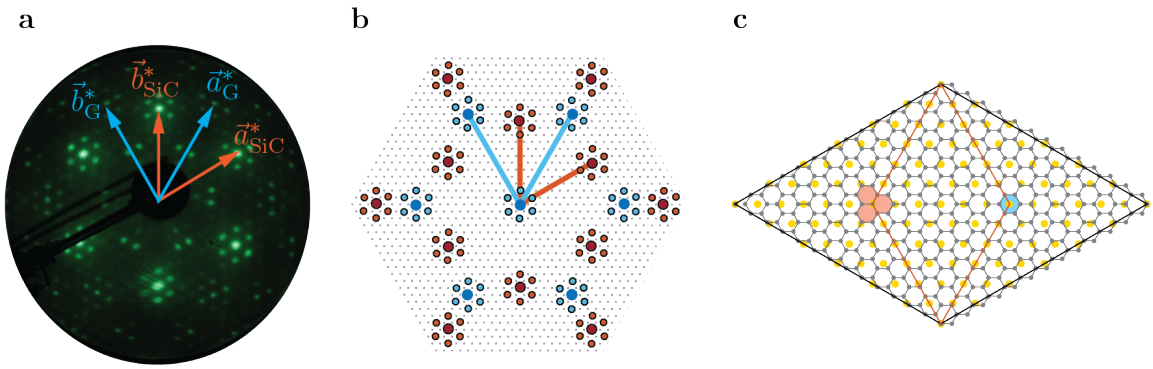

Figure 1.4: The $(6\sqrt{3}\times 6\sqrt{3})_{\mathrm{SiC}}$R30° reconstruction on SiC(0001). (a) LEED image of a buffer layer grown by confinement controlled sublimation. (b) reciprocal space interpretation of (a). The large red (blue) circles are SiC (graphene) rods, smaller red (blue) circles are $(6\times 6)_{\mathrm{SiC}}$ satellites about SiC (graphene). The graphene rods appear to be commensurate with the $6\sqrt{3}$ reciprocal lattice (black dots). (c) Real space $6\sqrt{3}$ unit cell. The gray (yellow) circles represent carbon (Si) in the graphene (bulk-terminated SiC). The black diamond is the $6\sqrt{3}$ unit cell and the red diamond is the $(6\times 6)_{\mathrm{SiC}}$ *quasi*-unit cell. The red and blue filled hexagons emphasize that the $(6\times 6)_{\mathrm{SiC}}$ is not a true unit cell. The red (blue) hexagons demonstrate the presence (absence) of a graphene carbon atom at the boundaries of the *quasi*-unit cell.

This naming convention was adopted because the buffer layer did not possess the electronic properties of freestanding graphene due to its interaction with SiC. Only when the second graphene layer formed did angle resolved photoemission spectroscopy (ARPES) measurements observe the characteristic Dirac cone [36].

At this stage it is important to recognize that there are potentially two distinct buffer layers present, (i) the bare buffer grown at 1400° ($\mathrm{BG_o}$) and (ii) the buffer layer grown at 1550° underneath the monolayer ($\mathrm{BG_{ML}}$). Because of the different growth temperatures and increased Si desorption these two buffer layers cannot *a priori* be assumed to be the same, i.e. they may have unique SiC interface structures, bonding configurations, strains and disorder, as I will show in Chapter 3.

1.4 The Buffer Layer and SiC(0001) Interface

Because of the complex surface reconstruction and challenges in growth, the history of experimental studies of graphitization on SiC(0001) is characterized by seemingly opposed

results and remains to be fully understood. For instance, it has been contested whether the SiC interface is a $6\sqrt{3}$ or $(6\times6)_{\text{SiC}}$ reconstruction, if it is bulk-terminated [52], and if the topmost carbon layer is a full, partial or defected graphene layer [53, 54].

LEED images always suggest the presence of what appears to be a $(6\sqrt{3}\times6\sqrt{3})_{\text{SiC}}\text{R}30^\circ$ reconstruction on SiC(0001) at all stages of graphitization [40, 43, 55]. As a result, layer estimation from LEED measurements alone can be challenging and can depend on the growth procedure [43]. The buffer layer is regarded to form with the initial formation of the $6\sqrt{3}$ reconstruction and sometimes these terms are used interchangeably. A typical LEED image of the $6\sqrt{3}$ is shown in Figure 1.4(a). The graphene reciprocal lattice vectors are rotated 30° from SiC and the magnitude is $|a_{\text{g}}^*|/a_{\text{SiC}}^*| = 13/6\sqrt{3}$, i.e. $\mathbf{a}_{\text{g}}^* = 13/6(\mathbf{a}_{\text{SiC}}^* + \mathbf{b}_{\text{SiC}}^*)$. With $a_{\text{SiC}} \approx 3.08$ Å, this leads to a lattice constant, $a_g = a_{\text{SiC}}\ 6\sqrt{3}/13 = 2.462$ Å, that is only slightly (0.1%) expanded from graphite (2.460(2) Å) [7, 8, 6, 9]. Furthermore, the graphene position in reciprocal space indicates that a $(13 \times 13)_{\text{g}}$ graphene unit cell is commensurate with the $(6\sqrt{3}\times6\sqrt{3})_{\text{SiC}}\text{R}30^\circ$ unit cell. How a graphene reciprocal lattice fits onto the $6\sqrt{3}$ reciprocal lattice is shown in Figure 1.4(b) and the corresponding real space unit cell is shown in Figure 1.4(c).

In contrast to LEED, STM measurements have not produced a satisfying image of a $6\sqrt{3}$ reconstruction [43]. Most outlines of a $6\sqrt{3}$ unit cell from STM measurements break down after only a few cell repetitions. The primary STM observed reconstruction is $(6\times6)_{\text{SiC}}$ [52, 56], though early measurements suggested it may not be truly commensurate with the substrate [45]. The difference between the $6\sqrt{3}$ and $(6\times6)_{\text{SiC}}$ unit cells are demonstrated in Figure 1.4(c). The two measurements are at odds in the sense that an integer multiple of $(6\times6)_{\text{SiC}}$ reciprocal lattice vectors cannot describe the graphene position in Figure 1.4(a). $(6\times6)_{\text{SiC}}$ features are observed in LEED images as "satellites," i.e. there are diffraction rods that surround the graphene and SiC reciprocal lattice rods described by $(6\times6)_{\text{SiC}}$ reciprocal lattice vectors [See Figure 1.4(a) and (b)]. However, it should be noted that $(6\times6)_{\text{SiC}}$ satellites surrounding graphene diffraction rods lie on the $6\sqrt{3}$ reciprocal

lattice because the graphene reciprocal lattice rod is on the $6\sqrt{3}$ reciprocal lattice.

The interpretation of LEED and STM measurements remains an ongoing research question [57, 58]. One model is that the SiC is unreconstructed. In this model the satellite rods in LEED are interpreted as resulting from multiple scattering and the $(6\times6)_{\text{SiC}}$ pattern seen in STM measurements results from a moiré pattern between the SiC layer and the graphene layer. In contrast, the reconstructed model claims that the satellite rods in LEED are due to structural changes in the interface between graphene and SiC. As such, the $(6\times6)_{\text{SiC}}$ seen in STM is interpreted as imaging the interface reconstruction. Within the reconstructed model, relaxed bulk-terminated [59] and adatom [52] models have been proposed. XPS and ARPES measurements have so far supported the relaxed bulk-terminated SiC interface model due to the lack of spectroscopic evidence for adatom species [36] while STM measurements image features that appear to be adatoms in the interface beneath the graphene layers [52].

What has become clear is that the buffer layer is a complete graphene layer without substantial defects or incomplete regions. This was shown through hydrogen intercalation of the buffer layer, where the hydrogen intercalated buffer produced a band structure similar to freestanding graphene [60, 61]. As growth methods and experimental techniques have improved, the understanding of the buffer layer electronic structure has changed. Initial ARPES measurements found the buffer layer to be a wide gap insulator with two significant surface states within the gap making the buffer layer unsuitable for electronic applications [36]. Using improved growth methods, this picture changed and found the buffer layer to be a true semiconductor with no surface states and a band gap $> 0.5\ eV$[62].

It is also clear that a strong interaction is present between the buffer graphene and the SiC. XPS measurements of bare buffer surfaces measure two broad buffer related components, identified as S_1 and S_2 [36, 63]. Figure 1.5(a) shows the presence of two buffer components in the C 1s spectra. They have been attributed to graphene bonded (S_1) and graphene not bonded (S_2) to the topmost Si in the SiC interface layer. The assignment was

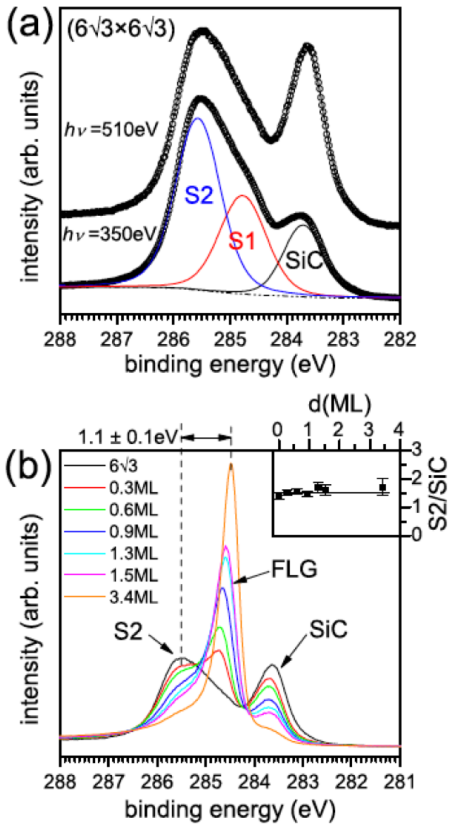

Figure 1.5: C 1s spectra of UHV grown buffer layer (a) and multilayer (b) graphene grown on SiC(0001). Figure taken from ref. [36]. (a) spectral decomposition of the buffer layer into three components; S_1 buffer carbon bonded to interface Si, S_2 buffer carbon sp^2 bonded, and SiC. (b) C 1s spectra of few layer graphene grown on SiC(0001). As the number of layers increases, the buffer contribution decreases and the monolayer graphene component shifts to lower binding energy.

based on a few observations. First, it was noticed that the σ-bands from ARPES measurements were shifted to lower binding energy compared to graphite by $\sim$1 eV. Similarly the binding energy of S_2 (285.6 eV) is roughly 1 eV lower than the binding energy of neutral graphite (284.42 ev). By taking this shift as a measure of the doping, the S_2 component was associated with sp^2 bonded carbon in the buffer layer. Furthermore, the S_2 binding energy followed the clear trend observed in the binding energy of few layer graphene. As the number of graphene layer increased, the binding energy approached the binding energy of neutral graphite [see Figure 1.5(b)]. They also observed that the ratio of the S_1 and S_2 was independent of photon energy, indicating that they were from the same layer. The fact that the intensity of S_1 and S_2 increased with a decrease in photon energy indicated that they were on the surface and not from the bulk. Their final observation was that the S_2:S_1 intensity ratio was roughly 2:1. This provided further evidence that S_2 was the buffer component not bonded to Si, even though it was at a higher binding energy than what is expected for graphite. A 2:1 ratio was relevant because the areal density of graphene is roughly 3 times larger than the Si areal density. Comparing the number of graphene and topmost Si atoms in the $6\sqrt{3}$, one obtains $N_g/N_{Si} = 2 * 13^2/(6\sqrt{3})^2 \simeq 3.13$. The S_2:S_1 ratio also suggested that nearly all of the Si in the interface were bonded and agreed with early calculations of an artificially reduced $\sqrt{3}$ unit cell [64, 65].

Although it is clear there is some strong, most likely sp^3, bonding between the buffer and interface Si, the assignment of S_1 as the C 1s component associated with the C-Si bond has been contested. More recent X-ray Standing Wave measurements asserted that S_2, instead of S_1, was the bonded component. This was based on a photoemission yield analysis that showed the S_2 component was closer to the interface than S_1 [63]. Their subsequent reflectivity analysis also reported a reduced Si concentration in the interface, which would call for a reduced number of bonds to the buffer layer.

Theoretically, the picture of the buffer layer is just as unclear. Due to the large surface reconstruction suggested by LEED, theoretical studies of graphene on SiC are limited and

remain inconclusive. Depending on the assumptions and calculation method, qualitatively different properties are predicted. Initial calculations were performed on an unrealistic bulk-terminated $\left(\sqrt{3}\times\sqrt{3}\right)_{\text{SiC}}\text{R}30^\circ$ unit cell where the graphene was highly compressed to fit a 2×2 graphene unit cell on the $\sqrt{3}$ SiC cell. The results predicted a wide gap buffer with a metallic state from Si dangling bonds [64, 65]. This seemingly agreed with initial ARPES measurements that found a wide band gap buffer with significant surface states [36]. However, this consistency was challenged when calculations of a bulk-terminated $(6\sqrt{3}\times 6\sqrt{3})_{\text{SiC}}\text{R}30^\circ$ buffer was predicted to be metallic [66]. There have also been other ab initio calculations of the $6\sqrt{3}$ buffer that claimed the results supported the insulator picture of the $(\sqrt{3}\times\sqrt{3})_{\text{SiC}}$ model[67], or remained silent on its electronic properties [68, 69]. Furthermore, it is not clear theoretically why the bulk-terminated reconstruction should be $6\sqrt{3}$ as there are other more energetically favorable interface structures, such as $(4\times 4)_{\text{SiC}}\text{R}24.2^\circ$ [69]. From all the theoretical studies conducted, none predict the most recent ARPES measurements of a semiconducting band gap >0.5 eV [62] or the gap from STS measurements of ~ 1 eV [60, 52]. It is clear that more detailed structural measurements are needed to guide further theoretical study and clarify previous experimental results.

1.5 Thesis Outline

This thesis serves to address many of the discrepancies found in the literature for the buffer layer on SiC. This was accomplished by refining the growth conditions for producing homogeneous buffer layer using CCS. The improved sample quality enabled synchrotron based studies such as angle resolved photoemission, surface x-ray diffraction, and x-ray standing wave photoemission. In Chapter 2 these characterization techniques are introduced. I will also discuss in-house characterizations that were utilized to develop an appropriate growth protocol of the buffer layer.

With improved samples in hand, the first surface x-ray diffraction measurements of the interface structure of the buffer layer are reported and discussed in Chapter 3. My results

reveal a new picture for understanding the buffer interface interaction: incommensurate mutual modulation. This concept is fleshed out and then utilized to predict the diffracted intensities. Chapter 4 develops a tight binding model for calculating the electronic band structure based off of the incommensurate mutual modulation model. The results provide excellent agreement with the experimental ARPES measurements, giving credence that the incommensurate model is responsible for the semiconducting character. Furthermore, I also address the possible contributions of strain and Kekulé distortions and show that if such distortions are present, they are small and do not significantly contribute to the buffer band structure compared to the contributions of the Si bonding to the interface.

Chapter 5 aims to gain insight into the origin of the incommensurate phase through detailed structural analysis of a buffer layer and monolayer sample using x-ray reflectivity and x-ray standing wave photoemission. This chapter builds off of previous studies and reconciles some of the discrepancies between Emery *et al.* and Emtsev *et al.* Through these studies, a vertical distribution of the buffer layer is obtained that suggests the formation of graphene islands separated by regions more strongly bonded to interface Si. The results provide consistency with predictions from incommensurate mutual modulation. A study of the SiC interface layers found a similar depleted Si interface persisted in both buffer layer and monolayer samples, indicating an interface equilibrium structure ultimately responsible for the incommensurate phase. In the closing chapter, the implications of the results are discussed and pathway forward is proposed for incorporating the buffer layer into graphene based electronics.

CHAPTER 2
EXPERIMENTAL TECHNIQUES FOR CHARACTERIZATION OF EPITAXIAL GRAPHENE ON SIC(0001)

In this Chapter, I provide an introduction to the primary characterization techniques utilized in this thesis to study the buffer layer on SiC(0001). The use of synchrotron based techniques for detailed characterization of the graphene-SiC(0001) interface is a central theme. The techniques reviewed in this chapter are Surface X-ray Diffraction (SXRD), Angle Resolved Photoemission Spectroscopy (ARPES) and X-ray Standing Wave Photoemission (XSW). While there is a substantial amount of information that can be acquired from these techniques, the results of these characterizations is of little practical use if they cannot be correlated to standard techniques such as Raman and XPS. For this reason, this chapter concludes with the Raman and XPS characterizations used for buffer layer samples. The characteristic Raman and XPS signatures serve as a guide for connecting the synchrotron results to other characterizations, such as transport measurements.

2.1 Surface X-ray Diffraction

X-ray crystallography was established over 100 years ago when Max von Laue discovered that crystals diffracted x-rays. Today the technique is ubiquitous for the determination of the atomic and molecular structure of a crystal, chemical bonds and disorder. The benefit of x-rays for crystallography is that the x-ray wavelength ($\sim$1 Å) is comparable to the separation distances between atoms. This allows for constructive and destructive interference of the scattered x-ray. Accurate modeling and measurement of the diffracted intensity provides quantitative and highly precise information, such as crystal and surface structure and lattice constants accurate to within thousands of an angstrom.

The advent of synchrotron facilities providing high intensity monochromatic x-rays

opened up the field of surface x-ray diffraction (SXRD). The high flux with excellent energy resolution means that fewer atoms are needed to provide measurable diffracted intensity. As the experimental technique improved, so too did the production methods of graphene growth on SiC. In this thesis, I present the convergence of these efforts with the first SXRD measurements of well ordered single layer graphene on SiC(0001) using synchrotron radiation. To appreciate the results of the SXRD measurements, I will provide an overview of SXRD in this section.

2.1.1 The Kinematic Approximation

The need for a high flux x-ray source stems from the fact that x-rays weakly scatter. Although this necessitates synchrotron light sources, the weakly interacting x-ray allows for a relatively straightforward analysis and prediction of the diffracted intensity through the kinematic approximation. The scattered amplitude of an x-ray from an electron bound to a nucleus is often described by the dipole approximation. The result is Thomson's formula [70],

$$Ae^{-i\mathbf{k}_f\cdot\mathbf{r}_e} = A_o\frac{e^2}{4\pi\varepsilon_o mc^2}\frac{1}{R_o}e^{-i\mathbf{k}_o\cdot\mathbf{r}_e}, \tag{2.1}$$

where A is the amplitude of the scattered x-ray electric field, A_o is the amplitude of the incident x-ray, R_o is the distance to the observation point, and $\mathbf{k}_o$ and $\mathbf{k}_f$ are the incident and scattered wavevectors. The weak interaction is seen by classical electron radius $e^2/(mc^2) \approx 3\times10^{-15}$ m, which is much smaller than atomic distances. A result of this is that $A \ll A_o$ and the single scattering or first Born approximation can be used. This enables the total scattering amplitude to be expressed as a superposition of individual scattering events from all atoms present in the system. Writing the scattered amplitude in this way is known as the kinematic approximation. Furthermore, the scattering in x-ray diffraction considers only the elastically scattering such that $|\mathbf{k}_f| = |\mathbf{k}_i| = k$.

By rewriting equation 2.1 with the substitution, $\mathbf{Q} = \mathbf{k}_f - \mathbf{k}_i$, the concept of momentum

transfer is introduced and A_f is now a function of $\mathbf{Q}$,

$$A(\mathbf{Q}) = A_o \frac{e^2}{4\pi R_o \varepsilon_o mc^2} e^{i\mathbf{Q}\cdot\mathbf{r}_e}. \tag{2.2}$$

Moving on from scattering of an individual electron to the electron density around an atom involves an integral over the electron density of the atom,

$$A(\mathbf{Q}) = A_o \frac{e^2}{4\pi R_o \varepsilon_o mc^2} \int \rho(\mathbf{r}) e^{i\mathbf{Q}\cdot\mathbf{r}} d\mathbf{r}. \tag{2.3}$$

This is merely the Fourier transform of the electron density, $f_\alpha(\mathbf{Q})$, and is known as the atomic form factor. In reality, the atomic form factor is also a function of photon energy, i.e. $f_\alpha(E, \mathbf{Q})$. The results of which have been tabulated for each atom [71, 72]. $f_\alpha(E, \mathbf{Q})$ is largely determined by Z, the atomic number of the atom. Care must be taken with ionic compounds as x-ray diffraction interacts with the electron cloud, not the nucleus. With the atomic form factor in hand, $A(\mathbf{Q})$ for multiple atoms can be calculated. The scattering amplitude in the kinematic limit is,

$$A(\mathbf{Q}) = A_o \frac{e^2}{4\pi R_o \varepsilon_o mc^2} \sum_{i=0}^{N-1} f_i(E, \mathbf{Q}) e^{i\mathbf{Q}\cdot\mathbf{r}_i}, \tag{2.4}$$

where $\mathbf{r}_i$ is the centered position of each atom in the system. By assuming R_o is far away compared to the illuminated area, R_o can be approximated as the same for each atom. In this form, the scattered amplitude can be calculated exactly if all the positions of the atoms are known. However, the realistic situation is the reverse, with a caveat. A typical x-ray diffraction measurement actually measures the scattered integrated intensity, $I_{int} = \int |A(\mathbf{Q})|^2 dt d\Omega$, in an attempt to determine the atomic positions. However, the phase information of $A(\mathbf{Q})$ is lost when measuring the intensity. Consequently, analysis of an x-ray diffraction measurement involves the construction of a model atomic system that possesses fitting parameters to reproduce the measured diffracted intensity.

The prototypical example is a bulk crystal. A bulk crystal can be idealized as a nearly infinite periodic structure. A crystal consists of a "unit cell" that is tiled throughout space. Mathematically, the positions of atoms in a crystal are described by basis and lattice vectors. The lattice vectors describe the periodicity of the system and how space is filled. The position of the lattice points can be written as,

$$\mathbf{R}_l = n_l\mathbf{a} + m_l\mathbf{b} + p_l\mathbf{c}, \tag{2.5}$$

where $\mathbf{a}$, $\mathbf{b}$, and $\mathbf{c}$ are the primitive lattice vectors and n_l, m_l, and p_l are integers describing the location of the lattice point l. The primitive lattice vectors are normally non-orthogonal. For *two* dimensional systems, such as graphene, there are only *two* lattice vectors, $\mathbf{a}$ and $\mathbf{b}$. Graphene lattice vectors are hexagonal, which means $\mathbf{a}$ is rotated 120° from $\mathbf{b}$. Each lattice point acts as an origin for the placement of basis atoms. If the unit cell possesses only one basis atom, then the position of the basis atom is most simply at the origin. For unit cells of two or more basis atoms, the basis positions are,

$$\mathbf{R}_b = u_b\mathbf{a} + w_b\mathbf{b} + v_b\mathbf{c}, \tag{2.6}$$

where u_b, w_b, and v_b are necessarily not integers, but some fractional position of the unit cell. It is not necessary to write the basis positions in terms of the lattice vectors, though it is often convenient.

Describing the atomic positions in this manner allows us to separate the scattering amplitude of the lattice and basis terms,

$$A(\mathbf{Q}) = A_o\frac{e^2}{4\pi R_o\varepsilon_o mc^2}\sum_b^{N_b} f(E,\mathbf{Q})e^{i\mathbf{Q}\cdot\mathbf{R}_b} \times \sum_l^{N_L} e^{i\mathbf{Q}\cdot\mathbf{R}_l}, \tag{2.7}$$

where N_b is the number of basis atoms, N_L is the total number of lattice points and the total number of atoms in the crystal is $N = N_bN_L$. The first factor is called the structure

factor, $F(E, \mathbf{Q})$. This is often the desired information for developing a structural model from a diffraction measurement. In its present form, $F(E, \mathbf{Q})$ is static, but real systems are dynamic and may also have disorder. A Debye-Waller factor is a common way to correct for these deviations from a perfect crystal [59, 63, 73]. A diffraction measurement at an instant in time can be thought of as a static measurement of the vibrating atoms oscillating about its central position. The time and space averaged structure factor can be obtained by a convolution of the atomic density with a Gaussian. The structure factor accounting for these considerations becomes,

$$F_{DW}(E, \mathbf{Q}) = \int \left(\int \rho(\mathbf{r} - \mathbf{u}))G(\mathbf{u}, \boldsymbol{\sigma})d\mathbf{u} \right) e^{i\mathbf{Q}\cdot\mathbf{r}} d\mathbf{r}, \tag{2.8}$$

where $G(\mathbf{u}, \boldsymbol{\sigma})$ is a normalized Gaussian of anisotropic widths $\boldsymbol{\sigma}$. Making use of the convolution theorem, the Fourier transform of a convolution is the product of the Fourier transforms of electron density and the Gaussian distribution. The Fourier transform of the electron density is the original structure factor, $F(E, \mathbf{Q})$ and the Fourier transform of a Gaussian is also a Gaussian. The structure factor becomes,

$$F_{DW}(E, \mathbf{Q}) = \sum_{b}^{N_b} f(E, \mathbf{Q}) e^{i\mathbf{Q}\cdot\mathbf{R}_b} e^{-1/2(\mathbf{Q}\cdot\boldsymbol{\sigma}_b)^2}, \tag{2.9}$$

where the result is generalized to allow for thermal and static variation for the different atoms in the unit cell. A consequence of the Debye-Waller factor is that it will decrease the scattered intensity at higher Q. As the temperature or disorder increases, less and less diffracted intensity will be measured.

The second term in equation 2.7 is the interference function. Expressing $\mathbf{R}_l$ in its primitive lattice vectors,

$$A(\mathbf{Q}) = A_o \frac{e^2}{4\pi R_o \varepsilon_o m c^2} F_{DW}(E, \mathbf{Q}) \sum_{n_l}^{N_l} e^{(i\mathbf{Q}\cdot\mathbf{a})n_l} \sum_{m_l}^{M_l} e^{(i\mathbf{Q}\cdot\mathbf{b})m_l} \sum_{p_l}^{P_l} e^{(i\mathbf{Q}\cdot\mathbf{c})p_l}, \tag{2.10}$$

it can be seen that the sum over each lattice vector is a geometric series, whose sum is,

$$S_n(x) = \frac{1 - e^{ixn}}{1 - e^{ix}}. \tag{2.11}$$

The resulting intensity can written as,

$$I(\mathbf{Q}) = \left(A_o \frac{e^2}{4\pi R_o \varepsilon_o mc^2} \right)^2 |F_{DW}(E, \mathbf{Q})|^2 |S_{N_l}(\mathbf{Q} \cdot \mathbf{a})|^2 |S_{M_l}(\mathbf{Q} \cdot \mathbf{b})|^2 |S_{P_l}(\mathbf{Q} \cdot \mathbf{c})|^2 \tag{2.12}$$

The square modulus of $S_n(x)$ is known as a "n-slit interference function," $|S_n(x)|^2 = \sin^2(nx/2)/\sin^2(x/2)$. Figure 2.1 demonstrates the behavior of $|S_n(x)|^2$ with increasing n. One of its properties is that it becomes sharply peaked as n increases. The inverse relationship between the width and n allows the order of surfaces and crystals to be determined, $Qa_{FWHM} = 2\pi 0.901/n$, where n is an estimate of the average domain size [73]. The peaks that develop are also periodic on 2π. It quickly becomes the case that as n increases, the only $\mathbf{Q}$ where significant diffracted intensity occurs is when the argument of the $S_n(x)$ is a integer multiple of 2π and $|S_n(2\pi)|^2 = n^2$. This gives rise to diffraction conditions,

$$\mathbf{Q} \cdot \mathbf{a} = 2\pi h;\ \mathbf{Q} \cdot \mathbf{b} = 2\pi k;\ \mathbf{Q} \cdot \mathbf{c} = 2\pi l, \tag{2.13}$$

where all three of these equations must be satisfied. The values of $\mathbf{Q}$ that satisfy these equations are the reciprocal lattice vectors, $\mathbf{G}_{hkl} = h\mathbf{a}^* + k\mathbf{b}^* + l\mathbf{c}^*$, where $\mathbf{a}^*$, $\mathbf{b}^*$, and $\mathbf{c}^*$ are the primitive reciprocal lattice vectors. This result shows that the same lattice concept in real space applies in reciprocal space. The primitive reciprocal lattice vectors can be determined from the real space lattice vectors,

$$\mathbf{a}^* = 2\pi \frac{\mathbf{b} \times \mathbf{c}}{\mathbf{a} \cdot \mathbf{b} \times \mathbf{c}};\ \mathbf{b}^* = 2\pi \frac{\mathbf{c} \times \mathbf{a}}{\mathbf{a} \cdot \mathbf{b} \times \mathbf{c}};\ \mathbf{c}^* = 2\pi \frac{\mathbf{a} \times \mathbf{c}}{\mathbf{a} \cdot \mathbf{b} \times \mathbf{c}}; \tag{2.14}$$

When the primitive reciprocal lattice vectors are properly defined, it is convenient to de-

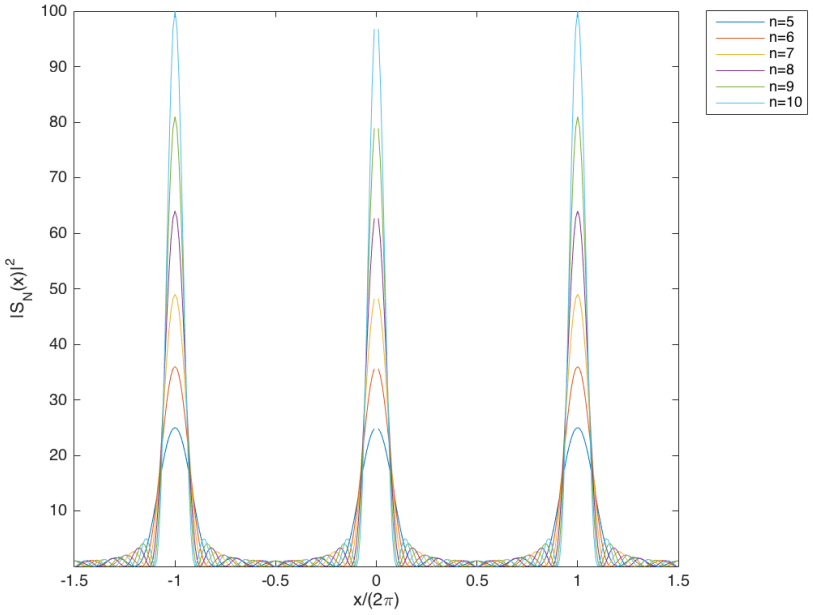

Figure 2.1: The bahvior of the n-slit interference function as a function of n. As n increases, the peak height increases, the width narrows, and $|S_n(x)|^2$ approaches a periodic distribution of delta functions.

scribe a location in reciprocal space in terms of (hkl), the reciprocal lattice units (r.l.u.).

2.1.2 Diffraction from Surfaces

For a surface, periodicity is broken in one direction. The lattice vectors are typically defined according to parallel and perpendicular components of the surface, even if they are not the bulk primitive lattice vectors. Convention states that $\mathbf{a}$ and $\mathbf{b}$ are the parallel components and $\mathbf{c}$ is the perpendicular component. Because of the broken periodicity at the surface the diffraction condition is relaxed for perpendicular momentum transfer ($\mathbf{Q}_z$ or l in r.l.u). Treatment of the diffraction intensity in $\mathbf{Q}_z$ requires care and can be understood in the context of attenuation. Diffraction intensity decays exponentially with depth into the bulk material. This can be accommodated with an attenuation parameter, $e^{-z\lambda} = \alpha$, where

$0 \leq \alpha < 1$. Accounting for α amounts to a correction to $S_n(x)$, for $\mathbf{Q}_z$.

$$S_{P_l}(\mathbf{Q} \cdot \mathbf{c}) = \frac{1 - (\alpha e^{i\mathbf{Q}\cdot\mathbf{c}})^{P_L}}{1 - \alpha e^{i\mathbf{Q}\cdot\mathbf{c}}}. \tag{2.15}$$

For x-rays, $\alpha \approx 1$ because x-rays weakly scatter and will have a large attenuation length. However, $\alpha^{P_l} \to 0$ since P_l is still large and λ is finite. Within these limits, the diffracted intensity for bulk reciprocal lattice vectors after accounting for the surface is,

$$I(\mathbf{Q}) = |F_{DW}(E, \mathbf{Q})|^2 \left| \frac{1}{1 - e^{i\mathbf{Q}\cdot\mathbf{c}}} \right|^2. \tag{2.16}$$

The diffracted intensity is still strong at integer values of l. However, information regarding surface reconstructions, defects, substrate steps is contained between the Bragg reflections.

Diffraction from a surface is not restricted to the bulk reciprocal lattice vectors. If a surface contains a purely two dimensional monolayer above its bulk structure or there exists a surface reconstruction there will be diffraction from the reciprocal lattice vectors of the surface. For example, graphene on SiC has a different lattice parameter from SiC. The periodicity of graphene will cause diffraction at a non bulk position in reciprocal space. Because graphene is only one layer and should theoretically be flat, diffraction at graphene reciprocal lattice positions are expected to be independent of $\mathbf{Q}_z$, $S_1(\mathbf{Q} \cdot \mathbf{c}) = 1$. This means the diffracted intensity should be the same regardless of the perpendicular momentum transfer component. What was once a diffraction *spot* for a three dimensional crystal is now a diffraction *rod* for a two dimensional crystal in reciprocal space. As a result, measurement of any changes in intensity with $\mathbf{Q}_z$ for a graphene reciprocal lattice rod provides information about the number of layers, vertical corrugations, surface roughness, and coupling to the SiC interface. To account for surfaces with distinct periodicities, the structure must be rewritten into to terms, $F_{Tot} = F_{Bulk} + F_{Surf}$. When calculating the diffracted intensity in this manner, care must be taken to account for the *cross terms*, such as $F_{Bulk}F^*_{Surf}$ and $F^*_{Bulk}F_{Surf}$.

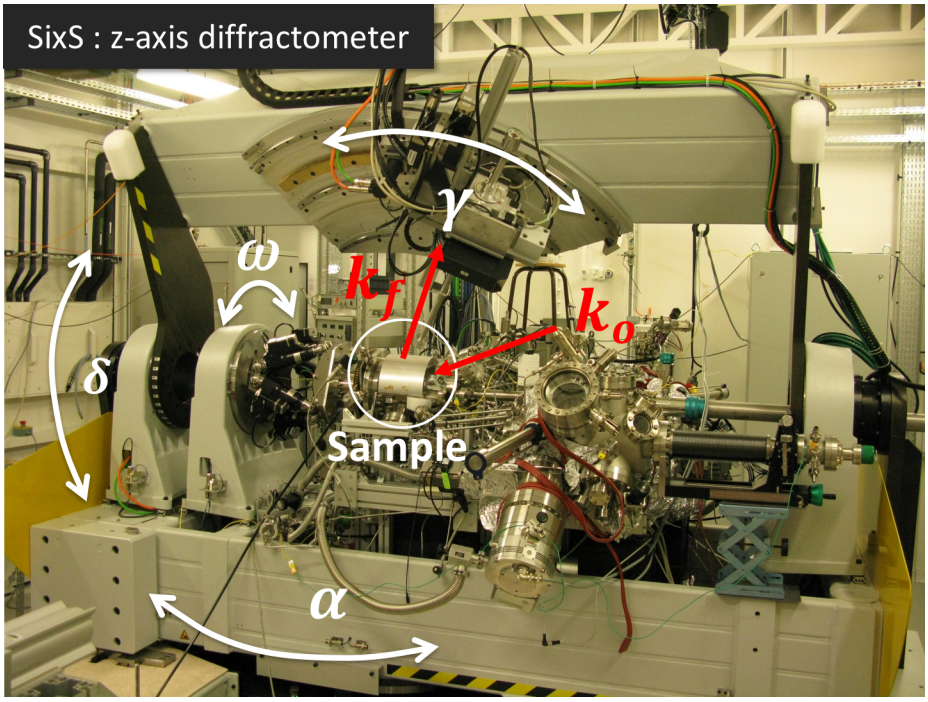

Figure 2.2: Image of the Z-axis diffractometer at the SixS beamline at SOLEIL Synchrotron. The greek letters represent the motors associated with the relevant angles they modify. $\mathbf{k}_o$ and $\mathbf{k}_f$ label the incident and reflected beam. The sample is measured in UHV conditions and Be window is used to minimize x-ray absorption. Image courtesy of Dr. Yves Garreau.

2.1.3 Integrated Intensity

In a typical diffraction measurement, the quantity being measured is the integrated intensity, I_{int}, rather than the intensity at a specific $\mathbf{Q}$ [75, 76]. The reason for this can be seen from the schematic in Figure 2.3. Because of the finite size of the detector and finite width of the diffraction rods, the detector is measuring the total diffracted intensity within a range of reciprocal space associated with a single diffraction rod. For such a measurement, a series of corrections can be made to obtain information regarding $|F_{DW}(E, \mathbf{Q})|^2$. To maximize the surface diffraction, the incident angle, α, is set near grazing incidence just above the critical angle. The integrated intensity is the total energy that strikes the detector area over

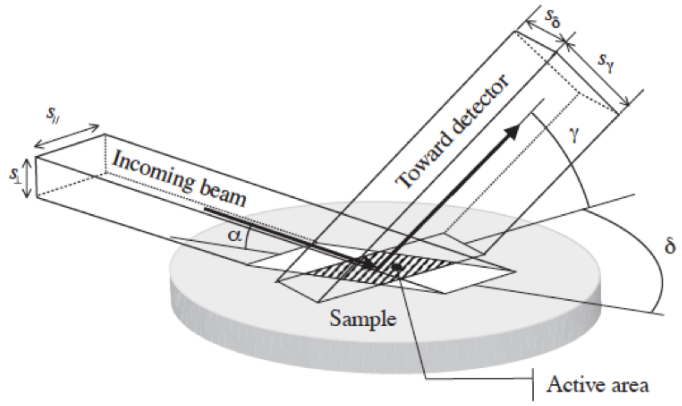

Figure 2.3: Schematic of and SXRD measurement using a Z-axis diffractometer. Image taken from ref. [74]. α is the incident angle, δ and γ describe the detector position, and ω rotates the sample. For a surface sensitive measurement, α is at grazing incidence. The finite size and projection of the incident beam on the surface and the finite size of the detector acceptance determine the active diffracting area. The finite size of the detector acceptance also determines rod interception corrections.

the entire duration of the measurement and can be written as [77],

$$I_{int} = \int |A(\mathbf{Q})|^2 dt d\gamma d\delta, \tag{2.17}$$

where γ and δ describe the position of the detector [see Figure 2.3]. The integral over time is often converted to an angular integration based off of the scan direction and velocity. The measurements in this thesis were collected in a step-by-step stationary geometry, i.e. the detector was set to fixed angular positions for a given amount of time and the total integrated intensity was collected before advancing to the next set of angular positions. In this configuration the integrated intensity is,

$$I_{int}(\mathbf{Q}) = T \int |A(\mathbf{Q})|^2 d\gamma d\delta, \tag{2.18}$$

where the limits of integration are set by the slit widths, s_δ and s_γ [see Figure 2.3]. To evaluate this integral the angular variables must be converted to reciprocal space coordinates. Additionally, there are a variety of other considerations that ultimately amount to

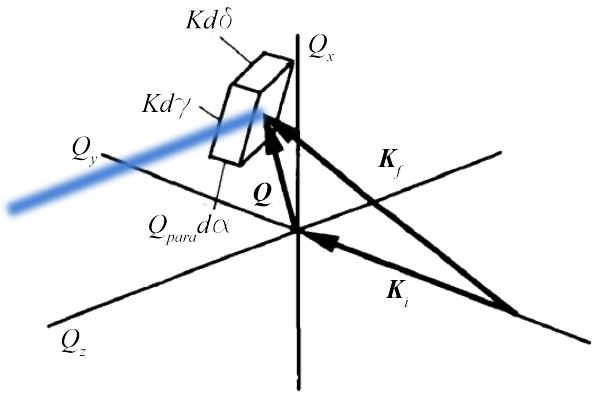

Figure 2.4: Schematic of SXRD in reciprocal space. The image is taken from ref. [75] and modified for the angular notation typically used for z-axis diffractometers. A surface diffraction rod has been added (in blue) to demonstrate the non-orthogonal volume element of integration. Also, the diffraction rod is blurred to demonstrate broadening that may occur from long range order, surface roughness and strain [73].

a set of correction factors that have been outlined previously for a variety of geometries and measurements [75, 78]. The result is that the integrated intensity can be related to an overall correction factor that varies with the angular positions of the incident and reflected beam,

$$I_{int} = C_{TOT}|F(\mathbf{Q})|^2, \tag{2.19}$$

where C_{TOT} is the total correction factor. $C_{TOT} = I_o L P C_A C_{rod} C_{det} C_{beam}$ can be broken into multiple factors related to: a scale (I_o), Lorentz (L), polarization (P), illuminated area (C_A), rod interception (C_{rod}), detector acceptance (C_{det}), and beam width (C_{beam}) factor.

Often, the physical constants are absorbed into a single fitting parameter relating to an overall scale factor I_o. The Lorentz factor results from the change of variables of integration and is obtained by evaluating the volume element, $dV = (kd\boldsymbol{\delta} \times kd\boldsymbol{\gamma}) \cdot Q_{para} d\boldsymbol{\alpha}$ [see Figure 2.4]. The relationship to reciprocal space coordinates is obtained by recognizing that $dV = (\mathbf{a}^* \times \mathbf{b}^*) \cdot \mathbf{c}^* dhdkdl = 8\pi^2/V_u dhdkdl$. The vectors for $\boldsymbol{\alpha}$, $\boldsymbol{\delta}$, $\boldsymbol{\gamma}$, $\mathbf{k}_i$, and $\mathbf{k}_f$ can be determined by a set of rotation vectors as demonstrated in ref. [79, 75]. After some algebra, the Lorentz factor can be determined and it is form depends on the type of measurement.

The two types of SXRD measurements I present in this thesis are reflectivity and in-plane diffraction. For in-plane measurements, $\mathbf{Q}_{para}$ is nonzero and for reflectivity $\mathbf{Q}_{para} = 0$. When measuring diffraction at $\mathbf{Q}_{para} = 0$, $(00l)$, this is often referred to as the specular rod. The specular geometry requires that $\alpha = \gamma$ and $\delta = 0$ whereas to measuring nonspecular diffraction rods requires δ to be nonzero. The Lorentz factor is different for these two scenarios: $L^{-1} = \sin\alpha$ for reflectivity, and $L^{-1} = \cos\alpha \sin\delta \cos\gamma$ for non-specular.[75].

Polarization from the synchrotron radiation was in the horizontal plane [see Figure 2.2] and the surface plane of the sample is vertical resulting in a polarization correction of $P = 1 - (\sin\alpha \cos\gamma \cos\delta + \cos\alpha \sin\gamma)^2$ [74]. Figure 2.3 shows that the illuminated area can be taken as the intersection of the projected beam area, sample area and projected area of the detector slits onto the surface. This correction is most easily obtained numerically when measuring in-plane diffraction rods. For reflectivity, the area correction is easily obtained analytically, $C_A = \min(L_S, s_\perp / \sin\alpha)$, where L_S is the sample length, $s_\perp$ is the incident beam perpendicular to the surface ($\approx 70\ \mu m$). The logic condition accounts for spill over when α is small and the projected area is larger than the sample. For a typical sample length of 4 mm, the cutoff angle is roughly 1° ($\mathbf{Q}_z = 0.07$ Å^{-1}).

Rod interception is a property unique to surface diffraction. If the system is sufficiently ordered, the diffraction is relatively sharp in h and k. However, in l the diffraction is more of a constant, than sharply peaked. As a result, the angular positions of the detector area intercepts the rod at a nonorthogonal angle. This is represented by the rod shown in Figure 2.4. C_{det} accounts for the case when the detector slits are not wide enough to capture the full integrated intensity of the diffraction rod and is best calculated numerically. C_{beam} accounts for nonuniformity of the incident intensity and can be calculated numerically as well [75].

Measurements were conducted on a Z-axis diffractometer [74] at SOLEIL Synchrotron on the SixS beamline. The SixS diffractometer is shown in Figure 2.2. The definitive

feature of the Z-axis diffractometer is through the control of the incident angle, α, by rotation of the entire diffractometer [74]. This type of system is ideally suited for surface studies because it is straightforward to maintain a fixed incident angle at grazing incidence just above the critical angle of total internal reflection. For SXRD, it is critical to maintain grazing incidence to maximize illumination of the surface and increase the surface to bulk intensity ratio.

My objective for diffraction measurements in this thesis is to obtain information regarding the structure of graphene and its interface with SiC. Since the lattice parameters of 4H-SiC is well known [80], reciprocal space can be defined in terms of SiC reciprocal lattice units $(hkl)_{\text{SiC}}$, i.e. $\mathbf{Q} = h\mathbf{a}^*_{\text{SiC}} + k\mathbf{b}^*_{\text{SiC}} + l\mathbf{c}^*_{\text{SiC}}$ where $a^*_{\text{SiC}} = b^*_{\text{SiC}} = 2\pi/(a_{\text{SiC}}\sqrt{3}/2) = 2.3556$ Å^{-1} and $c^*_{\text{SiC}} = 2\pi/c_{\text{SiC}} = 0.6233$ Å^{-1}.

2.2 Angle Resolved Photoemission Spectroscopy

Angle resolved photoemission spectroscopy (ARPES) utilizes the photoelectric effect, which was discovered by Hertz[81] and later explained by Einstein.[82] The photoelectric effect introduces the photon, which has an energy $E = h\nu$, where h is Planck's constant and ν is the frequency. In the photoelectric effect, a photon of sufficiently high energy will eject an electron from the material. The kinetic energy of the electron, E_{kin}, as observed by the spectrometer, is described by the simple equation,

$$E_{kin} = h\nu - \phi_{det} - |BE|, \tag{2.20}$$

where ϕ_{det} is the work function of the detector, and BE is the binding energy of the electron state prior to photoemission. Figure 2.5 demonstrates the energy level lineup and fundamental processes for photoemission. The specimen and spectrometer are in electrical contact with each other such that they share the same Fermi level, E_F. When an photoelectron initially escapes from the surface it has a kinetic energy $E'_{kin} = h\nu - \phi_s - |BE|$,

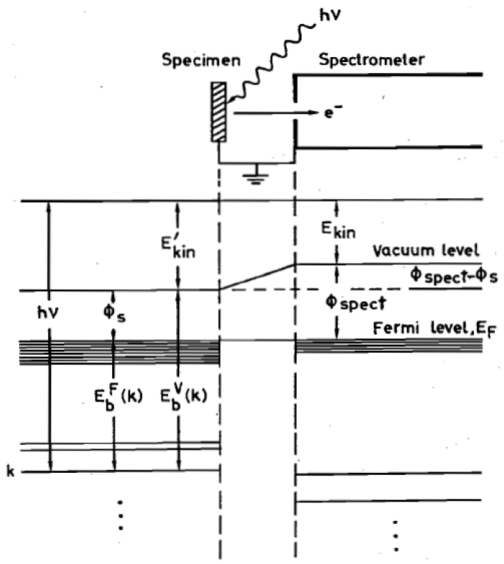

Figure 2.5: Schematic of the energy levels in photoemission spectroscopy from a metallic sample. Image from ref.[83]

where ϕ_s is the sample work function. Upon entering the spectrometer, an accelerating or decelerating potential is imparted on the electron based off the contact potential, $\phi_s - \phi_{det}$, such that the kinetic energy is increased or decreased. In this form, BE is measured with respect to E_F such that ϕ_{det} can be determined by fitting the photoemission cutoff E_{kin} to a Fermi function.

Angle Resolved Photoemission Spectroscopy (ARPES) measures the angular dependence of the photoelectrons as a function of binding energy in order to determine the momentum dependence and subsequently, $E(\mathbf{k})$ of the electronic band structure of the material. For graphene, ARPES allows the direct measurement of the Dirac cone-like dispersion of the π-bands. The kinetic energy of the photoemitted electrons is,

$$E_{kin} = \frac{K^2\hbar}{2m}. \tag{2.21}$$

K is the magnitude of the wavevector of the photoelectron and related to the momentum, $\mathbf{p} = \hbar\mathbf{K}$. m is the electron mass and $\hbar = h/(2\pi)$. Collecting the photoelectrons with a finite acceptance angle allows the discernment of the momentum dependence. Using the

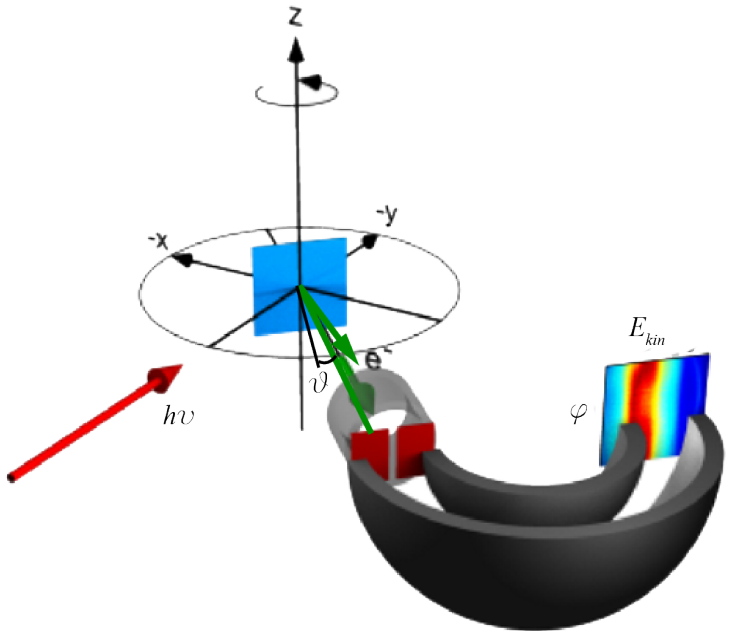

Figure 2.6: Schematic of ARPES geometry taken from http://nml.bu.edu/index_files/Page934.htm and modified for the notation used in this thesis. By measuring the photoemission spectra at defined polar (ϑ) and azimuthal (φ) angles, the parallel and perpendicular momentum of the photoemitted electrons can be determined.

notation in Figure 2.6, the momentum decomposition is,

$$K_x \approx 0.512\sqrt{E_{kin}}\sin\vartheta\cos\zeta\varphi, \tag{2.22}$$

$$K_y \approx 0.512\sqrt{E_{kin}}\sin\vartheta\sin\zeta\varphi, \tag{2.23}$$

$$K_z \approx 0.512\sqrt{E_{kin}}\cos\vartheta, \tag{2.24}$$

where 0.512 is the approximate value of $\sqrt{2m}/\hbar$ and $\zeta = 0.92$ is a correction for the entrance aperture optics for the Casiopee beamline at SOLEIL synchrotron. ARPES is ideally suited measuring the band structure of surface and two dimensional materials, like graphene, as the $\mathbf{K}_\parallel = \mathbf{K}_x + \mathbf{K}_y$ is related to the crysal momentum, $\mathbf{k}$, by a parallel reciprocal lattice vector, $\mathbf{K}_\parallel = \mathbf{k}_\parallel + \mathbf{G}_\parallel$, i.e. $\mathbf{K}_\parallel$ is conserved in the extended-zone scheme as opposed to the reduced-zone. The perpendicular momentum is not easily associated with a perpendicular crystal momentum $\mathbf{k}_\perp$ because at a surface the vertical periodicity

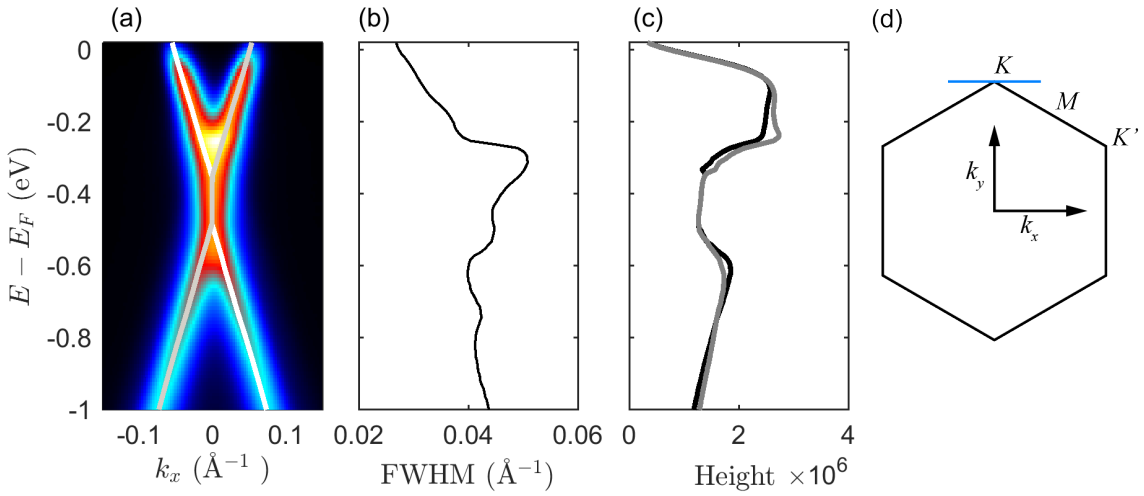

Figure 2.7: ARPES of monolayer graphene on SiC(0001). (a) ARPES spectra perpendicular to and at the$K$-point. The white lines show the fitted position of the π-bands. Graphene on this face is n-doped between 0.4 to 0.5 eV. (b) FWHM of the MDC linewidth of the graphene π-bands as a function of energy. (c) Height of the graphene π-bands as a function of energy. (d) Schematic of the region of reciprocal space probed by the ARPES measurement in (a)

is broken and therefore there is no perpendicular reciprocal lattice vector. Also there is an inner potential that causes the $\mathbf{k}_\perp$ to not be conserved. The photoemitted electrons are collected and analyzed by a hemispherical analyzer that has an energy and angle dispersing property [see Figure 2.6]. The entrance of the photoelectrons into the analyzer is limited by an entrance slit to limit the acceptance in ϑ. For a given ϑ the photoelectron intensity is measured as a function of E_{kin} and φ, $I(E_{kin}, \varphi)$. Since graphene is a 2D material, $\mathbf{k}_\perp$ is not associated with its band structure and these complications are less important in this context.

The ARPES measurement of graphene grown of SiC(0001) is shown in Figure 2.7. The color map represents a low photoelectron intensity (black) to a high intensity (yellow). The region of high intensity indicates the location of the graphene π-bands. The spectrometer was placed to collect photoelectrons with a momentum at the K-point. The location in reciprocal space of the measurement is shown in Figure 2.7(d). The "cut" is through the K-point and perpendicular to the ΓK direction. This is a convenient cut because it allows for

an easy measurement of the Dirac cone as both the left and right side of the Dirac cone are visible. This would not be the case for a cut taken along ΓK. There is a well known matrix element effect for graphene where half of the photoemission intensity expected for the Dirac cone is missing due to photoelectron diffraction and the incident photon polarization [62, 84, 34, 85, 86]. This matrix element effect is shown in Figure 2.8. The measurement is a constant-energy cut of the graphene ARPES spectra. Constant energy surfaces are obtained by measuring the ARPES spectra for a set of ϑ's. By changing ϑ, a different set of $\mathbf{K}$ are probed. After collecting these measurements, the results can be stitched together to visualize a cut with a fixed $E - E_F$. For the results shown, the constant energy cut was taken at 1 eV below the Dirac point. This is the reason for the circular shape of the photoelectron intensity. If the constant energy cut was taken at the Dirac point energy, E_D, the constant energy surface shown would consist of six points. Since half the Dirac cone is missing in Figure 2.8, it can be seen that a cut along ΓK will only show half of the Dirac cone and this will make it difficult to identify the Dirac point. Another feature in Figure 2.8 is the appearance of satellite Dirac cones around the $K_{\pm}$-points. This is the result of Umklapp processes where multiple scattering occurs from the underlying periodicities in the interface layers [84, 62].

When analyzing the properties of the Dirac cone, the results are similar to what is expected for theoretically freestanding graphene. By fitting the π-bands to a Lorentzian distribution for each Momentum Distribution Curve (MDC), which is the photoelectron intensity for a constant energy for a given cut, the central positions and widths of the π-bands were obtained [see Figure 2.7(b)]. The central positions can be fitted to a line to obtain a Fermi velocity. It was found that $v_F = c/275$ where c is the speed of light. The linearity and similarity to the predicted $v_F = c/300$ provide excellent evidence for a Dirac cone in graphene grown on SiC.

There are also a few differences from theoretically freestanding graphene. The charge neutrality point for graphene is normally at the Dirac point, i.e. where the valence and

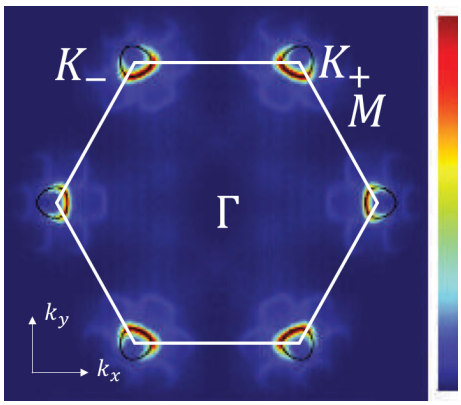

Figure 2.8: Constant energy cut at $E - E_F = E_D - 1$ eV of graphene on SiC. Figure taken from ref. [84]. Labels were added based off of the nomenclature used here. The constant energy cut demonstrates the matrix element effect that cancels out part of the photoemission intensity of the Dirac cone. It also shows the Umklapp processes associated with multiple scattering from the interface reconstruction.

conduction band touch. However, for ML, there is a significant doping of 0.4 eV, similar to previous measurements [47, 84, 34]. This doping is often attributed to charge transfer from the substrate and spontaneous polarization [87, 88]. One of the more notable differences from freestanding graphene is that the bonding and antibonding π-bands do not touch. There is a separation of roughly 130 meV. Furthermore, there is a decrease in intensity in the region between the two π-bands [see Figure 2.7(c)]. These observations were initially thought to be the result of the formation of a band gap [34]. Later it was shown to be the result of plasmons from the photoemission process [84]. This explanation was achieved by observing that the separation between upper and lower π-bands increased with doping and by measuring the MDC linewidths of the π-bands. The MDC linewidths for a CSS sample is shown in Figure 2.7(b). In an ARPES measurement, the MDC linewidth is related to the electron-phonon coupling, electron-hole pair generation, electron-plasmon coupling, and impurity scattering [84, 89]. The shape of the MDC linewidths were in excellent agreement with these various many body excitations and provided strong evidence that this effect was not due to a substrate-induced band gap.

However, my measurements have much higher counting statistics than the previous report because of my interest in the underlying buffer layer. The results show that there

are two peaks in photoemission intensity at ~ -0.3 and ~ -0.1 eV below E_F that were not observed previously. Later, I show that this is related to the buffer layer underneath the monolayer. One of the assumptions made by Bostwick *et al.* was that the electronic bands of the buffer layer and SiC were well below E_F and therefore could not couple near the Dirac point. Such an argument may no longer be valid and the possibility of a substrate induced gap must be reconsidered.

Nevertheless, ARPES has proved to be a powerful technique for understanding the quality of the graphene. For instance, while this gap is observed on SiC(0001), it is not observed on graphene grown on SiC($000\bar{1}$) [90]. The ability of ARPES to observe effects like doping, band gaps, substrate interactions, many body effects and chirality [85] make ARPES a powerful and essential tool for developing a deeper understanding of the properties of graphene and its response to its environment.

For graphene on SiC(0001), the buffer layer has not been as well studied as monolayer graphene. However, the buffer layer serves as an ideal platform for studying the effects of substrate interaction and was recently shown to have a band gap greater than 0.5 eV [62]. In this thesis, I develop a tight binding model of the buffer interaction with SiC based on the results from SXRD measurements to calculate the electronic band structure. These band structure calculations are then converted to a spectral weight expected for an ARPES measurement. The results of the calculated and experimental ARPES are compared and found to be in excellent agreement. The implications of this are twofold: (i) it provides merit to the structural model obtained from SXRD, (ii) the structural model provides an explanation for the observed band gap in the buffer layer.

2.3 X-ray Standing Wave X-ray Photoemission Spectroscopy

Typical x-ray photoemission techniques are surface sensitive up to 10's of nanometers. By generating an x-ray standing wave, the element specific vertical resolution of photoemission studies can be enhanced to within tenths of angstroms [91, 92, 93]. An x-ray standing

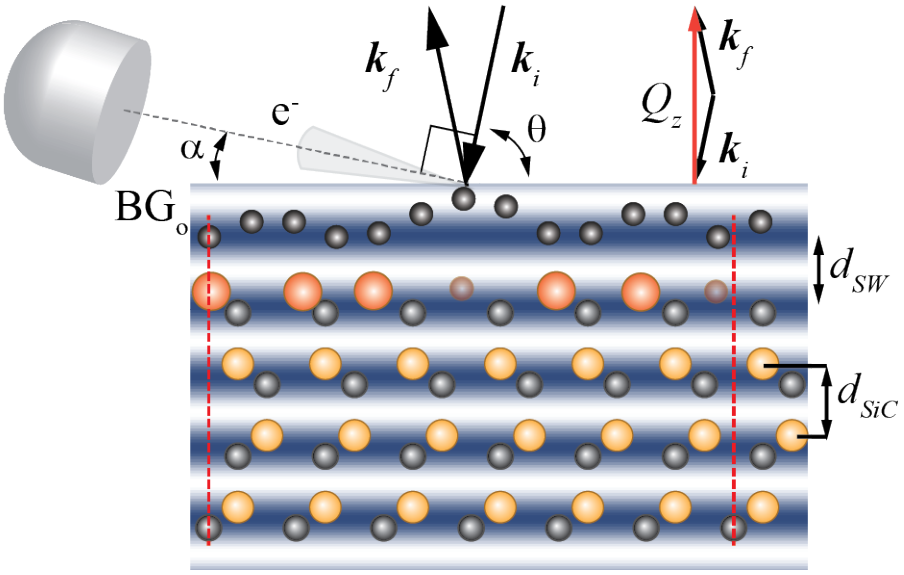

Figure 2.9: Schematic of x-ray standing wave photoemission. Superposition of the incident, $\mathbf{k}_i$, and reflected beam, $\mathbf{k}_f$, produce a standing wave indicated by the color map. From the momentum transfer, $\mathbf{Q}$, the standing wave period, d_{SW}, can be determined. The phase of the standing wave can be adjusted by tuning the angle and wavelength of the x-ray. The electron analyzer is placed to maximize the surface to bulk photoemission ratio. Since the photoemitted yield is proportional to the incident photon flux, a unique element specific yield is generated as d_{SW} passes through the d_{SiC}. The yield allows the determination of the average vertical distance (*modulo* d_{SiC}) and distribution of the chemical species.

wave can be generated by tuning the wavelength and incident angle to be near a Bragg reflection of the bulk material. At a Bragg reflection, the reflected wave is of sufficient intensity that the superposition of the incident and reflected beam generate a standing wave in the material. The fundamental principle of x-ray standing wave photoemission is that the photoemission yield is proportional to the interference field. Based on the atomic position, a unique photoemission yield is generated. Analysis of the photoemission yield allows sub-angstrom elemental resolution of the surface.

A schematic of the experimental setup for X-ray Standing Wave photoemission (XSW) is shown in Figure 2.9. The incident and reflected complex electric field can be modeled as

a plane wave for typical synchrotron studies,

$$\mathscr{E}_i = E_i e^{i(\omega t - \mathbf{k}_i \cdot \mathbf{r})}, \tag{2.25}$$

$$\mathscr{E}_f = E_f e^{i(\omega t - \mathbf{k}_f \cdot \mathbf{r})}, \tag{2.26}$$

where $\mathbf{k}_i$ is the incident wave vector and ω is the frequency of radiation. The scattered field, $\mathscr{E}_f$ will be a plane wave of similar form with a wave vector $\mathbf{k}_f$. For elastic scattering, the scattered frequency and wave vector magnitude are equal and for coherent scattering, the scattered and incident amplitude are related by,

$$\mathscr{E}_f = \sqrt{R}\mathscr{E}_i e^{i\nu} \tag{2.27}$$

where the phase, ν, is independent of t and $\mathbf{r}$. R is the reflectivity, $R = I_f/I_i = |\mathscr{E}_f|^2/|\mathscr{E}_i|^2$. The total electric field is the superposition the incident and scattered field, $\mathscr{E} = \mathscr{E}_i + \mathscr{E}_f$. A standing wave is generated by the interference pattern. By writing the scattered wave vector as, $\mathbf{k}_f = \mathbf{k}_i + \mathbf{Q}$, the normalized standing wave intensity can be written as,

$$I_N = \frac{|\mathscr{E}|^2}{|\mathscr{E}_i|} = 1 + R + 2\sqrt{R}\cos(\nu - \mathbf{Q} \cdot \mathbf{r}). \tag{2.28}$$

The color map in Figure 2.9 represents the standing wave normalized intensity. I_N is composed of planes of constant intensity that oscillate from its minimum and maximum when $\mathbf{r}$ is parallel to $\mathbf{Q}$. R and ν are calculated for the bulk material at the given $\mathbf{Q}$ from dynamical diffraction theory [94, 91],

$$\frac{E_f}{E_i} = \sqrt{R}e^{i\nu} = \sqrt{\frac{F_{\mathbf{Q}}}{F_{\bar{\mathbf{Q}}}}}\left(\eta \pm \sqrt{\eta^2 - 1}\right), \tag{2.29}$$

where $F_{\mathbf{Q}}$ and $F_{\bar{\mathbf{Q}}}$ are the structure factor calculated at the $\mathbf{Q}$ and $-\mathbf{Q}$, respectively. For these studies, the structure factor is calculated from 4H-SiC. The atomic positions for 4H-

SiC needed for calculating $F_{\mathbf{Q}}$ can be found in ref. [80]. This equation provides the primary relationships between the crystal structure and the reflectivity in the nonlinear scattering regime near a Bragg reflection.

The structure factor in dynamical diffraction theory requires corrections to the atomic form factor,

$$F_{\mathbf{Q}} = \sum_{n}^{N} \left(f_n^o(\mathbf{Q}) + \Delta f_n'(\lambda) + i\Delta f_n''(\lambda)\right) S_n(\mathbf{Q}) D_n(\mathbf{Q}), \tag{2.30}$$

where N is the number of atoms in the unit cell, $S_n(\mathbf{Q}) = e^{i\mathbf{Q}\cdot\mathbf{r_n}}$ is the phase factor determined from the $\mathbf{r}_n$ atomic positions within the unit cell and $D_n(\mathbf{Q})$ is a Debye-Waller factor for the n^{th} atom. $f_n^o(\mathbf{Q})$ is the atomic form factor, where a standard exponential expansion is used as an approximation [71]. $\Delta f_n'(\lambda)$ and $\Delta f_n''(\lambda)$ are the real and imaginary components of the anomalous scattering factors [72].

In an XSW measurement, either the incident angle or photon energy, $E = h\nu$, is varied to pass through the selected Bragg reflection. This is accomplished by setting $\mathbf{Q} = \mathbf{G} = h\mathbf{a}^* + k\mathbf{b}^* + l\mathbf{c}^*$, where $\mathbf{G}$ is the (khl) reciprocal lattice vector of the bulk. h and k describe the parallel components and l describes the components perpendicular to the surface. For the studies presented, the $(004)_{\text{SiC}}$ reciprocal lattice vector was chosen. This corresponds to the perpendicular components of the SiC(0001) surface.

For the presented experiments, E was varied instead of θ. As such, the anomalous scattering factors have to be adjusted for each E. η in equation 2.30 is given by [95],

$$\eta = \frac{-2(\Delta E/E_B)\sin^2\theta_B + \Gamma F_0}{|P|\Gamma\sqrt{F_{\mathbf{Q}}F_{\bar{\mathbf{Q}}}}}, \tag{2.31}$$

where $\Delta E = E - E_B$ with E_B being the photon energy associated with the Bragg reflection. θ_B is the Bragg angle. P is the polarization of the incident x-ray. For these studies, π-polarization was used, i.e. the polarization is in the scattering scattering plane, which amounts to $P = \cos 2\theta_B$. $\Gamma = (r_e\lambda^2)/(\pi V_c)$ is a scale factor with r_e being the classical

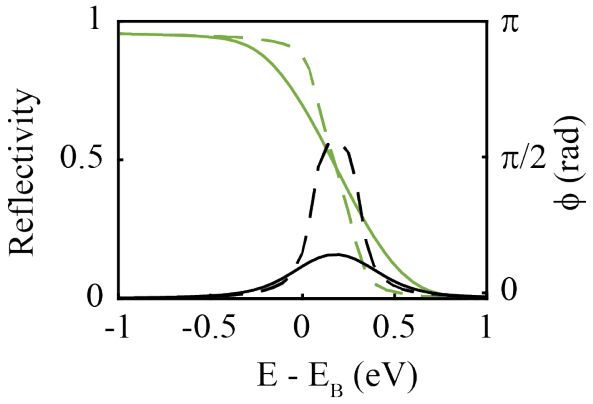

Figure 2.10: Calculated reflectivity (black) and phase (green) for the SiC(0004) reflection. The dashed lines are calculated assuming no energy broadening. Solid lines are the energy broadened reflectivity, $\Delta E \approx 170$ meV.

electron radius, V_c is the volume of the unit cell and λ is the wavelength of the incident x-ray.

The schematic in Figure 2.9 represents the measurement setup at the GALAXIES beamline at SOLEIL Synchrotron of the buffer layer sample. To achieve a significant diffracted intensity and hence a strong standing wave, the standing wave period, d_{SW}, was set to the SiC bilayer spacing $c_{\text{SiC}}/4 = 2.52$ Å. As a reminder, the Bragg diffraction condition is,

$$2d \sin\theta = n\lambda. \tag{2.32}$$

Therefore, the photon energy $E = 2512$ eV and $\theta_B = 78^\circ$ was used to achieve the SiC(0004) Bragg reflection. To account for the energy resolution of the incident x-ray beam, equation 2.29 was convoluted by normalized Gaussian whose width was the instrument resolution. The instrument resolution for the GALAXIES beamline was approximately 300meV. When fitting the photoemission yield, the instrument resolution as adjusted as a fitting parameter. From the fitting routine, the instrument resolution was determined to be 170 meV. Figure 2.10 demonstrates the broadened and unbroadened calculated reflectivity and phase for the SiC(0004) reflection, i.e. $\mathbf{G} = 4\mathbf{c}^*$, the magnitude of which is $Q_z = 2\pi/(4c_{\text{SiC}})$. It can be seen that the instrument resolution has a strong impact on the

total reflectivity and to a less extent on the phase.

The fundamental principle that enables the XSW technique is that photoemission is a function of the intensity of the photon source interacting with the bound electron. Since a standing wave was generated, the x-ray intensity is modulated at the atomic scale. From the dipole approximation, it can be shown that the photoemission yield from an atom at position $\mathbf{r}_j$ within the standing wave field is [91, 96],

$$Y_j^{\mathbf{G}} = 1 + R + 2P\sqrt{R}\cos\left(\nu + \mathbf{G}\cdot\mathbf{r}_j\right). \tag{2.33}$$

The normalized scattered yield is simply the superposition of the scattered yield for all atoms of a particular chemical species, i.e. of the same binding energy,

$$Y_j^{\mathbf{G}} = 1 + R + 2P\sqrt{R}N^{-1}\sum_n^N \cos\left(\nu + \mathbf{G}\cdot\mathbf{r}_n\right), \tag{2.34}$$

where N is the number of atoms at positions $\mathbf{r}_n$ belonging to the chemical species. Due to thermal vibrations, static disorder and corrugations, a distribution of $\mathbf{r}_n$ are possible for a given chemical species. As such this summation is often treated as an integral with a density of a particular form. The integral representation is,

$$Y_j^{\mathbf{G}} = 1 + R + 2P\sqrt{R}\int_{vol}\rho_j(\mathbf{r})cos(\nu - \mathbf{G}\cdot\mathbf{r})dr. \tag{2.35}$$

If a Gaussian distribution is assumed for $\rho(\mathbf{r})$, the normalized yield is,

$$Y_j^{\mathbf{G}} = 1 + R + 2P\sqrt{R}f_j^{\mathbf{G}}\cos\left(\nu + 2\pi P_j^{\mathbf{G}}\right), \tag{2.36}$$

where $f_j^{\mathbf{G}} = e^{-2\pi\sigma_j^2/d_{SW}^2}$ is coherent fraction and $P_j^{\mathbf{G}} = z_j/d_{SW}$ is the coherent position, and P is the polarization correction: 1 for σ-polarization and $\cos 2\theta_B$ for π-polarization. If the dipole approximation is no longer valid the expression becomes more complicated

[96]. However, for these studies, the C 1s and Si 2s core levels were used, which are well described by the dipole approximation. Also,I will show that the values for $f_j^{\mathbf{G}}$ and $P_j^{\mathbf{G}}$ are highly dependent on the spectral decomposition and this will limit the level of detailed analysis possible by XSW alone. As a result, non-dipolar corrections are smaller than the uncertainty from the spectral decomposition.

Parameterization of $f_j^{\mathbf{G}}$ and $P_j^{\mathbf{G}}$ can be understood considering equation 2.34. Each chemical species contributes a $\cos(\nu + \mathbf{G} \cdot \mathbf{r}_n)$ to the yield. The yield is then the result of a superposition of cosines of the same period that differ only in its phase. The result will also be a cosine whose amplitude will be determined by the positional distribution of the chemical species. If the position is well defined and only perturbed by small thermal vibrations, $f_j^{\mathbf{G}}$ will be close to unity. Examining $P_j^{\mathbf{G}}$, it can be seen that the derived position, z_j, has a $modulo - d_{SW}$ ambiguity. There are two methods to address this, (i) energy dependent photoemission and (ii) x-ray reflectivity. X-ray reflectivity is the best way to resolve this issue.

The advantage of the XSW technique is its connection to the structure factor from x-ray diffraction and its ability to address the phase problem. $f_j^{\mathbf{G}}$ and $P_j^{\mathbf{G}}$ are related to the chemical specific contribution to the structure factor, $F_j^{\mathbf{G}}$, for the given $\mathbf{G}$ as,

$$F_j^{\mathbf{G}} = f_j^{\mathbf{G}} e^{i2\pi P_j^{\mathbf{G}}}. \tag{2.37}$$

When assuming a Gaussian distribution, $f_j^{\mathbf{G}}$ becomes the Debeye-Waller factor,

$$f_j^{\mathbf{G}} = e^{-1/2(G\sigma_j)^2}, \tag{2.38}$$

where σ_j describes the total positional distribution as a Gaussian encompassing the effective variation from disorder, corrugation and thermal vibrations.

The process for analysis of an XSW measurement thus consists are measuring the photoemission spectra as a function of photon energy where the incident angle and wavelength

are tuned to be near a Bragg reflection of the bulk material. The energy range is small such that there is a minimal change in the period of the standing wave. However, the slight changes in photon energy alters the phase of the standing wave such that different atomic planes are excited. If multiple peaks are present, each spectra must be decomposed to obtain $Y_j^{\mathbf{G}}$, which is the integrated area of each spectral component as a function of photon energy. To obtain z_j and σ_j, equation 2.36 is fit to the experimental data. This requires the calculation of the energy resolution broadened reflectivity and phase using dynamical diffraction theory. z_j and σ_j then serves as inputs to x-ray reflectivity.

2.4 Growth and Characterization of Buffer Graphene

There has been substantial work focusing on the growth and characterization of graphene on SiC(0001) [97, 41, 37, 36, 98, 99, 100, 101]. However, most of this work focused on monolayer growth, rather than the buffer layer. To this end, detailed studies of the buffer layer were conducted with synchrotron radiation techniques, such as ARPES, SXRD and XSW. While these techniques can provide detailed information, the quality and consistency of the prepared samples has a direct impact of the information that can be obtained. For this reason, buffer samples were characterized by Raman spectroscopy and XPS prior to the synchrotron studies.

The current graphene growth method using confinement controlled sublimation consists of three heating stages. First, the sample is heated to ~300°C to remove any adsorbed water or organic contaminants. The second stage heating temperature is at 1200°C to remove additional contaminants and the last temperature step is for graphene growth. For each sample, the graphene growth time was 30 minutes and the initial heating stages were at least 15 minutes. The ramp time between the different temperature stages is limited by the thermal mass of the crucible and usually on the order of 1-2 minutes.

Raman measurements were conducted with a Horiba Jobin-Yvon LabRam and a $\lambda = 532$ nm laser. The spot size was $\sim 1\mu$m. The data was collected with a resolution of 1 cm^{-1}

over 1200 cm-1 to 3400 cm^{-1} at multiple locations for a given sample. The Raman shown reflects the best representation of the Raman collected for the specified growth conditions.

Figure 2.11 shows the Raman results for various graphene growth temperatures ranging from 1377°C to 1584°C . A bulk SiC carbide background was subtracted from each spectra [100, 99, 102]. The Raman spectra represents a characteristic spectra for the entire sample. Because the samples are grown by confinement controlled sublimation, a consistent Raman spectra is observed across the sample. Slight variations are possible across the sample due to temperature gradients from non-uniform heating. Variations in the Raman spectra for samples grown at temperature close to the buffer temperatures results are slight monolayer overgrowth coverage with a non-uniformity less than 5%. The variations that arise near monolayer growth temperatures are differences in graphene related peak positions, widths and heights indicating variations in the monolayer coverage and bilayer overgrowth.

These temperature studies found that no substantial Raman signature was observed below 1377°C . Above this temperature a characteristic buffer spectra is observed, similar to ref. [100]. The buffer spectra has a broad D (1350 cm^{-1}) and G peak (1582 cm^{-1}).[103] The D peak is associated with "defects" and the G peak with a sp^2 stretching mode [104]. A characteristic absence of a 2D peak accompanies the broad D and G features. There are two additional features at 1490 cm^{-1} (B_o) and 2950 cm^{-1}. These two features have yet to be adequately described. The broad feature at higher wavenumber is within a similarly broad range for a D+G peak indicating this feature may be a second order mode. While the peak B_o is at present unidentified, it initially increases and then appears suppressed once monolayer begins to form. This indicates it is a characteristic feature associated with the BG_o.

Another interesting feature is the relative insensitivity to the formation of monolayer graphene at lower temperatures. A measurable 2D signal only occurs at temperatures above 1430°C . This demonstrates that there is a reasonably large temperature range for producing buffer only surfaces or at minimum a surface with immeasurably low graphene

overgrowth. One consequence of this is the ability to produce nearly homogeneous buffer graphene. This is demonstrated by the lack of a 2D peak in the Raman spectra as well as XPS measurements shown below that estimate a fully covered graphene.

From the Raman spectra alone, it may not be clear that the buffer layer is structurally graphene due to a lack of a 2D peak or that the buffer layer fully covers the surface. Evidence that the buffer layer is structurally graphene comes from diffraction and STM measurements of a graphitic lattice constant[105, 60], and σ-bands in ARPES measurements [36]. Furthermore, the buffer layer can be hydrogen intercalated [61, 57, 60, 106]. Hydrogen intercalation consists of exposing the epitaxial graphene surface to H_2 near atmospheric pressure and at elevated temperatures greater than 500°C . The hydrogen is thought to saturate the bonds between the buffer and SiC interface. After intercalation, the buffer exhibits all the signs of free standing graphene, such as a Raman 2D peak and small D peak and most importantly a Dirac-cone in ARPES. Furthermore, prior to H_2, the buffer layer also has a graphite lattice constant [105].

XPS measurements were obtained with a Thermo Scientific K-alpha XPS Spectrometer using monochromatic Al K α x-ray radiation. C 1s, Si 2p and O 1s spectra were collected at multiple locations on the surface with a pass energy of 50 eV with a photoemission angle perpendicular to the surface. Each component of the C 1s spectra was fitted with a Pseudo-Voigt distribution. Figure 2.12 shows a typical C 1s spectra of the buffer layer. There are four components, a bulk SiC (C_B), two buffer components (S_1 and S_2), and one absorbed contaminant peak (C-x). The identification of C-x is based on comparisons with buffer samples that were heated in UHV prior to XPS characterization. For the synchrotron XPS measurements of the buffer, the samples were heated to 500°C prior to measurement in UHV. These measurements, shown in Chapter 5, do not observe the C-x component. However, for the Thermo XPS measurements it was not possible to anneal the sample prior to the measurement and a C-x component is observed. Monolayer samples do not possess a measurable C-x component. This indicates that the buffer layer is more reactive. Also, the

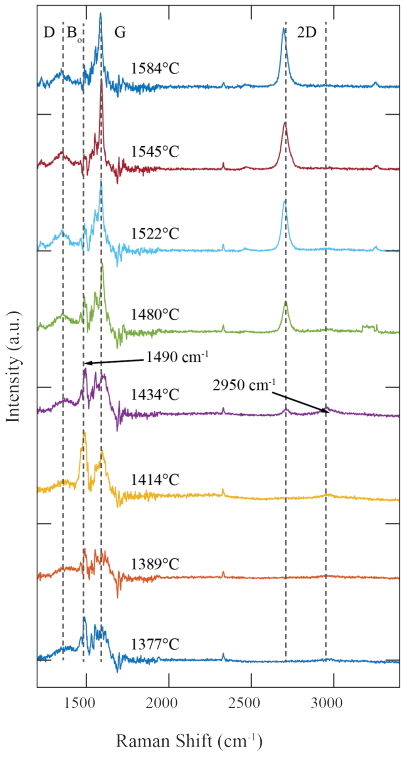

Figure 2.11: Raman spectra of the graphene growth on SiC(0001) for various growth temperatures. Each sample was heated for 30 minutes at a maximum temperature from 1377°C to 1584°C . Below 1377°C no significant Raman features were measured. The bulk SiC Raman was subtracted from each spectra. Vertical dashed lines label characteristic features from buffer and monolayer. D, B_o, G and 2D peaks are characteristic components of monolayer graphene. The buffer layer has broad D and G features with no 2D component. There are two additional features at 1490 cm^{-1} (B_o) and 2950 cm^{-1} that reach a maximum at a growth temperature of 1414°C . Much of the buffer features are reduced in monolayer samples.

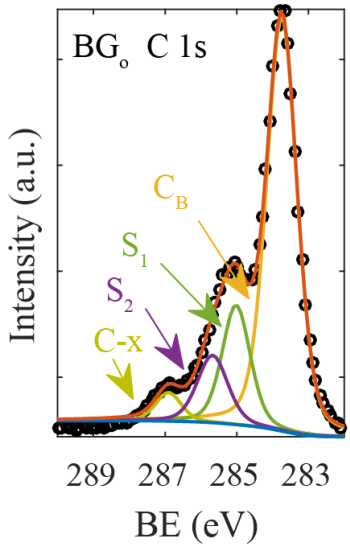

Figure 2.12: C 1s spectra of BG_o from standard K-alpha radiation. There are 4 components in the spectra, C_B is from the bulk, $S_1$and $S_2$are from BG_o and C-x is from absorbed carbon contaminants, this is known since annealing to moderate temperatures of 300°C eliminates this peak from the spectra.

strong monolayer peak obscures the photoemission signal from the buffer layer. For this reason, monolayer surfaces are fitted with three components, C_o, ML and S_1, where S_1 is for all buffer related features. It is typical to use an asymmetrical lineshape for the ML component. However, for the present analysis the integrated area of all graphene components is the relevant parameter, not a proper decomposition. For this reason peak parameters are not emphasized. A detailed analysis of the C 1s spectra using synchrotron radiation and X-ray Standing Wave techniques addresses these issues later in Chapter 5.

For now, a model for a semi-infinite bulk with an overlayer is used to estimate graphene coverage [83], where SiC is the bulk and graphene is the overlayer. The formula for estimating the number of graphene layers (N_g) is,

$$N_g = \lambda_g / c_g \ln\left(1 + \frac{I_g/s_g}{I_{\text{SiC}}/s_{\text{SiC}}}\right), \tag{2.39}$$

where $\lambda_g = 31$ Å ($\lambda_{\text{SiC}} = 25.8$ Å) is the graphene (SiC) attenuation length,[107] s_g

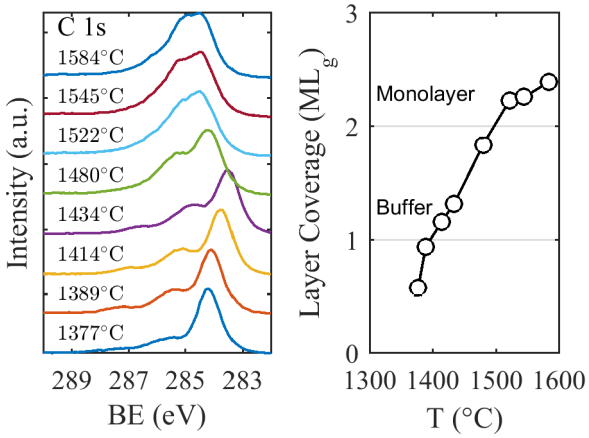

Figure 2.13: XPS analysis of Graphene grown on SiC(0001) with confinement controlled sublimation at increasing growth temperatures. (a) C 1s spectra of graphene samples grown with increasing growth temperature. At 1377°C , the buffer layer is undergrown and at 1584°C a substantial content of bilayer graphene has formed. (b) graphene layer coverage based on analysis using equation 2.39. Below 1377°C no substantial buffer layer has formed. Uniform coverage quickly develops at temperatures of 1400°C . Producing monolayer graphene requires a higher temperature and does not occur as rapidly with increasing temperature.

(s_{SiC}) is the sensitivity factor for graphene (SiC). The element specific sensitivity factor is $s_j = \sigma_j \rho_j \lambda_j$, where σ_j is the photoelectron cross section and ρ_j is the density. Since the cross sections are both from carbon, this parameter cancels in equation 2.39. The density of graphene is estimated by the areal density and the average layer spacing,c_g = 3.35 Å, ($\rho_g = 2/(c_g a_g^2 \sqrt{3}/2)$). The density of bulk carbon is $\rho_{CB} = 4/(a_{\mathrm{SiC}} \sqrt{3}/2 c_{\mathrm{SiC}})$. To estimate the buffer and monolayer coverage, the S_1, $S_2$and ML integrated intensities are summed together to obtain the total graphene photoemission intensity. Note that the absolute thickness with this model can vary up to 20-40% due errors in model parameters. What is more important are the trends demonstrated on a relative scale.

It can be seen that the buffer coverage quickly approaches uniform coverage. Below 1377°C , no substantial buffer components are observed. With only an increase in growth temperature of 20°C , a near complete buffer coverage formed. Such a drastic change is not observed for monolayer growth. Rather graphene coverage starts developing around

1430°C and gradually approaches a full monolayer coverage around 1500°C . Since XPS measures photoemission from a large area, it is not necessarily the case that a predicted monolayer thickness consists of a homogeneous monolayer surface. It could also be the case that there is some fraction of the surface with monolayer coverage and another lesser fraction of bilayer graphene. This is not the case for the buffer layer because Raman results showed no observable 2D peak. However, when monolayer growth occurs, it can be seen that the 2D gradually becomes broader with increasing temperature, a telltale sign of bilayer coverage as the electron and phonon bands of the 2D peak split [103].

Raman demonstrated the buffer layer can be prepared such that little to no monolayer overgrowth was present. From Raman alone, it is difficult to obtain coverage estimates of the buffer layer. However, XPS was able to demonstrate that the buffer layer is nearly fully covered. More precise coverage estimates are presented in Chapter 5 using X-ray reflectivity. Furthermore, a small plateau around 1430°C exists slightly above the temperature when the buffer is fully covered, providing evidence for different activation energies for buffer growth and monolayer growth. By considering Raman and XPS together, a picture is painted that nearly a full buffer layer can be formed with minimal graphene overgrowth. This has important implications for studying functionalized graphene as well as producing better quality graphene samples, where hydrogen or oxygen intercalation could produce quasi-freestanding graphene with potentially superior properties.

CHAPTER 3

THE INCOMMENSURATE GRAPHENE-SIC(0001) PHASE

Incommensurate crystals (IC) have well ordered periodic distortions that cannot be related by integer multiples to their underlaying lattice. X-ray diffraction has been used to study IC structures for over forty years [108] and remain the ideal technique to study IC systems. Unlike real space probes like STM, x-ray diffraction can precisely measure both absolute and relative small deviations from commensurate lattices.

This chapter demonstrates that the buffer graphene lattice constant and the SiC interface are incommensurate (IC), not the commensurate $6\sqrt{3}$ reconstruction assumed for the past forty years [40]. This is accomplished by quantifying the IC distortion through the first high resolution surface X-ray diffraction (SXRD) measurements of the buffer-SiC(0001) structure. Precise SXRD measurements of the in-plane surface structure were made possible by improvements in the coherent domain size to double that of previous works [58, 109].

3.1 Experimental

The substrates used in these studies were n-doped CMP polished on-axis 4H-SiC(0001) provided by Cree. The graphene was grown in a confinement controlled silicon sublimation (CCS) furnace [37]. In the CCS method, graphene growth is a function of temperature, time, and crucible geometry that sets the silicon vapor pressure. With the current crucible design, a single semiconducting buffer graphene (referred to as BG_o) layer grows at a temperature of 1400°C - 1420°C for 30 min. At these growth conditions the ARPES spectra is qualitatively different from growth temperatures below 1380°C and UHV grown samples [62, 36, 110]. UHV buffer is characterized by two flat bands at 0.5 and 1.6 eV that span the entire Brillion Zone (BZ), whereas CCS buffer shows two dispersive bands. The difference

was attributed to an increase in layer uniformity and growth at quasi equilibrium conditions possible in the CCS method. In this study, I focus on the properties of the newly discovered semiconducting buffer.

Monolayer graphene (referred to as ML) will grow above a buffer layer at 1550°C - 1570°C in 20 min. An important note is that once the ML grows, a new buffer layer (referred to as BG_{ML}) forms below ML. As I will demonstrate, the buffer graphene with and without a ML layer above it is structurally different. The BG_o and ML samples were characterized by Raman spectroscopy and LEED and give results similar to Fromm *et al.* [100] and Emtsev *et al.* [36].

SXRD measurements were conducted at room temperature under UHV at the SIXS beamline at SOLEIL Synchrotron using a photon energy of $h\nu = 12.8$ keV. The angle of incidence was fixed at 0.1° (near the critical angle) to optimize the scattered intensity. The momentum transfers, $\mathbf{Q} = \mathbf{k}_f - \mathbf{k}_i$, are written in terms of the bulk hexagonal SiC lattice parameters: $\mathbf{Q} = h\mathbf{a}^*_{\text{SiC}} + k\mathbf{b}^*_{\text{SiC}} + l\mathbf{c}^*_{\text{SiC}}$ where $a^*_{\text{SiC}} = b^*_{\text{SiC}} = 2\pi / \left(a_{\text{SiC}}\sqrt{3}/2\right) = 2.3556\mathring{A}^{-1}$ and $c^*_{\text{SiC}} = 0.6233\mathring{A}^{-1}$. $\mathbf{Q} = (h, k, l)$ represents a point in reciprocal space using SiC reciprocal lattice units (r.l.u.). Polarization and geometric corrections [75] were performed to compare integrated intensities. Prior to X-ray exposure, the samples were heated to 500°C in UHV to remove surface contaminants.

ARPES measurements were made at the Cassiopée beamline at the SOLEIL synchrotron. Measurements on both samples were performed at 90 K. The Fermi energy, E_F, was determined from the k-integrated intensity cutoff of the molybdenum sample holder to within 20 meV for each sample. $h\nu = 70$ eV.

3.2 The Incommensurate SiC(0001) Interface

In the traditional buffer layer picture, the commensurate $6\sqrt{3}$ structure gives rise to 6^{th} order diffraction rods around the bulk SiC reciprocal lattice rods at the positions $\left(0, \frac{5}{6}, l\right)$ and $\left(0, \frac{7}{6}, l\right)$ [see the insert in Figure 3.1(a)]. However, high resolution SXRD measure-

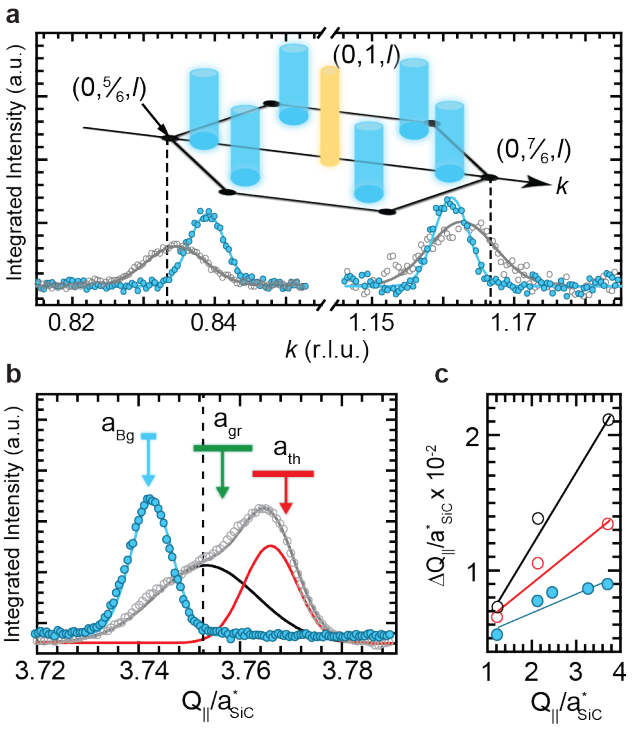

Figure 3.1: Diffraction results from the incommensurate graphene-SiC(0001) systems. (a) SXRD radial k scans, $(0, k, 0.1)$, around the SiC $(0, 1, l)$ rod (see schematic in the insert). The background-subtracted intensity is instrument corrected. Data is for the BG_o (blue) and ML (gray) films. Dashed lines mark the commensurate $5/6^{\text{th}}$ and $7/6^{\text{th}}$ positions in reciprocal space (black circles in insert). The buffer satellite rods are contracted relative to the commensurate positions towards the $(0, 1, l)$ rod while the monolayer rods are nearly commensurate. (b) Radial scan through the nominal graphene $(0, 3, 0.1)_G$ rod for the BG_o (blue ∘) and ML (gray ∘) films. Dashed line marks the expected position for a commensurate $6\sqrt{3}$ graphene film. Blue arrow shows the expected $(0, 3, l)_G$ position from Eq. 3.6. The monolayer film has a contribution from the ML (red line) and the BG_{ML} rods (black line). The green (red) arrow marks the position for graphite (theoretical graphene). The arrows' horizontal bar represent their known uncertainties. (c) Radial width of graphene rods as a function of $Q_{\|}$ for BG_o (blue ∘), ML (red ∘), and BG_{ML} (black ∘).

ments reveal that the satellite rods are symmetrically shifted away from the commensurate 6^{th} order positions and towards the bulk $(0, 1, l)$ rod. The incommensurate rods along k in Figure 3.1(a) are $\pm\mathbf{q}_1 = \mathbf{Q} - \mathbf{G}_{0,1}^{\text{SiC}}$ whose magnitude is $q_1 = q_o a_{\text{SiC}}^*$, where $q_o = 1/6(1+\delta)$ and $\delta = 0.037(2)$.

This behavior is a classical result of a modulated incommensurate system [112]. The modulation may be a chemical or displacement modulation. For the moment a displacement modulation is considered. For displacement modulation, the contracted satellite positions are a direct result of the commensurate unit cell positions, $\mathbf{R}$, being modulated by a function, $\boldsymbol{\eta}(\mathbf{R}, \mathbf{q})$. The modulation can be Fourier expanded so that the new modulated positions, $\mathbf{r}$, are given by [113],

$$\mathbf{r} = \mathbf{R} + \sum_{j=1}^{d} \boldsymbol{\eta}_j \sin\left(\mathbf{q}_j \cdot \mathbf{R} + \phi_j\right). \tag{3.1}$$

Each Fourier component has a corresponding amplitude $\boldsymbol{\eta}_j$, wavevector $\mathbf{q}_j$, and phase ϕ_j. The number of Fourier components is d. From this description the diffraction condition and intensity can be calculated. In the kinematic approximation the scattering amplitude is,

$$A(\mathbf{Q}) = \sum_{\mathbf{r}} f_{\mathbf{r}} e^{i\mathbf{Q}\cdot\mathbf{r}}, \tag{3.2}$$

where $f_{\mathbf{r}}$ is the atomic form factor of the atom at position $\mathbf{r}$. Substituting eq. 3.1 into eq. 3.2 and using the Jacobi-Anger expansion $e^{iZ\sin\theta} = \sum_{p=-\infty}^{\infty} e^{ip\theta} J_p(Z)$, where $J_p(Z)$ is a Bessel function of the first kind, gives,

$$A(\mathbf{Q}) = F(\mathbf{Q}) \sum_{\mathbf{R}_{l,l'}} \sum_{\{p_j\}=-\infty}^{\infty} e^{i(\mathbf{Q}+\sum_j p_j \mathbf{q}_j)\cdot\mathbf{R}_{l,l'}} e^{i\sum_j p_j \phi_j} \prod_{j=1}^{d} J_{p_j}(\mathbf{Q}\cdot\boldsymbol{\eta}_j). \tag{3.3}$$

$F(\mathbf{Q}) = \sum_{\mathbf{R}_b} f_{\mathbf{r}} e^{i\mathbf{Q}\cdot\mathbf{R}_b}$ is the average structure factor from the basis atoms, $\mathbf{R}_b$ and is assumed to be slowly varying in subsequent calculations. The integrated intensity is calculated from the scattering amplitude by $I = \int d^3Q |A(\mathbf{Q})|^2$. Using the substitution

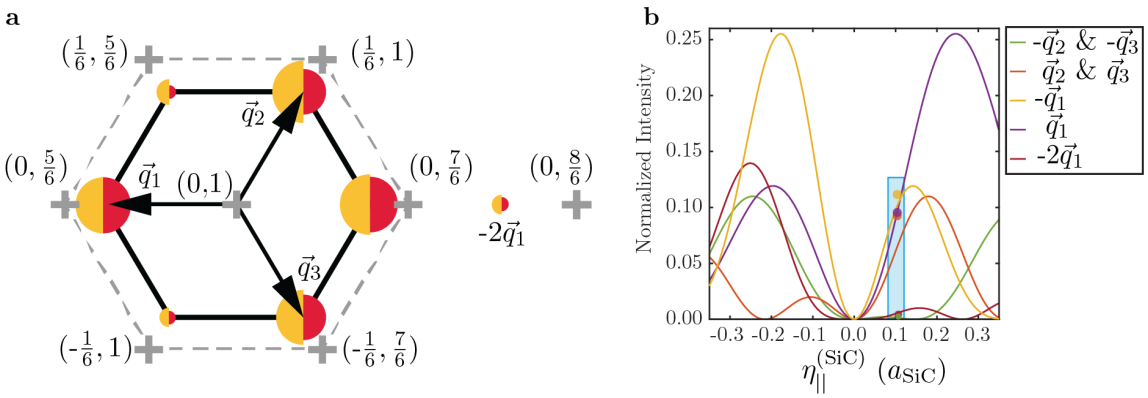

Figure 3.2: SXRD derived structure of the buffer-SiC interface. (a) The instrument corrected integrated intensity of the satellite rods around the $(01l)$ rod. Crosses mark the commensurate 6^{th} order rods. The arrows show the three IC wavevectors. The gold circle's area are proportional to the measured intensity of the satellite rods. The red circle's area are proportional to the fit intensity described in the text for $\eta^{(\mathrm{SiC})} = 0.11 a_{\mathrm{SiC}}$. (b) The $\eta_{||}^{(\mathrm{SiC})}$ dependence of the calculated intensity for the satellite rods shown in (a). The intensity is normalized to N^2. The vertical blue box shows the range of $\eta_{||}^{(\mathrm{SiC})}$ that best fit the measured values of all seven rods. The circles represent the normalized experimental intensity values for the satellite rods.

$\mathcal{R} = \mathbf{R} - \mathbf{R}'$, I find the restriction $\sum_j^d p_j \mathbf{q}_j = \sum_{j'}^d p_{j'} \mathbf{q}_{j'}$, denoted as $\langle \{p_j\}\{p_{j'}\} \rangle$, and the diffraction condition,

$$\mathbf{Q} = \mathbf{G} - \sum_j^d p_j \mathbf{q}_j, \tag{3.4}$$

where $\mathbf{G}$ is a reciprocal lattice vector of the SiC ($\mathbf{G}^{(\mathrm{SiC})}$) or graphene ($\mathbf{G}^{(\mathrm{g})}$) unmodulated lattice, and $\{p_j\}$ is a set of integers for the corresponding $\mathbf{q}_j$. The presence of incommensurate modulation allows diffraction at new positions in reciprocal space. Each incommensurate wavevector effectively increases the dimensionality of the system. The diffraction intensity subject to the constraint, $\sum_j^d p_j \mathbf{q}_j = \sum_{j'}^d p_{j'} \mathbf{q}_{j'}$, is,

$$\frac{I(\mathbf{Q})}{N^2 |F(\mathbf{Q})|^2} = \sum_{\langle \{p_j\}\{p_{j'}\} \rangle} \prod_{j,j'}^d J_{p_j}(\mathbf{Q} \cdot \boldsymbol{\eta}_j) J_{p_{j'}}(\mathbf{Q} \cdot \boldsymbol{\eta}_{j'}) e^{i(\sum_j^d p_j \phi_j - \sum_{j'}^d p_{j'} \phi_{j'})} \tag{3.5}$$

The modulation amplitude in the SiC interface layer and the buffer graphene layer can be quantified by comparing the measured, instrument corrected [75], integrated intensity of the incommensurate satellite rods to the calculated intensity. The intensity was numerically

calculated with a large number of lattice points by inserting eq. 3.1 into 3.3. To obtain a meaningful estimate of the modulation, the number of terms in $\boldsymbol{\eta}(\mathbf{R}, \mathbf{q})$ must be limited. Experimentally, the satellite rods of significant intensity were first order. The minimum number of wavevectors needed to reproduce the symmetry of the satellites was found to be $d = 3$. The three $\{\mathbf{q}\}$ are shown in Figure 3.2(a). They are of equal magnitude and directed along $\mathbf{q}_1 = -q_o\mathbf{b}^*_{\text{SiC}}$, $\mathbf{q}_2 = q_o\mathbf{a}^*_{\text{SiC}}$, and $\mathbf{q}_3 = q_o(\mathbf{b}^*_{\text{SiC}} - \mathbf{a}^*_{\text{SiC}})$. Note that from the non-orthogonality of $\{\mathbf{q}\}$, there are multiple sets of $\{p\}$ for a given satellite rod that contribute to the diffraction intensity. For example, $-\mathbf{q}_1 = \mathbf{q}_2 + \mathbf{q}_3$ and satisfies the restriction $\langle\{p_j\}\{p_{j'}\}\rangle$. From symmetry considerations, the modulation amplitudes, $\{\boldsymbol{\eta}\}$, are assumed to have the same magnitude, $\eta^{(\text{SiC})}$ or $\eta^{(\text{g})}$, and parallel to their respective $\{\mathbf{q}\}$. Multiple orientations for the modulation amplitudes were tested and these choices were found to provide the best fit. Further, the intensity was found to be insensitive to the choice of $\{\phi\}$.

Figure 3.2(b) shows how the calculated intensity of the satellite rods around $\mathbf{G}^{(\text{SiC})}_{0,1}$ vary as a function of $\eta^{(\text{SiC})}$. The intensity was normalized to N^2, where N is the number of lattice points in the numerical calculation. When $\eta^{(\text{SiC})} \to 0$, $I \to 0$ for all satellite rods and $I \to 1$ at $\mathbf{Q} = \mathbf{G}$. As $\eta^{(\text{SiC})}$ increases, the intensity is not symmetric in $\eta^{(\text{SiC})}$ about zero and the satellite intensities develop an asymmetry like the observed experimental pattern [see Figure 3.2(a)]. The range of $\eta^{(\text{SiC})}$ with the proper intensity pattern is highlighted by the blue box in Figure 3.2(b). The best fit value is $\eta^{(\text{SiC})} = 0.11(4)a_{\text{SiC}}$. The same analysis was performed on the graphene satellites and found a weak, but non-zero, in-plane modulation of $\eta^{(g)} < .01a_{\text{SiC}}$.

The incommensurate modulation can be visualized by plotting the relative density change of the SiC interface layer. By considering eq. 3.1 as a coordinate transformation, the normalized density change relative to the unmodulated system is given by $\Delta\rho/\rho = J^{-1} - 1$, where J^{-1} is the inverse of the Jacobian determinant for the transformation of $\mathbf{R} \to \mathbf{r}$. The color map in Figure 3.3 shows that the SiC interface consists of a super-hexagonal network

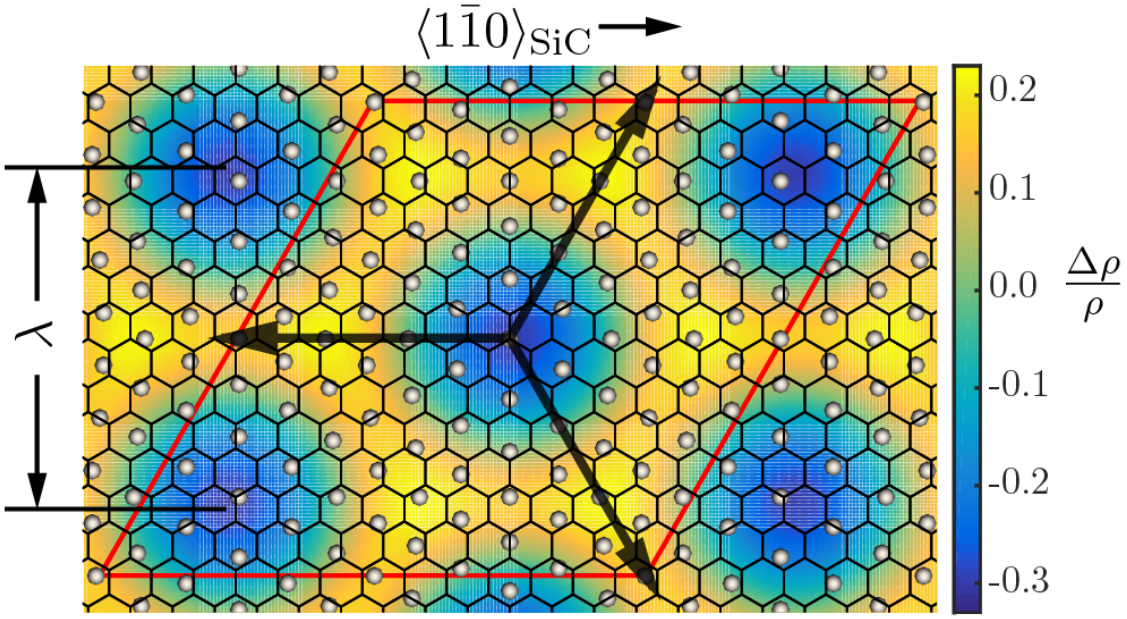

Figure 3.3: Relative density $\Delta\rho(x,y)/\rho$ map of the incommensurate SiC interface using the measured $\{\mathbf{q}\}$ and best fit $\eta_{||}^{(\mathrm{SiC})}$. The gray circles and hexagonal mesh overlay represents interface Si and graphene, respectively. The commensurate $6\sqrt{3}$ unit cell is marked in red. Black arrows show the three incommensurate wavevectors.

with a period of $\lambda = 6(1+\delta)a_{\mathrm{SiC}}$. The boundaries have a higher density than bulk terminated SiC. Note that while the density modulation is periodic, the atomic positions of both the SiC interface and the buffer graphene are not periodic. The network is very similar to STM images of the buffer layer [43, 53, 56, 52].

The exact structure of the SiC interface and the driving force for the incommensurate phase remains to be determined. It is unlikely that a simple sinusoidal modulation used to fit the data is the complete picture. Recent work by Emery et al. [63] may provide a clue. They show that the interface layer below the buffer graphene layer has a lower Si and higher C concentrations than bulk SiC. Silicon vacancies and/or substitutional carbon could give rise to different bonding geometries that could produce strains sufficient to drive the incommensurate modulation. On the other hand, a comparable strength of in-plane and interlayer interaction coupled with subsequent changes in bond length may be sufficient to drive the incommensuration in a bulk-terminated system.

3.3 Incommensurate Mutual Modulation of Graphene and the SiC Interface

What is unique about the buffer system is that not only is the buffer graphene lattice constant incommensurate [see Figure 3.1(b)], but a new periodicity (q_o) is present that is also incommensurate with both the buffer graphene and bulk SiC. The emergence of q_o and its relation to the buffer graphene and SiC lattice parameter can be understood not as a Moiré period but in the context of mutual modulation. Moiré patterns and periodicities result from commensurate rotations of lattices with similar [114] or different [115] lattice parameters. The periodicity that arises in the buffer/SiC system is not consistent with a Moiré pattern. The smallest commensurate approximation found near the experimental $\delta = 0.037(2) \approx 1/24$ estimates a Moiré period of ~ 13.3 nm resulting from a $(54 \times 54)_g$ supercell. This is not consistent with the experimental $\lambda \approx 1.9$ nm. An incommensurate crystal will have no true Moiré period. Moreover, an x-ray diffraction measurement exhibiting only a Moiré pattern would show no satellite diffraction rods. The appearance of periodicity in a modulated system differs from a Morié period in that the modulation arises from a periodic displacement or composition distortion as opposed to a superlattice commensuration of two undistorted lattices. Lattice distortions arise when the interlayer interaction is of sufficient strength to alter the natural bonding configuration of the primitive crystal.

Insight into the origin of q_o can be gained from two unique observations. A schematic of the diffraction pattern observed with SXRD is shown in Figure 3.4(a). Figure 3.4(b) shows that $\mathbf{G}^{(\mathrm{g})}_{1,1}$ rod is exactly coincident with an incommensurate satellite rod $\mathbf{G}^{(\mathrm{SiC})}_{0,2} - \mathbf{q}_1$. Moreover, the diffraction rod is well described by a single peak with no observable shoulders. In other words, the spacing between the buffer $\mathbf{G}^{(\mathrm{g})}_{1,1}$ and the SiC $\mathbf{G}^{(\mathrm{SiC})}_{0,2}$ is an incommensurate wavevector, i.e. $\mathbf{q}_1 = \mathbf{G}^{(\mathrm{SiC})}_{0,2} - \mathbf{G}^{(\mathrm{g})}_{1,1}$ [see Figure 3.4]. Furthermore, the same set of modulation wavevectors observed around SiC reciprocal lattice vectors is also observed about the graphene reciprocal lattice vectors. These observations allow the generalization

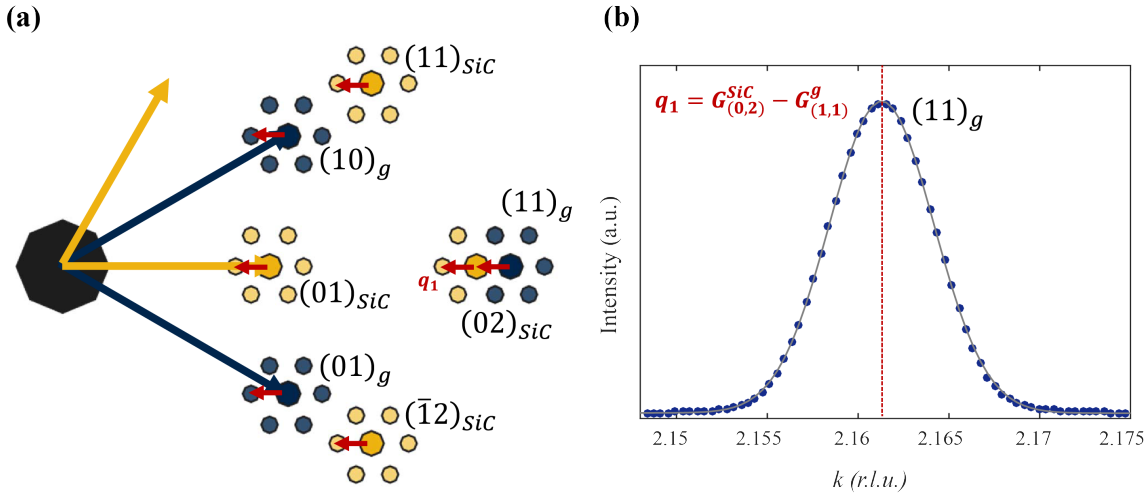

Figure 3.4: Mutual modulation of graphene and SiC. (a) Schematic of reciprocal space for the buffer graphene-SiC system. The large filled blue (red) circles represent the SiC (graphene) reciprocal lattice rods. The small blue (red) circles represent the SiC (graphene) satellite rods. (b) SXRD radial k scan, around the buffer graphene $(1, 1, l)$ rod of BG_o film. The solid blue line represents the expected position of the of the incommensurate wavevector from the SiC $(0, 2, l)$ rod. The position is exactly coincident of the the buffer graphene $(1, 1, l)$. The result is a direct consequence of mutual modulation between buffer graphene and SiC.

that equation 3.4 can be rearranged such that the set of allowed principal incommensurate wavevectors $\{\mathbf{q}\}$ for both graphene and the SiC interface can be described by the difference of graphene and SiC reciprocal lattice vectors,

$$\{\mathbf{q}\} = \{\mathbf{G}^{(\mathrm{SiC})} - \mathbf{G}^{(\mathrm{g})}\}. \tag{3.6}$$

This result indicates that by measuring $\mathbf{q}$, the graphene lattice constant can be determined. If $\mathbf{q}_1 = \mathbf{G}^{(\mathrm{SiC})}_{0,2} - \mathbf{G}^{(\mathrm{g})}_{1,1}$ is solved for the graphene lattice parameter, the following relationship predicts the buffer graphene lattice parameter,

$$a_{bg} = a_{\mathrm{SiC}} \frac{6\sqrt{3}(1+\delta)}{13+12\delta}. \tag{3.7}$$

Based off of the experimentally determined $\delta = 0.037(2)$, the lattice parameter of the buffer layer is predicted to be 2.469(4) Å. This value is in exact agreement with the measured

lattice constant of 2.469(3) Å[see Table 3.1]. As a visual confirmation, Figure 3.1(b) shows the excellent agreement between the measured and expected ($\mathbf{G}^{(\mathrm{g})}_{0,3} = \mathbf{G}^{(\mathrm{SiC})}_{1,1} - \mathbf{q}_1 + \mathbf{q}_2$) position of the buffer $\mathbf{G}^{(\mathrm{g})}_{0,3}$.

These experimental consequences arise naturally from the concept of mutual modulation. To understand the origin of equation 3.6, consider the interaction of a monolayer of graphene with the SiC interface. The equilibrium atomic positions of the graphene atoms can be Fourier expanded in terms of the SiC periodicities,

$$\mathbf{r}_g = \mathbf{R}_g + \sum_{\mathbf{G}^{(\mathrm{SiC})}} \boldsymbol{\eta}^{(g)}_{\mathbf{G}^{(\mathrm{SiC})}} \sin\left(\mathbf{G}^{(\mathrm{SiC})} \cdot \mathbf{R}_g\right), \tag{3.8}$$

similar to equation 3.1 where instead of an arbitrary $\mathbf{q}$, the modulation wavevectors are $\mathbf{G}^{(\mathrm{SiC})}$. The alternate situation is also true that the graphene may distort the SiC. In this situation the SiC atomic positions must be written in terms of the graphene periodicities,

$$\mathbf{r}_{\mathrm{SiC}} = \mathbf{R}_{\mathrm{SiC}} + \sum_{\mathbf{G}^{(\mathrm{g})}} \boldsymbol{\eta}^{(\mathrm{SiC})}_{\mathbf{G}^{(\mathrm{g})}} \sin\left(\mathbf{G}^{(g)} \cdot \mathbf{R}_{\mathrm{SiC}}\right), \tag{3.9}$$

By examining the diffraction resulting from a system modeled by equation 3.1, it is clear for this situation that the diffraction conditions for the graphene and SiC are $\mathbf{Q} = \mathbf{G}^{(\mathrm{SiC})} - \sum_j p_j \mathbf{G}^{(g)}$ and $\mathbf{Q} = \mathbf{G}^{(g)} - \sum_j p_j \mathbf{G}^{(\mathrm{SiC})}$, respectively. However, this is not the diffraction pattern observed and defined by equation 3.6. To understand how a $\mathbf{q}$ can be a *difference* of $\mathbf{G}^{(\mathrm{SiC})}$ and $\mathbf{G}^{(g)}$, it must be recognized that $\mathbf{q}$ is necessarily *modulo* $\mathbf{G}$. For example, consider the substitution $\tilde{\mathbf{q}} = \mathbf{G}^{(g)} + \mathbf{G}^{(\mathrm{SiC})}$ into equation 3.8. The result is,

$$\mathbf{r}_g = \mathbf{R}_g + \sum_{\mathbf{G}^{(\mathrm{SiC})}} \boldsymbol{\eta}^{(g)}_{\mathbf{G}^{(\mathrm{SiC})}} \sin\left(\tilde{\mathbf{q}}^{(SiC)} \cdot \mathbf{R}_g - \mathbf{G}^{(\mathrm{g})} \cdot \mathbf{R}_g\right), \tag{3.10}$$

where clearly $\mathbf{G}^{(\mathrm{g})} \cdot \mathbf{R}_g = 2\pi n$. Since $\sin(\theta + 2\pi n) = \sin\theta$, the addition of $\mathbf{G}^{(g)}$ has no effect on the modulation. Substituting $\tilde{\mathbf{q}}$ into equation 3.9 amounts to the same result. From this analysis it can be seen that the $\mathbf{q}$ from equation 3.6 and $\tilde{\mathbf{q}}$ are equivalent. Therefore,

this shows us that the experimentally observed diffraction pattern is a result of mutual modulation, i.e. the SiC interface modulates graphene and graphene modulates the SiC interface. Since $\mathbf{G}^{(g)}$ and $\mathbf{G}^{(\mathrm{SiC})}$ are incommensurate, $\tilde{\mathbf{q}}$ will generate a new periodicity that is incommensurate from both graphene and SiC.

Such a result is important because it provides information on the type of incommensurate system that is present in the graphene/SiC interface. One type of incommensurate system is when the interaction between two naturally incommensurate crystals is weak. If their interaction is sufficiently weak, their incommensuration is maintained. This is not the case for the buffer-SiC interface. If it were, no satellite rods would be measured. The fact that modulation rods occur about both $\mathbf{G}^{(\mathrm{SiC})}$ and $\mathbf{G}^{(g)}$ indicates that the incommensuration results from competing interactions. The relevant and comparably strong interactions are inferred to be the σ-bonds in the buffer layer, the sp^3 C-Si bonds between the buffer layer and the interface silicon and the bulk C-Si bonds. If it were the case that one interaction was dominant, then the periodicity of that interaction would also dominate.

For a mutual modulation, the size of the set of modulation vectors, d, is determined by reciprocal lattice vectors, and therefore d approaches infinity. Furthermore, the incommensuration of the two layers means that the set of allowed diffraction positions in reciprocal space is nearly continuous. To determine the important modulation amplitudes and wavevectors would require theoretical calculations. However, it can also be addressed experimentally. Three principal modulation amplitude and wavevectors were identified and shown in Figure 3.3(a). The notion of mutual modulation predicts the existence of more and by searching for additional modulation vectors, a better understanding of the relevant types of interactions can be obtained. However, the striking resemblance to STM measurements suggests that the primary modulations have been identified [116, 60].

3.4 Incommensurate-Commensurate Phase Transition of Graphene on SiC(0001) and the Graphene Lattice Constant

In a mutual modulation, the incommensurate modulation inherently results from the incommensurate lattice parameter. The incommensurate buffer lattice constant is larger (2.469(3) Å) than the expected $6\sqrt{3}$ value if the buffer was commensurate with the $6\sqrt{3}$ (2.462 Å, vertical dashed line). This is demonstrated by the shift to lower $Q_{||}$ in Figure 3.1(b). Additionally, the lattice constant is larger than graphite (2.460(2) Å) and the range of theoretically predicted values for isolated graphene (2.455(3) Å) [11, 12, 13]. An increased lattice constant is consistent with stronger interlayer interaction in layered materials [10] and with the view that some of the carbon atoms bond lengths increase due to some degree of hybridization with Si in the SiC interface.

The first measurement of the buffer graphene lattice constant was by Schumann et al. with a reported lattice constant of 2.467Å[105]. This value is consistent with my measurement of 2.469Å. However, to reconcile their measured IC lattice constant with a commensurate $6\sqrt{3}$ cell Schumann et al. attempted (incorrectly) to use a vertically buckled graphene sheet locked into the $6\sqrt{3}$ reconstruction. In their supplemental material, they begin by asserting that a flat graphene layer should be commensurate with a $6\sqrt{3}$ unit cell. In order to accommodate the larger measured lattice constant into a commensurate SiC reconstructed $6\sqrt{3}$ cell, the buffer must develop a vertical corrugation like that observed in STM [60]. While there are a number of problems with their analysis (choosing a $(6 \times 6)_g$ graphene cell instead of the actual $(6\times6)_{\text{SiC}}$ cell for instance), their beginning assertion is fundamentally wrong for two reasons. First, in diffraction, the measured lattice constant is the average *in-plane* lattice constant. For the buffer graphene to be commensurate with a $(6\sqrt{3}\times6\sqrt{3})_{\text{SiC}}\text{R}30^\circ$ reconstruction, the in-plane buffer lattice constant would need to be $a_{\text{Bg}} = a_{\text{SiC}}6\sqrt{3}/13 = 2.462$Å, which it is not. Consequently, a commensurate $6\sqrt{3}$ system is excluded by both their measurement and ours.

This leads to the second reason their analysis is fundamentally wrong. Schumann et al.'s analysis of a periodically buckled graphene film is attempting to measure the bond modulation within the unit cell using only the integer order graphene rods. This is fundamentally impossible. In diffraction, the effects of vertical corrugation and/or in-plane bond length variations are contained in the structure factor of the unit cell. To measure the structure factor (and therefore the modulation of lattice constants), one must measure the **non-integer** order surface diffraction rods of the reconstructed surface. Since they found no non-integer order rods, it is impossible for them to make any assertion as to the graphene's reconstruction. The correlation of any structural model based on the SXRD measured average lattice constant alone is specious.

In fact the lack of non-integer order rods in their work point to a highly disordered surface that is typical of UHV grown epitaxial graphene. In my measurements, these other rods exist. We are therefore able to not only understand the origin of the average lattice constant, but can begin to describe the bond length variation of the buffer graphene layer and the SiC interface. In principle by analyzing the satellite rods as a function of in-plane and out-of-plane momentum transfers it is possible to get more information about the graphene distortion.

When a monolayer (ML) of graphene forms above the buffer layer, there are changes in the buffer's structure. The buffer with ML on top is distinguished as BG_{ML} from the bare buffer layer BG_o. Once the ML forms, the satellite positions and the lattice constant become nearly commensurate ($\delta < 0.02$) with the bulk SiC [See Figure 3.1(a) and (b)]. The ML lattice contracts relative to BG_{ML} making the ML incommensurate with both the BG_{ML} and SiC. The lattice constants for the buffer and ML systems are summarized in Table 3.1. Note that the ML lattice constant is nearly that of theoretically isolated graphene and contracted from graphite. In this case, the incommensuration along with the contraction from graphite is due to comparatively reduced interlayer interaction. Also, the ML interacts with only one layer and the incommensuration reduces the interlayer coupling compared to Bernal

Table 3.1: Comparisons of graphene lattice constants, their relative strain (Δa) compared to theoretical graphene, RMS strain ϵ_{rms}, and long range order

Graphene Form	Lattice constant (Å)	Δa (%)	ϵ_{rms} (%)	Order (nm)
Theoretical MG	$2.453(4)$[4]	-	-	-
Graphite	$2.460(2)$[5]	+0.28	-	-
BG_o	$2.469(3)$[1,3]	+0.70	0.2	60
BG_{ML}	$2.462(3)$[1,3]	+0.40	0.6	43
MG	$2.455(3)$[1,3]	+0.10	0.3	43
C-Face multilayer	$2.452(3)$[2]	-0.04	-	300

[a]This work
[b]From Ref. [50].
[c]Similar values were measured by Schumann et al., [105].
[d]From Ref. [11, 12, 13].
[e]From Refs. [7, 8, 9, 6].

stacking. This contraction is analogous to non-Bernal stacked graphene layers on C-face SiC [See Table 3.1].

The measured lattice constants show that graphene's intrinsic strain has been historically misinterpreted using Raman 2D peak positions. It has been clearly demonstrated that the Raman 2D peak of tensile strained graphene red shifts to lower wave numbers [117]. Since isolated graphene must be compressively strained relative to graphite [see Table 3.1], the 2D peak of true free standing graphene must be blue shifted relative to graphite as is the case for the 2D peak of graphene grown from SiC [99, 102, 118, 100]. The problem is that exfoliated graphene has its 2D peak shifted in the *wrong* direction (it is red shifted compared to graphite) [99, 102, 118, 100], which contradicts its historical reference as "free standing" graphene. Clearly the position of the 2D Raman peak in "free standing" graphene is due to some other cause that has yet to be explained.

There are two additional changes when the ML forms. First, the system becomes more disordered (30% decrease in long range order) as evidenced by the broader satellite rods in Figure 3.1(a). Also, the BG_{ML} develops a large RMS strain, ϵ_{rms}. RMS strain presents itself as Q-dependent broadening ($\epsilon_{\text{rms}} \approx \Delta Q/Q$). The plot of ΔQ vs. Q in Figure 3.1(c) shows that BG_{ML} has the largest slope, i.e. the largest ϵ_{rms}. The RMS strain in ML is smaller,

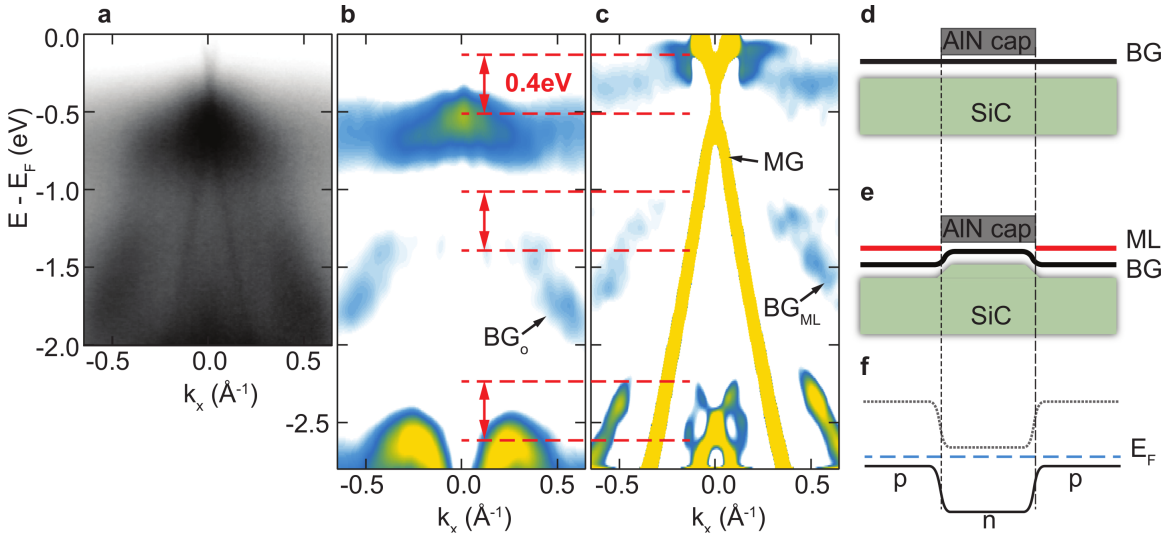

Figure 3.5: The effect of ML graphene growth on the buffer band structure. (a) ARPES bands at the BG_o layer K point (k_x is perpendicular to ΓK, $h\nu = 70$ eV). A Dirac cone from a 2% ML graphene layer is also visible. (b) A negative 2^{nd} derivative filter of the BG_o bands in (a). (c) A similar 2^{nd} derivative filter for a MG film. Red dashed lines mark the approximate 0.4 eV shift of the buffer bands. (d) Schematic of a negative AlN capping layer to locally prevent graphene growth. (e) Schematic of a pnp junction made by monolayer-buffer-monolayer junction where the buffer layer is a continuous film. (f) Schematic of the spatially varying bands from the structure in (e).

presumably due to strain relaxation allowed by weaker coupling to BG_{ML}. However, BG_o presents the lowest overall RMS strain.

It was assumed that the strong buffer-SiC interaction meant the buffer band structure did not change significantly once the ML formed. Now that a structure change in the buffer was demonstrated in Figure 3.1 upon ML formation, it is prudent to revisit how or if the BG_{ML} differs from BG_o. Figure 3.5(a) shows the ARPES spectra from the BG_o layer. The π-bands are broad ($\Delta k \sim 0.35$ Å^{-1}) consistent with $q \sim 0.38$ Å^{-1}. In order to compare the BG_{ML} bands with the BG_o, I plotted a 2nd derivative spectra of the buffer and ML bands in Figure 3.5(b) and (c). This compensates for both the Δk broadening and the photoelectron attenuations through the ML.

Figure 3.5(c) shows that the semiconducting π-bands are still present with the ML above. Although the BG_{ML} bands intensity is weak, it is consistent with a complete buffer layer after correcting for attenuation. There is, however a change in the BG_{ML} bands com-

pared to the BG_o bands. The π-bands are pushed to lower binding energy by ~ 0.4eV compared to the BG_o bands and the band near E_F appears to have less dispersion than the BG_o case. While there is a small energy gap between the BG_{ML} layer bands and E_F, the experimental error could also support the BG_{ML} layer being metallic [66]. It is also possible that the Dirac cone from ML is pinned at E_F from these flatter buffer bands. Note that $\eta^{(SiC)} < 0.05\ a_{SiC}$ (the uncertainty is due to the increased disorder in the BG_{ML}). The low value of $\eta^{(SiC)}$ is consistent with a buffer layer structure closer to the commensurate structure that would give rise to either a small gap or metallic bands. The fact that ML is incommensurate with BG_{ML} may provide new insight into why graphene grown on the Si-face has historically lower mobilities than C-face graphene[2, 118, 119] even though they have the same doping[120]. The only difference between the two is that the $(000\bar{1})$ system has no known buffer layer.

More importantly, the band changes in the BG_{ML} layer suggests a pnp junction device architecture by spatially controlling where MG is formed [see Figure 3.5(d), (e), and (f)]. By first growing a continuous buffer layer, a capping layer (AlN or SiN) mask is locally deposited to inhibit further graphene growth.[121, 122] The sample is then heated to grow MG outside of the masked area. This leaves a pnp junction as shown in Figure 3.5 where the capping layer remains as a gate insulator.

CHAPTER 4
TIGHT BINDING MODEL FOR THE ORIGIN OF INCOMMENSURATE SEMICONDUCTING GRAPHENE

The discovery of incommensurate mutual modulation in the graphene-SiC(0001) interface overturns the idea of the commensurate $(6\sqrt{3}\times6\sqrt{3})_{\text{SiC}}\text{R}30^\circ$ reconstruction assumed for the last forty years. Regardless of the exact structure, this discovery allows us to revisit and ultimately explain the origin of the buffer layer's electronic structure. Such a task is necessary as all previous calculations using the $6\sqrt{3}$ reconstruction have not described earlier [36] or more recent [62] ARPES measurements. In this chapter, a simplified model is developed for calculating the electronic structure resulting from incommensurate mutual modulation in graphene. To study the electronic structure of the incommensurate system, I formulate a tight binding model based on ab initio calculations[66]. Tight binding methods are often employed to study IC systems because of the large number of atoms involved. These IC calculations involve a "unit cell" arising from either a truncated lattice or by using a nearly commensurate lattice [123, 124, 125, 6, 114]. Although the Brillouin zone collapses in IC systems, delocalized dispersive states are still predicted for certain interaction configurations [125, 126]. Indeed ARPES measurements of IC systems still show "bands" [124]. The calculated band structure for the experimentally determined modulation is in excellent agreement with ARPES measurements of buffer graphene and indicates the importance of interface interaction in determining phyisical properties of the buffer layer.

4.1 Tight Binding Model of the Graphene-SiC Interaction

For all calculations, the buffer system is modeled as a graphene layer above a triangular lattice of Si atoms at the SiC surface. The Si lattice is rotated 30° from the graphene lattice vectors. Carbon atoms in the SiC are not included. The graphene atom positions are

defined, $\mathbf{R}_g(m,n) = m\mathbf{a} + n\mathbf{b} + \mathbf{R}_{A/B}$ with $\mathbf{R}_A$ at the origin, $\mathbf{R}_B = 1/3(\mathbf{b} - \mathbf{a})$ and $\mathbf{b}$ is rotated 120° from $\mathbf{a}$. A single orbital nearest neighbor tight binding model of the graphene π-electron network is employed to study the band structure. The Hamiltonian reads,

$$H = -t \sum_{\mathbf{R},\mathbf{R}'} \sum_{\langle i,j \rangle} \sum_{\mathbf{r}_{Si}} (a^{\dagger}_{\mathbf{R}+\mathbf{r}_i} a_{\mathbf{R}'+\mathbf{r}_j} + V\theta\left(r_{cut} - r_{Si}\right) a^{\dagger}_{\mathbf{R}+\mathbf{r}_i} a_{\mathbf{R}+\mathbf{r}_i} + H.c.), \tag{4.1}$$

where $\mathbf{R}$ ($\mathbf{R}'$) specifies the unit cell, $\mathbf{r}$ specify the C atom positions within the graphene unit cell, $\langle i,j \rangle$ represent that $\mathbf{R} + \mathbf{r}_i$ and $\mathbf{R}' + \mathbf{r}_j$ must be nearest neighbors to the carbon atom and r_{Si} represents the in-plane nearest neighbor distance for a Si atom in the interface layer to the graphene C at $\mathbf{r}_i$. $t \approx 3.0$ eV is the transfer integral between nearest neighbor C sites and $a^{\dagger}_{\mathbf{r}}$ ($a_{\mathbf{r}}$) are operators that create (annihilate) a carbon π-electron at $\mathbf{r}$. V is the onsite potential due to bonding from with a Si interface atom. $\theta\left(r_{cut} - r_{Si}\right)$ is the Heavyside step function that is 1 if $r_{Si} < r_{cut}$ and 0 otherwise. The Fourier transformation, $a_{\mathbf{r}} = 1/\sqrt{N} \sum_{\mathbf{k}} e^{i\mathbf{k}\cdot\mathbf{r}} \phi_{\mathbf{k}}\left(\mathbf{r}\right)$ is applied to the Hamiltonian, where $\phi_{\mathbf{k}}(\mathbf{r})$ is the operator that annihilates a p_z orbital at $\mathbf{r}$. After this transformation, the sums over $\mathbf{R}$ and $\mathbf{R}'$ are identical and the Hamiltonian becomes,

$$H = -t \sum_{\langle i,j \rangle} e^{i\mathbf{k}\cdot\boldsymbol{r}_{i,j}} \phi^{\dagger}_{\mathbf{k}}\left(\mathbf{r}_i\right) \phi_{\mathbf{k}}\left(\mathbf{r}_j\right) + V\theta\left(r_{cut} - r_{Si}\right) \phi^{\dagger}_{\mathbf{k}}\left(\mathbf{r}_i\right) \phi_{\mathbf{k}}\left(\mathbf{r}_i\right) + H.c., \tag{4.2}$$

where $\boldsymbol{r}_{i,j} = (\mathbf{R} + \mathbf{r}_i) - (\mathbf{R}' + \mathbf{r}_j)$. The solution to the Schrödinger equation is $|\Psi_n(\mathbf{k})\rangle = \sum_{\mathbf{r}} C^n_{\mathbf{r}} \phi^{\dagger}_{\mathbf{k}}\left(\mathbf{r}\right)$ where the coefficients are obtained from the solution to the eigenvalue problem, $\det[H(\mathbf{k}) - ES(\mathbf{k})] = 0$. The overlap of the p_z orbitals is assumed to be negligible. Therefore, the elements $S_{m,n} = \delta_{m,n}$. The matrix elements of the Hamiltonian are

$$H_{m,n} = -t \left(e^{i\mathbf{k}\cdot\boldsymbol{r}_{m,n}} \delta_{\mathbf{r}_m + \boldsymbol{r}_{m,n}, \mathbf{r}_n} + V\theta(r_{cut} - r_{Si}) \delta_{\mathbf{r}_m, \mathbf{r}_n} \right). \tag{4.3}$$

The method used to compare the calculated band structure with the ARPES is to project

the band structure from the supercell Brillouin Zone (BZ) to the larger primitive graphene BZ [127]. When unfolding the band structure, a weight is assigned to each eigenvalue at each k value;

$$W_n(\mathbf{k}) = \frac{1}{n}\left(\sum_{\mathbf{r}_{A,i}}\left(C^n_{\mathbf{r}_{A,i}}(\mathbf{k})\right)^*\sum_{\mathbf{r}_{A,i}}C^n_{\mathbf{r}_{A,i}}(\mathbf{k}) + \sum_{\mathbf{r}_{B,i}}\left(C^n_{\mathbf{r}_{B,i}}(\mathbf{k})\right)^*\sum_{\mathbf{r}_{B,i}}C^n_{\mathbf{r}_{B,i}}(\mathbf{k})\right). \quad (4.4)$$

Here $\mathbf{r}_{A/B}$ refer to C atoms in the larger unit cell that unfold to the A(B) sublattice. Neglecting effects such as polarization, photoelectron diffraction, etc., the ARPES intensity can then be approximated as;

$$I(E,\mathbf{k}) = \int\sum_{i}^{n} W_i(\mathbf{k})\delta(E - E_n(\mathbf{k}))dE. \quad (4.5)$$

Assuming the p_z orbitals are sufficiently localized, the wavefunction coefficients can also be used to model an STM measurement. This is done by calculating the charge density for a given energy [23],

$$\rho(\mathbf{r},E) = \int\sum_{n,\mathbf{k}} |C^n_{\mathbf{r}}(\mathbf{k})|^2\delta(E - E_n(\mathbf{K}))dE. \quad (4.6)$$

Both the ARPES intensity and charge density were broadened in energy by ± 0.1 eV to better represent the experimental measurements.

4.2 Incommensurate Graphene-SiC Model

In order to use a TB model for the graphene-SiC(0001) system, it is necessary to first properly set the TB onsite potential, V, the "unit cell", and the conditions that dertermines whether or not a Si in the interface bonds to a carbon atom in the graphene. The reason an onsite potential is used, rather than modifying the hopping parameter t is based off of the diffraction results. First it was seen that the $\eta^{(g)}$ was small. Changes in t are related to

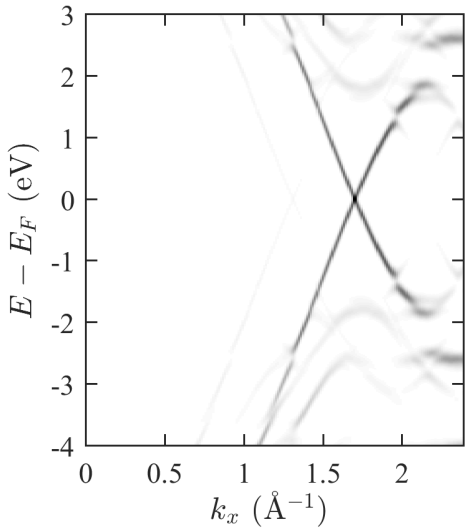

Figure 4.1: Band structure of strained graphene according to equation 3.1 with $\eta_g = .1a_{\text{SiC}}$. It can be seen that even at strains well above the experimentally determined value, band gaps do not form at the K-point.

changes in bond distance. Corrections to the hopping parameter are typically modeled as $t' = te^{-3.37l/a_o - 1}$ [28]. With this model it was found that large strains were necessary to open substaintial band gaps [28]. Furthermore, a stain model was tested and found no band gap formation for strains up to in excess of $\eta^{(g)} = 0.1a_{\text{SiC}}$, ten times larger than the strain estimate from the diffraction results [see Figure 4.1].

These results point to an onsite being the appropriate parameter. Also, it is common to model the substrate interaction with graphene by an on site potential [34, 128]. Furthermore, the electronic band structure from ab initio calculations found that the band structure near E_F was exclusively due to the graphene π-bands. Since I am interested in the ARPES measured band structure near E_F, it is sufficient to model only the graphene π-electrons and its interaction with the substrate through V. To determine the appropriate on-site potential V, V is set so that the TB calculations reproduce the results of ab initio calculations of Kim *et al.* [66] based on a graphene layer above a bulk terminated SiC(0001) surface. I begin by setting the conditions for a Si atom bond to a graphene C atom.

Previous ab initio calculations of the buffer layer assumed a $6\sqrt{3}$ bulk-terminated SiC interface was commensurate with a (13×13) graphene supercell [66]. The lattice vectors

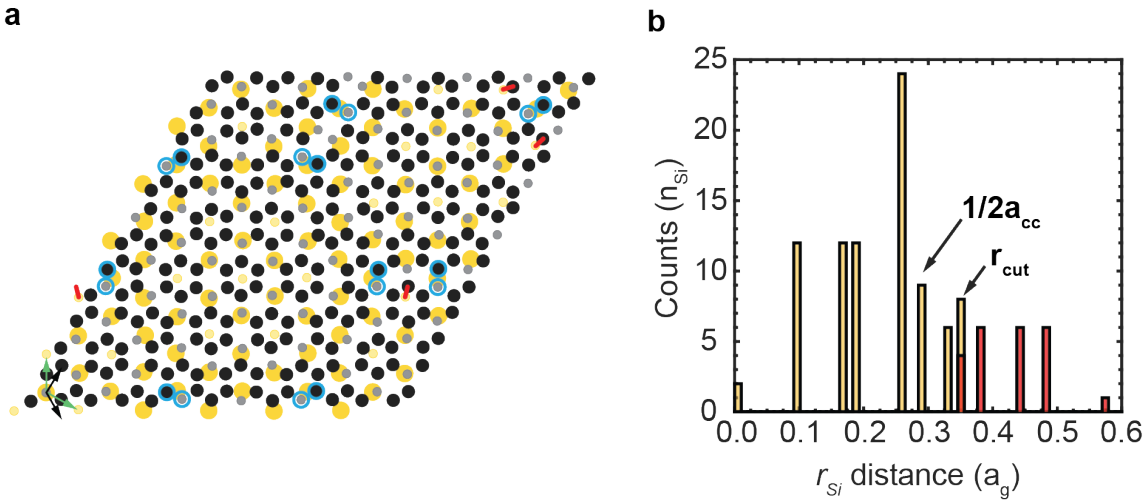

Figure 4.2: Bonding geometry from ab initio calculation [66]. (a) shows the bonding configuration of the $6\sqrt{3} \times 6\sqrt{3}R30^{\circ}_{\text{SiC}}$ or $(13 \times 13)_g$ unit cell do to an assumed unmodulated bulk-terminated SiC(0001) interface. The graphene lattice vectors are the black arrows, the SiC interface lattice vectors are the green arrows. The black (gray) circles are carbon atoms in the graphene layer bonded (did not bond) to Si. The large (small) yellow circles are Si atoms bonded (not bonded) to C in the graphene layer. The blue circles around a pair of C atoms are the same distance from the nearest Si within r_{cut}. The red lines indicate situations where bonding within r_{cut} did not occur. (b) Histogram counting the number of Si atoms with a nearest neighbor planar distances between Si in the interface layer and C in the graphene layer, r_{Si}. The yellow (red) histogram of r_{Si} is for bonded (not bonded) Si to graphene C atoms. The most notable feature is the overlap near $.34a_g$, which is highlighted in (a).

for graphene and SiC are shown in Fig. 4.2(a). In their calculations, the system was then allowed to relax from this initial configuration. Figure 4.2(a) and Figure 4.3(a) shows the predicted bonding pattern from the full DFT calculations. Not all Si in the interface bond to carbon in the graphene layer. They found that 79% of the interface Si atoms bind to 25% of the BG_o graphene C atoms. The bonding pattern is divided into two types: a nearly commensurate (NC) region and partially bonded carbon chains. In the NC region most of the carbon is bonded to silicon surface atoms, the remaining carbon in this region forms isolated benzene-like rings [see Fig. 4.3(a)]. The chains are an incomplete hexagonal network of carbon not bonded to the SiC. This network creates boundaries around the NC regions that are responsible for the bands near E_F [see Fig. 4.3(d)].[66]

Let r_{Si} be defined as the in-plane nearest neighbor distance between Si atoms and graphene carbon in the bulk terminated system. It turns out that r_{Si} is a good measure for identifying those Si atoms that ultimately bind to graphene carbon and those that do not after the system relaxed in the ab initio calculations. The histogram in Fig. 4.2(b) shows that if $r_{Si} > 0.35a_g$ the Si atom will not bond (a_g is the graphene lattice parameter). The maximum r_{Si} for bonding does not have a sharp cutoff, i.e. there are a few cases at the $r_{Si} = 0.35a_g$ boundary where bonding both did and did not occur (4 out of a total 85 carbon-SiC bonds). These cases are highlighted by red lines in Fig. 4.2(a). An additional complication occurs when $1/2a_{cc} < r_{Si} < .35a_g$, where a_{cc} is the C-C bond length in the graphene layer. In this case, two C atoms may be equidistant from the nearest Si atom. In the ab initio calculations, only one of the nearest C atoms bonded to Si. This is demonstrated by the blue circles in Fig 4.2(a). To avoid these complications, a cutoff radius $r_{cut} = 1/2a_{cc}$ is used for the incommensurate system. If the distance between Si and buffer C is less than r_{cut}, the TB calculation assumes that the two bond through the assignment of an onsite potential V.

The onsite potential, V, was chosen by comparing the TB results to the bands from the ab initio calculations. This was done by adopting the predicted bonding configuration of

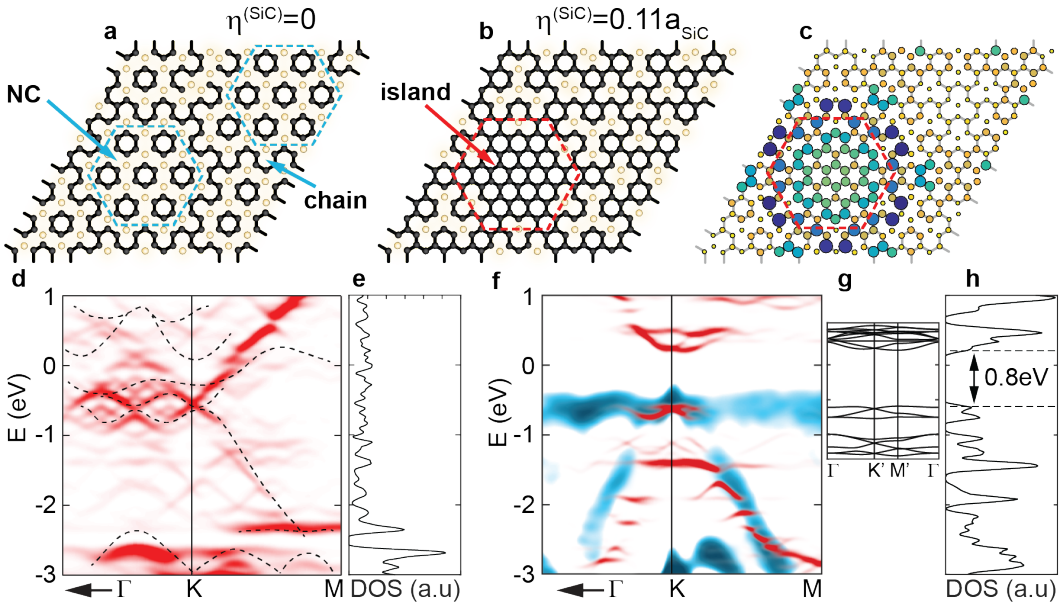

Figure 4.3: Comparison of the theoretical graphene band structure with experimental ARPES data. (a) The commensurate $6\sqrt{3}$ buffer structure derived from ab initio calculations in Ref. [66]. Black circles are carbon unbonded to the SiC. Gold circles are carbon bonded to Si in the interface layer below. The NC regions (blue hexagons) and the carbon chains are marked. (b) A model structure based on modulated SiC layer using the experimental value, $\eta^{(SiC)} = 0.11a_{\text{SiC}}$ (same color scheme as (a)). Red dashed hexagon marks the boundary of an isolated graphene island. (c) The calculated charge density[23] (arbitrary units) at $E = -0.6$ eV for the structure in (b). (d) TB bands (red) mapped onto the graphene BZ[127] from the commensurate structure in (a). The low energy bands from the ab initio commensurate structure are overlaid (black dashed line). (e) DOS for the TB bands in (d). (f) TB calculated bands (red) from the modulated structure in (b). The negative 2^{nd} derivative of the experimental ARPES bands (blue) are overlaid. The π-bands from a 2% monolayer have been subtracted from the experimental bands. (g) TB band structure in the unfolded $6\sqrt{3}$ BZ showing the mini-gaps in the π-bands that are observed in the experimental bands. (h) DOS for the TB bands in (f). The direct 0.8eV band gap is marked.

ab initio calculation, shown in Fig. 3(a) of the paper, for the TB calculations. A constant V was assigned to those C atoms in the graphene layer that were bonded to Si in the SiC surface. A large range of V were tested and the resulting band structure was compared with the ab initio band structure. It was found that $V \approx 4t \approx 12\ eV$ in the TB calculation best reproduced the ab intio bands and is comparable to the expected interaction strength [114]. The excellent agreement between the ab initio and TB band structure is shown in Fig. 4.3(d). While both calculations are in agreement, they clearly do not predict the ARPES experimental semiconducting bands plotted in Fig. 4.3(f).

Within this TB ansatz (with a similar r_{cut} and on-site potential), I explored the effect of an incommensurately modulated SiC lattice on the buffer's band structure. To isolate the effects of modulation (η^{SiC}) and incommensuration (q_o), I begin with modulating a commensurate $6\sqrt{3}$ unit cell. As expected, the bonding pattern is dependent on $\eta^{(\text{SiC})}$ and significant changes occur in the C-Si bonding configuration when the bulk terminated surface is modulated according to Eq. 3.1. As such, the band structure is also influenced by $\eta^{(\text{SiC})}$ due to the strong coupling between Si and C through the onsite potential. Figure 4.3(b) shows the bonding structure using the experimentally measured $\eta^{(\text{SiC})}$. The modulation and reduced r_{Si} decreases the number of Si bonds to the buffer graphene layer by nearly 40% compared to the commensurate unmodulated case in Fig. 4.3(a). Half of the NC regions in the commensurate structure converts into large regions of unperturbed graphene "islands." The location of the graphene island corresponds to the region of decreased Si interface density in Fig. 3.3. The graphene between the islands, aligned with the higher Si density boundaries in Fig. 3.3, have a much higher number of bonds to the interface Si as might be expected. The interface density modulation acts as a domain wall in the buffer graphene layer that breaks the bonding symmetry and opens a band gap.

The calculated semiconducting bands [see Fig. 4.3(f)] look remarkably similar to the measured ARPES bands for $\eta^{(\text{SiC})} = 0.11 a_{\text{SiC}}$ (the experimental value). Note that although lowest energy band shows a narrow bandwidth in the experimental 2^{nd} derivative ARPES

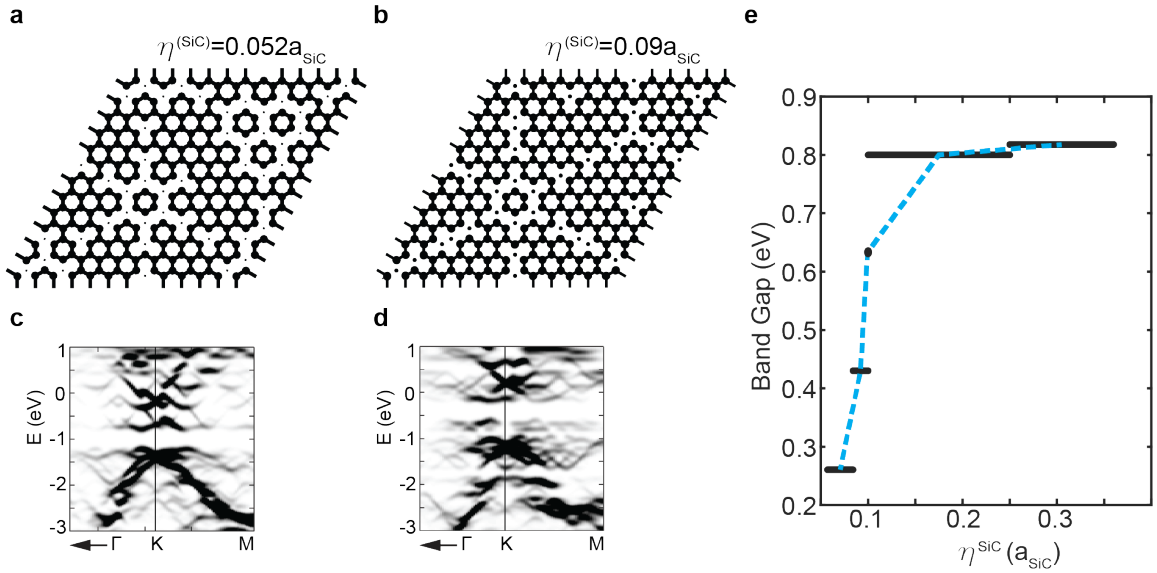

Figure 4.4: Bonding and band structure dependence on $\eta^{(\mathrm{SiC})}$. (a) and (b) The large (small) circles indicate unbonded (bonded) graphene to the Si below. As the modulation in the SiC interface increases the bonding configuration changes. At $\eta^{(\mathrm{SiC})} = 0.052a_{\mathrm{SiC}}$ shown in (a) the chain boundary of the unmodulated case broadened and opened a band gap of $0.26\ eV$ shown in (c). At $\eta^{(\mathrm{SiC})} = 0.09a_{\mathrm{SiC}}$ shown in (b) the bonding becomes more like graphene islands and a larger gap forms as shown in (d). (e) The calculated band gap as a function of $\eta^{(\mathrm{SiC})}$. As $\eta^{(\mathrm{SiC})}$ increases, the graphene "island" develops and the band gap increases to a value that appears to saturate. Dashed line shows the average value of $\eta^{(\mathrm{SiC})}$ that produces a given gap.

spectra, it is more dispersive perpendicular to ΓK.[62] The low BE experimental bands near K show a loss in spectral weight between ~ 0.6 to 1.5 eV. This is due to a mini-gap that forms in the π-bands. This is shown in the calculated π-bands plotted in the reduced zone shown in Fig. 4.3(g). The predicted gap is 0.8 eV as shown in density of states (DOS) in Fig. 4.3(g). The charge density from the three highest occupied bands in Fig. 4.3(f) show weak localization at the edges of the island [see Fig. 4.3(c)] and give rise to a charge density remarkably similar to STM measurements.[43]

In addition to the experimental $\eta^{(\mathrm{SiC})}$, the bonding and band structure was calculated for many other values of $\eta^{(\mathrm{SiC})}$ to develop an understanding of how $\eta^{(\mathrm{SiC})}$ influences the buffer band structure. The formation of islands and the opening of a band gap in the TB ansatz is robust in both q and η. The results are shown in Figure 4.4(a)-(d). The band gap increases as a function of $\eta^{(\mathrm{SiC})}$ becoming nearly constant for $\eta^{(\mathrm{SiC})}/a_{\mathrm{SiC}} \gtrsim 0.1$. The band gaps form over a large range of η's ($0.05 < \eta^{(\mathrm{SiC})}/a_{\mathrm{SiC}} < 0.36$) that includes the experimentally determined value of $\eta^{(\mathrm{SiC})}$. When $\eta^{(\mathrm{SiC})} < 0.10 a_{\mathrm{SiC}}$ the structure and band gap is sensitive to small changes in $\eta^{(\mathrm{SiC})}$ [see Fig. 4.4(e)]. However, even in this range the bonding configuration forms graphene "islands" that are sufficient to open band gaps $> 0.25\ eV$. When $\eta^{(\mathrm{SiC})}$ exceeds $0.10 a_{\mathrm{SiC}}$, a graphene "island" is fully formed and larger band gaps $> 0.8\ eV$ open. This configuration is stable and no significant change in bonding occurs up to $0.36 a_{\mathrm{SiC}}$. Note that the size of the band gap has nearly constant values over ranges of $\eta^{(\mathrm{SiC})}$'s [see Fig. 4.4(e)].

Finally, I have tested the effect of band gap formation with increasing $\eta^{(\mathrm{SiC})}$ in larger "incommensurate" supercells near the experimentally measured $q(\delta = 0.037)$ and confirmed that similar behavior is observed. Figure 4.5 shows the band structure of the unmodulated and experimentally modulated configuration for a $(54 \times 54)_G$ graphene unit cell. This is done by setting $\delta = 1/24$. It can be seen that the large unit cell gives rise to similar effects on the band structure as calculations based on the commensurate $6\sqrt{3}$ configuration. When the Si interface is unmodulated, a band structure similar to the calculations of [66] is

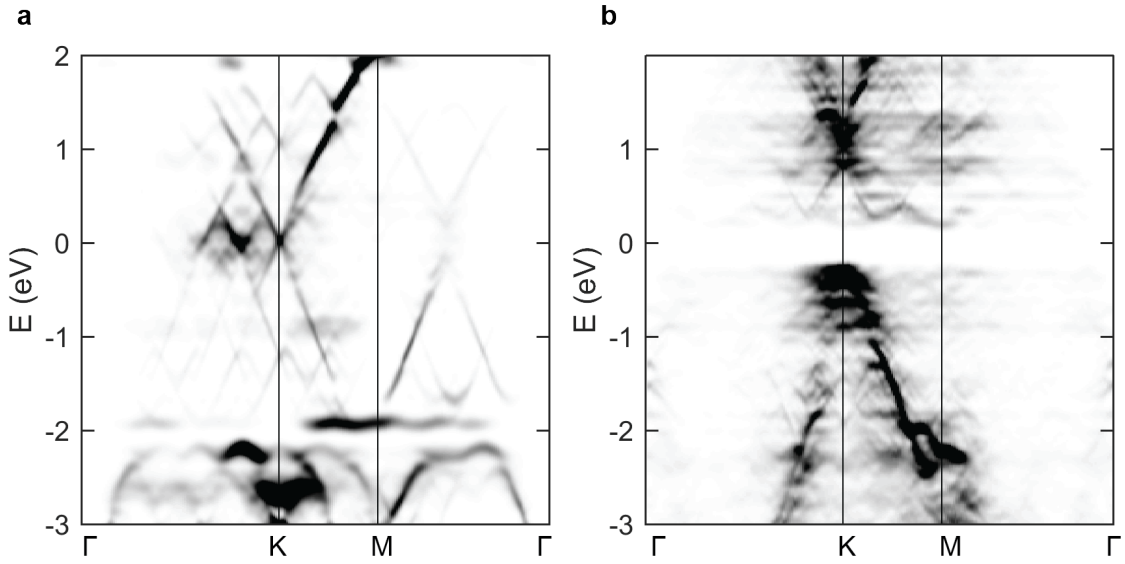

Figure 4.5: A comparison of the band structure between a modulated and unmodulated commensurate $(54 \times 54)_G$ structure for a $q(\delta = 1/24)$ close to the incommensurate $q(\delta = 0.037)$ surface (a) Band structure for $\eta_{\text{SiC}} = 0$. The unmodulated case resembles the band structure similar to [66]. (b) Band structure for the modulated supercell with $\eta_{\text{SiC}} = 0.12a_{\text{SiC}}$. The modulation opens a band gap of 0.45 eV and resembles the band structure of the buffer layer measured by ARPES.

observed. Also, the modulated case, $\eta^{\text{SiC}} = 0.12a_{\text{SiC}}$, opens a band gap of $\sim 0.5eV$ at the K-point similar to the experimental results.

The band structure for $\eta^{(\text{SiC})} = 0.11a_{\text{SiC}}$ and $q(\delta = 0.04)$ is shown in Fig. 4.6 over the whole range in reciprocal space and energy. In Fig. 4.6(b) the ARPES from BG_o in Fig. 4.6(a) is compared to the π and σ bands of graphene. The bands near E_F do not resemble the two nondispersive states seen in UHV grown buffer. Neither band extends through the whole Brillion zone and more detailed measurements demonstrated that one band disperses parallel to ΓK and another band disperses perpendicular to ΓK [62]. At higher binding energy, it can be seen that the ARPES π and σ bands have many splittings due to interaction with the SiC at $E - E_F$ below -2.5 eV. The π electrons in the carbon atoms of the buffer layer that do not interact with SiC are responsible for the low energy states as demonstrated in [66] and verified in my tight binding model. Therefore the tight

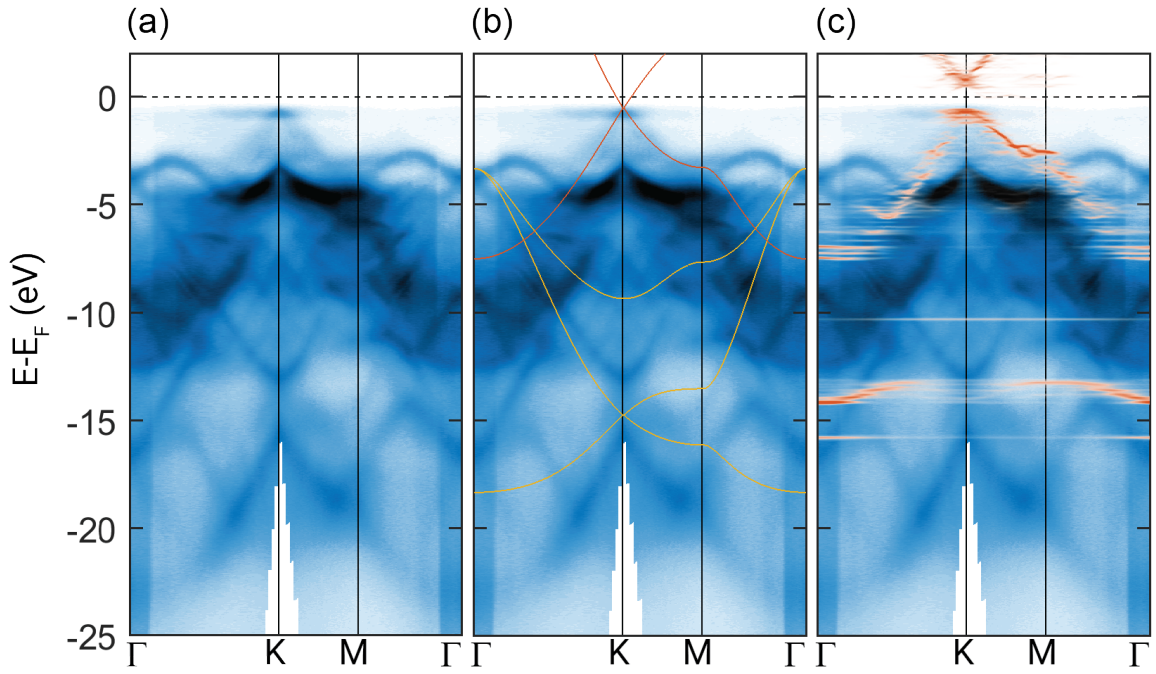

Figure 4.6: ARPES spectra of the buffer layer with $h\nu = 70$ eV. (a) Experimental data only showing the g_1 and g_2 states do not exist across the entire BZ. (b) Same as (a) with overlays of the TB bands of graphene. The graphene π-bands (red lines) and graphene σ-bands (yellow lines) are shown. The standard tight binding parameters from [5] were used for the calculations. (c) Same as (a) showing the calculated spectral weight (red) over layed on the experimental bands. The TB model uses the modulated structure with $\eta^{(\mathrm{SiC})} = 0.11 a_{\mathrm{SiC}}$.

binding model is justified for binding energies near E_F and provides qualitative agreement between experiment and theory as shown in Fig. 4.6(c) and the more detailed ARPES spectra shown in Figure 4.3. As the binding energy increases, the tight binding model does not account for all splittings because of more complicated interaction with the SiC interface, but nevertheless still reasonably follows the experimental bands.

4.3 Discussion

In addition to the SXRD derived incommensurate modulation providing a good description of the buffer band structure, the SXRD results also exclude other primary band gap opening mechanisms such as Kekulé distortions. A Kekulé distortion is a bond length alternation pattern that triples the size of the graphene unit cell [29, 129, 130]. Such distortions are

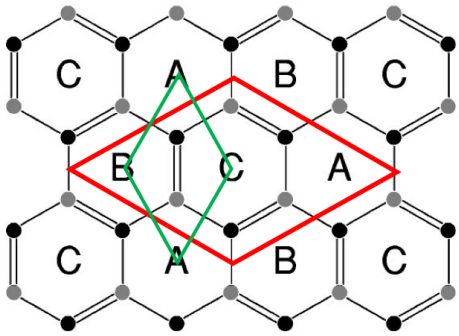

Figure 4.7: Crystal structure of a Kekulé distortion. The bond dimerization pattern triples the size of the unit cell and results in a $(\sqrt{3} \times \sqrt{3})_g$ unit cell, as shown by the red diamond. The green diamond is the primative graphene unit cell. The image is taken from ref. [29]

thought to arise from a peierls instability where a decrease in electronic energy from dimerization may outweigh the energy gain in elastic energy. Furthermore, it was recently shown that substrate interactions can induce Kekulé ordering [31] and it is therefore prudent to carefully consider this effect.

Figure 4.7 shows the bond alternation pattern of a Kekulé distortion. By tripling the size of the unit cell, the $K_{\pm}$-points of the graphene Brillion Zone are now reciprocal lattice vectors. To obtain the bond alternation, the A and B atoms of the graphene sublattice are modulated by a different wavevector,

$$\mathbf{r}_A = \mathbf{R}_A + \epsilon e^{i\mathbf{K}_+ \cdot \mathbf{R}_A} \tag{4.7}$$

$$\mathbf{r}_B = \mathbf{R}_B + \epsilon e^{i\mathbf{K}_- \cdot \mathbf{R}_B}, \tag{4.8}$$

where the real and imaginary components correspond to the x and y axis. It was shown that the band gap that forms from such a distortion can be large for relatively small ϵ and that there's no loss in generality by assuming a symmetric distortion, i.e. $\epsilon_A = \epsilon_B = \epsilon$ [29]. In the symmetric form, the band gap is,

$$E_g = 6\sqrt{3}\alpha t\epsilon / a_{cc} \tag{4.9}$$

where $\alpha \approx 3.7$ describes the change in hopping parameter, $t = 3$ eV, with bond length, $t' = te^{-\alpha\Delta a_{cc}/a_{cc}}$, where $a_{cc} = a_g/\sqrt{3} \approx 1.42$ Å is the undistorted graphene bond length. For this distortion, the bond length increase is the same magnitude as the bond length decrease for the dimerized atoms. The diffracted intensity can be easily calculated for the Kekulé distortion as a function of ϵ. Figure 4.8(a) shows the diffraction pattern where the area of the circles correspond to the diffracted intensity. Because the unit cell was tripled, diffraction rods occur at $1/3$ multiples of the graphene reciprocal lattice vectors, $\mathbf{G}^(g)$.

Measuring the diffracted intensity of these third order spots revealed no measurable diffraction rod [see Fig. 4.8(b)]. Furthermore, it is not possible to argue that disorder is contributing to the null result as the buffer layer is highly ordered and diffraction of other surface rods were measured, i.e the incommensurate modulation rods. This indicates that if a Kekulé distortion is present, it is immeasurably small. Because only a small distortion is needed to open a substaintial band gap, it is a worthwhile exercise to determine the minimum detectable ϵ and whether that theoretical band gap is large enough provide an alternate explanation, in addition to incommensurate modulation, of the buffer band gap. This can be accomplished by comparing the ratio of integrated intensity expected for the $(01)_G$ and $(1/3, 1/3)_g$ rod [see Fig. 4.8(b) and (c)]. The calculated and experimentally determined ratio, $I(1/3, 1/3)_N = I(1/3, 1/3)/I(01)$, is shown in Figure 4.8(d). Since no peak was measured for $I(1/3, 1/3)$, the experimental noise is used as an upper limit for the integrated intensity. This results in $I(1/3, 1/3)_N \approx 1.62 \times 10^{-5}$ and a $\Delta a_{cc}^{(max)} < 0.005$ Å(Correspondingly, $\epsilon < 0.0025$ Å.). With these limits, a maximum band gap of $E_g^{(max)} < 0.19$ eV is determined. This analysis shows that SXRD could in principle measure a very small Kekulé distortion for the current sample order of the buffer layer. Also, these results show that the small distortion has a predicted band gap significantly less than the < 0.5 eV measured for the buffer layer [62]. Considering these results together suggests that Kekulé distortions alone cannot account for the observed band gap.

These results do not state that no strain is present in the buffer layer. Rather, they state

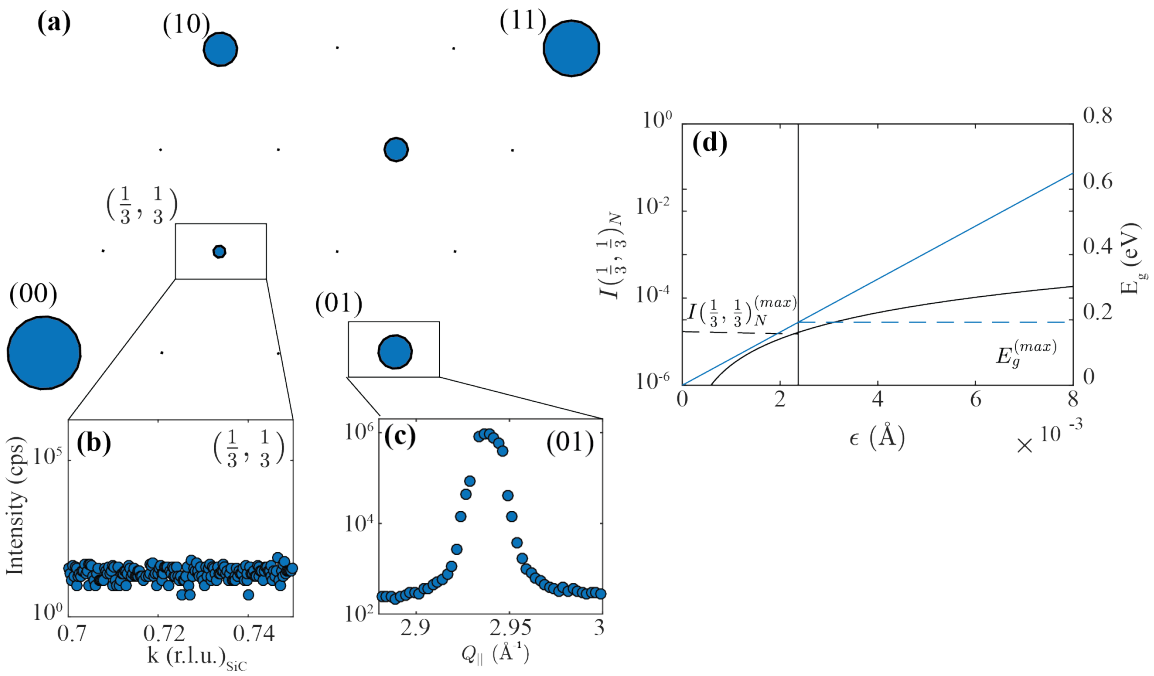

Figure 4.8: Diffraction based limitations on bandgap formation due to Kekulé distortions. (a) Diffraction pattern expected for a Kekulé distortion. The diffraction rods are labeled in terms graphene reciprocal lattice units. The Kekulé distortion requires a $(\sqrt{3} \times \sqrt{3})_g$ unit cell that causes diffraction at $\frac{1}{3}$ multiples of the $\mathbf{G}^(g)$. (b) Diffracted intensity measured at $(1/3, 1/3)_g$. There is no measurable diffraction rod associated with a Kekulé distortion. (c) Diffraction rod measured for $(01)_g$. Comparing $(01)_g$ diffracted intensity with the noise in $(1/3, 1/3)_g$. (d) compares the intensity ratio $I(1/3, 1/3)_N = I(1/3, 1/3)/I(01)$ to place an upper limit on the Kekulé distortion (black line). The diffraction limited maximum change in bond length (dashed black line) determines the maximum band gap $E_g^{(max)}$.

that there is minimal Kekulé contributions to the strain. Instead the primary strain observed is the IC modulation. However, it is was determined that the modulation was also quite small in the buffer layer, though not negligible. It is important to note that some finite contribution is observed as this is the whole premise of mutual modulation that provides precise predictions of the diffraction conditions. Furthermore, these distortions only characterized the in-plane modulations. In the following Chapter, I focus on the vertical corrugations present in the buffer layer and the SiC interface.

Since the local strain variation in the buffer layer is small, this indicates that the band gap is a result of some other interaction. From the SXRD analysis, it was found that the buffer and SiC interface interact in a strong and unique way described by mutual modulation. Mutual modulation requires the consideration of the interface. Through the model developed to describe the electronic structure resulting from mutual modulation, a graphene island formation was revealed that predicted large band gaps. Furthermore, the fact that the unbonded graphene "island" configuration was present for such a large range of $\eta^{(\mathrm{SiC})}$'s and that the opening of a band gap is prevalent over this same range lends a great deal of weight to the idea that the incommensurate system is responsible for the buffer's semiconducting properties. Coupling this to the fact that the calculated band structure, using the experimental value for q and $\eta^{(\mathrm{SiC})}$, reproduces the important features of the experimentally measured bands supports the importance of the modulated interface controlling the buffer's electronic properties.

CHAPTER 5

COMPOSITION AND STRUCTURE OF THE INCOMMENSURATE AND COMMENSURATE GRAPHENE-SIC PHASES

The discovery of incommensurate mutual modulation has provided a fundamentally new understanding of the mechanisms responsible for band gap formation in buffer graphene. Incommensurate crystals have important consequences for transport properties and also indicate the potential existence of other phases. It was long assumed that the buffer structure and properties were independent of layer coverage. However, the previous two chapters have demonstrated significant differences between a bare buffer layer (BG_o) and the buffer beneath monolayer graphene (BG_{ML}). The notable differences are: BG_o is incommensurate, has a band gap greater than 0.5 eV and has minimal random in-plane strain whereas BG_{ML} is commensurate with bulk SiC, nearly metallic and possesses a large random in-plane strain. A proper understanding of the differences and similarities between these buffer layers will provide insights into band gap formation along with new routes towards band gap engineering in graphene through substrate interaction.

In this chapter, the nature of the incommensurate and commensurate phases of buffer-SiC interaction is addressed through a combined study of X-ray Standing Wave X-ray Photoemission Spectroscopy (XSW) and X-ray reflectivity (XRR). Substantial differences in vertical corrugation and interface order are found. BG_o has a rich vertical structure spanning over 2 Å whereas BG_{ML} has a reduced vertical distribution of 0.4 Å well described by a normal distribution. The vertical corrugation in BG_o is consistent with the island formation predicted in Chapter 5 due to the incommensurate modulation in the SiC interface as the strong interaction with the interface at the island boundaries is expected to induce buckling in the graphene layer. In both BG_o and ML films, the SiC topmost interface layer is Si depleted indicating the presence of Si vacancies with possible C substitutions. These

vacancies/substitutions reduce the bonds to $<24\%$ of the BG_o and are responsible for the incommensuration. Although the interaction is reduced by Si depletion, the interaction is strong due to a bond distance of 1.87 Å. This distance is the same distance as the bilayer separation in bulk SiC(1.89 Å), suggesting sp^3 rather than Van der Waals bonding. When a monolayer forms, the average distance from the SiC interface layer contracts to be 2.22 Å in BG_{ML}. Although this distance is 0.3Å larger than the closest fitted distance found in the bare buffer layer, this does not imply a reduced interaction with the interface. Due to the corrugation in BG_{ML} and the topmost Si interface, roughly 30% of BG_{ML} is less than 1.89 Åfrom this interface indicating a similar, if not increased, interaction with the interface. A critical feature of the monolayer sample is an increase in the disorder and random strain in BG_{ML} and the interface layers. Since incommensurate systems necessarily require long range order, the increase in disorder causes interactions with bulk SiC and its periodicities to dominate. These results suggest that the increase in random strain can be considered as the mechanism driving the incommensurate-commensurate phase transition as well as the corresponding change in electronic structure.

5.1 X-ray Standing Wave Analysis of Graphene on SiC(0001)

Chapter 4 reported the observation of both an incommensurate and commensurate phase of the graphene interface with SiC(0001) in well ordered and homogeneous films of graphene with different layer coverages. The correspondingly distinct electronic properties mandates further detailed studies to gain a proper understanding of the mechanisms driving the incommensuration as well as the transition to a commensurate phase. Most of the structural studies have been on samples grown in ultrahigh vacuum where it is well known to have a large degree of graphene layer inhomogeneity, larger disorder, as well as a variety of interface structures compared to more recent techniques [63, 58, 43, 131, 52, 97]. Consequently, a clear picture of the buffer layer and its evolution with the formation of additional graphene layers is still lacking. This has resulted in theoretical studies of

simplified interface configurations and often reduced unit cells that hindered proper connections to experimental results [66, 69, 132, 67, 64, 68]. Now that improved growth methods are in place, reconciliation has begun where the observation of incommensurate mutual modulation in the buffer/SiC(0001) interface explained the semiconducting properties observed in ARPES. Furthermore, the change in electronic band structure resulting from incommensurate-commensurate phase transition inspires a method for band gap engineering in graphene through manipulation of the interface structure. This goal requires detailed studies to gain insight into the mechanisms driving the phase transition and how to manipulate the interface to achieve the desired electronic properties.

Below I discuss detailed structural studies conducted using mutual XSW and XRR analysis of BG_o and ML films grown by confinement controlled sublimation [37]. One of the most powerful techniques for measuring buried interface structures is synchrotron based surface x-ray diffraction and reflectivity. However, the phase problem is the principal challenge in achieving quantitative results. XSW measurements can address this by placing constraints on the amplitude and phase of the structure factor. This section presents the analysis and results from the XSW measurements. [63, 91, 133]

5.1.1 Experimental

In an XSW experiment, an incoming x-ray beam of energy $E = \hbar c k_o$ and a scattered beam with momentum, k_f, from a Bragg reflection ($G = k_f - k_o = 2\pi/d$) are used to produce standing waves whose crests are d apart. By choosing the SiC(0004) Bragg reflection for the 4H-SiC(0001) surface, the standing wave is perpendicular to the surface with $d = c_{\text{SiC}}/4 = 2.52$Å [Figure 2.9]. By changing E, the standing wave will move perpendicular to the surface. Since photoemission is proportional to the interference photon flux, the traversing standing wave will cause photoemission of different atomic species as the standing wave passes through the atomic planes. The normalized photoemission yield for a particular chemical species j in the material, $Y_j^{\mathbf{G}}(E)$, will therefore be function of

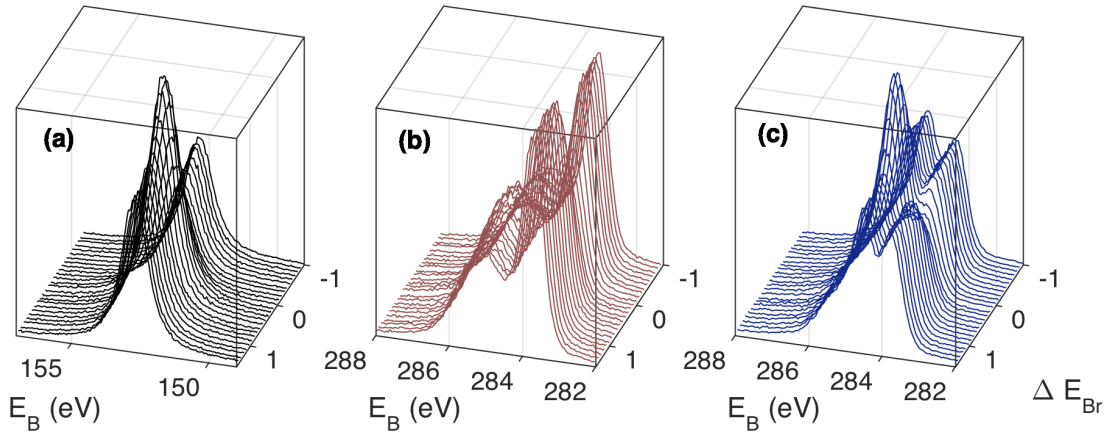

Figure 5.1: X-ray standing wave photoemission spectra as a function of ΔE_{Br} for Si 2s (a) and C 1s core levels for BG_o (b) and ML (c). As $h\nu$ passes through E_{Br}, ($\Delta E_{Br} = h\nu - E_{Br}$) a unique photoemission yield develops for each chemical component present. (c) clearly demonstrates the distinct yields that allow the graphene and bulk carbon to be distinguished.

E and can enable the extraction of information regarding the vertical distribution of that species. This basic phenomena is demonstrated in Figure 5.1 for the Si 2s of BG_o and C 1s spectra of BG_o and ML films. Figure 5.1 clearly demonstrates how different chemical species produce a unique photoemission yield. Furthermore, even if the chemical species are of the same element, the yield of each species can be extracted with a proper spectral decomposition. However, as I will show, a proper decomposition is not a trivial endeavor.

The XSW wave measurements were carried out at the GALAXIES beamline at SOLEIL Synchrotron [134]. To achieve the SiC(0004) Bragg reflection, $E = 2512$ eV was the incident x-ray photon energy and $\theta = 78°$. The energy resolution was better than 250 meV and the photoemission take off angle is perpendicular to the incident x-ray to ensure surface sensitivity. All measurements were conducted at room temperature. The substrates used for these studies were n-doped on axis CMP polished 4H-SiC(0001). Epitaxial graphene samples were grown by confinement controlled sublimation [37]. In this method, the SiC(0001) surface is heated in a nearly enclosed crucible to maintain a partial Si pressure during the growth procedure. Graphene growth depends on temperature, time and crucible geome-

try. In the current design, BG_o formed on the SiC(0001) surface in 30 minutes at 1400°C . When the SiC(0001) surface is heated to 1550°C for 20 minutes, a nearly complete second layer of graphene forms (referred to as ML). The ML film also has a buffer layer whose properties are distinct from BG_o and therefore will subsequently be distinguished as BG_{ML}.

Voigt functions were used for all buffer and bulk components of the C 1s and Si 2s spectra while the Doniach Sunjic lineshape was used for all graphene components. The Voigt function is a convolution of a Gaussian and Lorentzian lineshape,

$$V(x:I,F_G,F_L,x_o) = I\int_{-\infty}^{\infty}\frac{\sqrt{4\ln 2}}{F_G\sqrt{\pi}}e^{-4\ln 2\left(\frac{x'-x_o}{F_G}\right)^2}\times\frac{F_L}{\pi\left((x-x'-x_o)^2+F_L^2\right)}dx'. \tag{5.1}$$

Where F_G and F_L are the Full Width Half Maximums (FWHM) for Gaussian and Lorentzian distributions, x_o is the centered position and I is the integrated area of Voigt distribution. The overall FWHM of the Voigt distribution, F_V can be obtained by the approximation $F_V = 0.5346F_L + \sqrt{0.2166F_L^2 + F_G^2}$ to within 0.02%[135]. Each component is expected to have a unique F_G and F_L due to differences in vibrational degrees of freedom and excitation lifetimes. The Doniach Sunjic lineshape,

$$DJ(x:I,\alpha,F_{DJ},x_o) = I\,\frac{\cos\left(\pi\alpha/2+(1-\alpha)\tan^{-1}\left(-(x-x_o)/F_{DJ}\right)\right)}{\left((x-x_o)^2+F_{DJ}^2\right)^{(1-\alpha)/2}}, \tag{5.2}$$

has been traditionally used to fit the graphene C1s components, where α is the asymmetry parameter, and I, F_{DJ}, and x_o is a height parameter, width and center position, respectively [136]. To account for experimental broadening, thermal fluctuations, etc., the Doniach Sunjic lineshape is also convoluted with a normalized Gaussian in a similar manner to the Voigt lineshape. One difficulty with the Doniach Sunjic lineshape is that the integral does not converge for a nonzero asymmetry parameter. As a result an integrated area cannot be determined. However, for this lineshape, I is sufficient for extracting the XSW yield and a more precise quantification of the density and coverage will be obtained from X-ray reflectivity and discussed in Section 5.2.

5.1.2 X-ray Standing Wave C 1s Core Level Analysis

A proper analysis of $Y_j^{\mathbf{G}}(E)$ requires a proper spectral decomposition of the C 1s spectra. Figure 5.2 shows a typical C 1s spectra of BG_o at an E far from E_B. The spectra is fitted according the minimization procedure I will discuss below. For now, this spectra serves as reference to discuss previous analyses of the buffer C 1s spectra. C 1s analysis of graphene on SiC(0001) is complicated and requires at least 4 components that account for C-Si sp^3 bonds from bulk SiC (), C-C sp^2 in monolayer graphene (S_{ML}), and two buffer components, S_1 and S_2. They are identified in a similar manner as with Emery *et al.* and Emtsev *et al.*, which label the photoemission component of highest BE to as S_2. It is well known that the buffer layer strongly interacts with the SiC [36, 48, 66, 67]. Therefore, one component describes carbon bonded to interface silicon and the other component describes buffer carbon not bonded to the interface. Two components, as opposed to one, are necessary because the areal density of the buffer layer is larger than the interface Si areal density.

The binding energy and physical interpretation of these features has been debated. Emtsev *et al.* [36] attributed S_1 as buffer carbon sp^3 bonded to Si in the SiC interface from two observations. First, they noticed an approximate 2:1 intensity ratio of S_2:S_1. Given that the density of graphene is roughly three times larger than the Si density in SiC, the 2:1 ratio was consistent with ab initio bonding predictions from a reduced $(\sqrt{3} \times \sqrt{3})R30^\circ_{\text{SiC}}$ unit cell[65, 64], this painted the picture that every Si atom bonds to a C atom in the buffer layer. They also noticed a similar shift in binding energy of ~ 1 eV of the buffer σ-bands and the S_2 from the expected position of neutral graphite. This indicated that S_2 was more graphitic. Furthermore, they make note that bulk C-Si bonds in SiC are normally less than graphite, which justifies S_1 as the sp^3 component since it is at a lower BE than S_2.

More recent measurements by Emery *et al.* [63] provided a different interpretation that S_2, as opposed to S_1, was the bonded buffer component based off of their X-ray standing wave analysis. Analysis of their photoemission yield results suggested that S_2 was closer to the SiC interface. They also found an inverted S_2:S_1 ratio relative to Emtsev *et al.* They

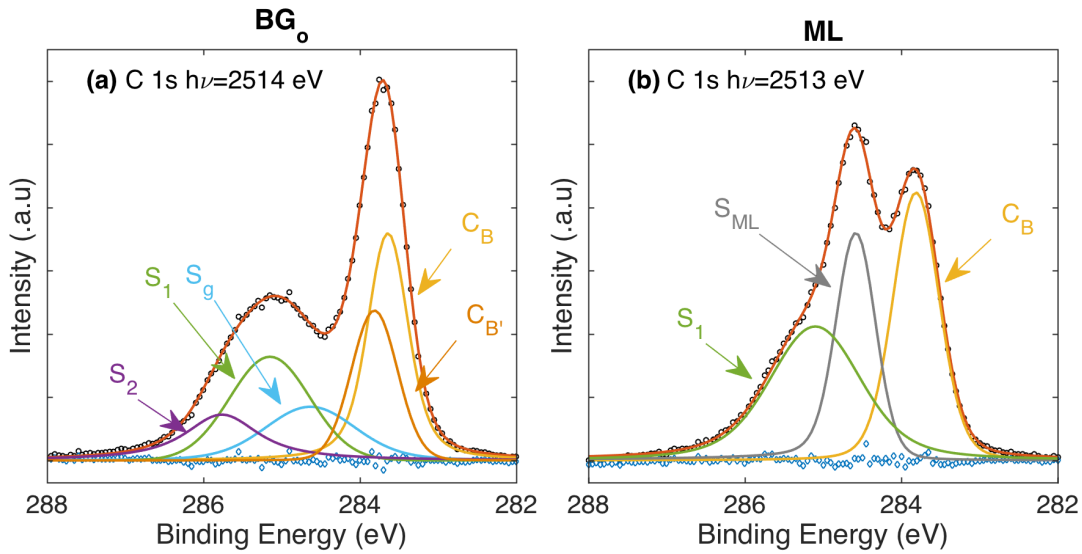

Figure 5.2: Typical C 1s spectra of a BG_o (a) and ML (b) surface. (a) The spectra is fitted with 5 components based on the χ^2_g minimization procedure described in the text. Typically 4 components are used to fit graphene surfaces on SiC(0001), two for the buffer layer (S_1 and S_2), one for graphene (S_{ML}) and one for bulk carbon from SiC (C_B). This spectra shows two additional features: S_g is another buffer carbon unbonded to the interface and $C_{B'}$ is another bulk carbon associated with the surface. (b) Contrary to BG_o, the ML spectra is well described by three components in the χ^2_g minimization: a buffer component (S_1), and monolayer component (S_{ML}), and a C_B.

justified their results by showing that the S_2:S_1 ratio of the buffer spectra in ref. [36] could also be inverted if a small component of graphene overgrowth was included: a likely scenario for UHV grown samples. They also note that other effects (e.g. spontaneous substrate polarization [88], band bending, charge-transfer doping and sp^2 and sp^3 bond hybridization) can influence the C 1s binding energy suggesting that the similar binding energy shift of $S_2$and the buffer σ-bands with respect to graphite was more or less a coincidence.

To date, no XSW or XRR measurements have been reported on a bare buffer layer. Previous studies only measured multilayer UHV grown samples where the lowest coverage sample studied was $\sim$0.5 ML. Consequently, the resulting C 1s spectra had a substantial monolayer graphene component that obscured the buffer components. This is demonstrated in Figure 5.2(b) for the ML sample analyzed in this thesis. Also, a 0.5 ML sample is neccessarily a mixture of bare buffer and buffer covered by a monolayer. This fact, which was unknown at the time of the previous XSW measurements, is critical as the SXRD analysis from Chapter 3 demonstrated structural and electronic differences between the two buffers. This type of sample hinders a proper discrimination between BG_o and BG_{ML} features. In addition to sample inhomogeneity, XSW analysis is complicated further by the fact that the S_{ML}BE is a function of the number of layers [36]. As the number of graphene layers increase, the binding energy approaches that of graphite. The consequence for XSW analysis is that two unique yields, i.e. a yield from monolayer and a yield from bilayer, will result at nearly the same binding energy and will therefore hinder a proper layer spacing from XSW analysis alone. This is not to say that SXRD reflectivity is without it's own set of challenges [see Section 5.2]. However, the benefits of each technique can be utilized to gain a better understanding.

In addition to these technical issues, the notion of a two component buffer is also suspect. This assignment arose from early theoretical calculations on an artificially reduced $(\sqrt{3} \times \sqrt{3})_{SiC}$ unit cell where only two types of carbon (carbon sp^3 bonded to Si and sp^2 carbon) were present in the buffer layer with a ratio of 1:3 [65, 64]. Similar ratios from

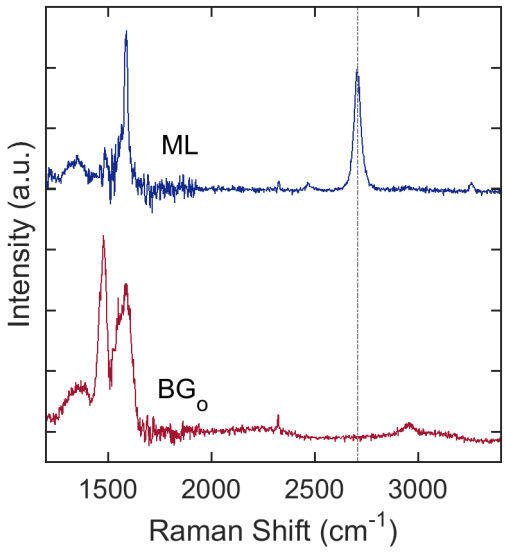

Figure 5.3: A comparison of the Raman spectra from a BG_o (blue) and a ML (red) film. The lack of a measurable 2D peak in the buffer only spectrum places a maximum coverage of 3% monolayer overgrowth in the buffer only film, consistent with previous ARPES estimates [62].

early C 1s spectra of the $6\sqrt{3}$ interface corroborated this idea[36]. However, given the incommensurate structure of BG_o, it is reasonable to expect a continuum, rather than two, of binding energies where any decomposition can only be an approximation. For this reason, the presented XSW analysis investigates the results from a multiple number of components.

With confinement controlled sublimation, layer control is improved and growth of a nearly complete buffer layer with minimal graphene overgrowth is possible. As a result, an upper limit of the graphene contributions to the C 1s spectra in CCS grown buffer samples can be obtained. Figure 5.3 demonstrates the difference in Raman spectra between BG_o and ML surfaces. The bulk SiC Raman signature was subtracted from each graphene spectra to reveal the surface components. The ML spectra is similar to previous reports for epitaxial graphene on SiC [41, 137]. The BG_o spectrum is characterized by broad D, G and D' peak features as well as a characteristic feature at 1490 cm^{-1} (B_o) and between 2900-3100 cm^{-1}. The presence of the D and D' features along with the absence of a 2D peak suggest a strong interaction with the interface.

The buffer spectrum is consistent with earlier measurements of the buffer layer [100, 138]. However, the buffer Raman spectra is different from reports for UHV and some argon grown samples [105, 101]. An important difference is the lack of a 2D peak, which can be used to estimated ML overgrowth. Using the ML 2D intensity as a reference and the background noise as an upper limit in the buffer 2D peak, an upper limit of 3% overgrowth is obtained across the entire sample. This is consistent with ARPES estimates of ML coverage in a similarly prepared BG_o film [62]. While Raman measurements place a limit on the graphene overgrowth, XPS analysis provides an initial estimate of a completely covered buffer surface [see Section 2.4]. Consideration of both XPS and Raman provide support that the SiC surface is fully covered by the buffer layer with minimal graphene overgrowth. Another important difference in the buffer Raman is the appearance of the B_o peak at 1490 cm^{-1} not observed in UHV samples. The peak was supported by vibrational density of states calculations on a reduced unit cell [100]. However, it's origin, especially in the context of an incommensurate buffer, is still largely unclear.

This assessment from Raman spectroscopy is essential for placing limits on the contribution expected for monolayer graphene and provides a means for detailed study of the BG_o components in the C 1s spectra. Determination of the proper number of BG_o components can be aided by XSW measurements. Based on the principle of the photoelectric effect, the binding energy of each chemical component is independent of E over the small ΔE range sampled in an XSW measurement. Therefore, deviations in the binding energy of chemical species as a function of photon energy suggest the presence of additional unaccounted chemical species. By considering the XSW C 1s spectra as a whole, the number of components, n_j, within statistical uncertainties, present in the buffer C 1s spectra can be identified.

Figure 5.4 demonstrates the procedure for identifying the appropriate n_j for the the C 1s BG_o and ML XSW spectra. Since the binding energy of each component should be independent of E, inaccuracies in n_j are highlighted by changes in binding energy as the

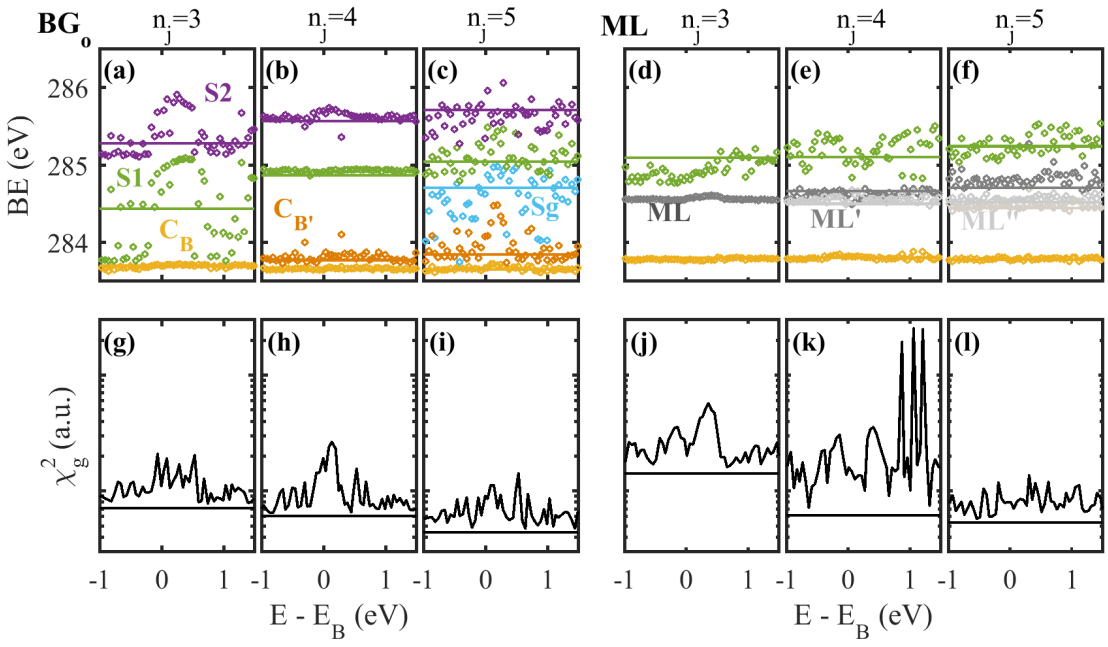

Figure 5.4: Binding energy dependence of the buffer layer component decomposition for the X-ray standing photoemission C 1s spectra of a $n_j = 3-5$ component buffer graphene (a-c) and monolayer (d-f) decomposition, respectively. The binding energy positions were determined through an unconstrained fit for the indicated E. Each color represents a unique component. (d-f) The different gray scales represent components associated with graphene. (g-i) and (j-l) show the χ^2_g resulting from binding energy and width determined from the unconstrained fit for the three to five component decomposition of buffer and monolayer graphene, respectively. The horizontal lines in (g-l) represent the minimized χ^2_g.

photon energy passes through the Bragg reflection. This is clearly demonstrated in Figure 5.4(a) when $n_j = 3$. When only the S_1, S_2 and $C_B$components are used to fit the BG_o C 1s spectra, there is a clear shift in binding energy of the S_1 and S_2 components. While the unconstrained fit adequately describes an individual spectra, it is clear that the traditional S_1 and S_2 components are insufficient for describing all the features present in the BG_o XSW C 1s spectra. As n_j increases, changes in binding energy are smaller relative to the statistical uncertainty indicating the approach to an appropriate number of components, but also the maximum n_j that can be resolved.

The maximum n_j occurs when there is substantial overlap in the uncertainty for binding energy of each component. For BG_o, Figure 5.4(c) demonstrates that $n_j = 5$ is the

maximum number of components that can be extracted from the XSW data. Analysis of the ML XSW data reveals the $n_j = 4$ as a maximum.

To fully account for the unique yields present in the XSW spectra, a unique two step fitting routine is developed. First, the integrated area for each component is determined for each E by minimizing the sum of the squares of the residuals, χ^2_E. During this first step, the binding energy and width are fixed for every E. Only the integrated area is allowed to vary. Then the binding energy and width are adjusted to minimize the global $\chi^2_g = \sum_E \chi^2_E$. Figure 5.4(g-l) demonstrates the large variability in χ^2_g that results from an unconstrained fit of an individual E. For a proper minimization of χ^2_g, an equal selection of the distinct spectra must be used, otherwise χ^2_g will be improperly weighted against certain features. For this reason, analysis is concentrated to E within -1.0 to 1.5 eV of the photon energy associated with the SiC(0004) Bragg reflection, E_B. The horizontal lines in Figure 5.4 represent the resulting binding energy (a-f) and χ^2_g (g-l) from the two step minimization procedure. Note that the binding energy positions are not the average binding energy positions for each component. In this way, minimizing χ^2_g leverages trends in the photoemission yield undetectable from typical core level spectra.

Figure 5.5 shows the best fits C 1s XSW spectra from the χ^2_g minimization for BG_o and ML. The spectra shown were collected at a photon energy of $E - E_B = 0.25$ eV. The quality of the fits is demonstrated by the residuals in Figure 5.5(d-f) and (j-l). Since E is near E_B in Figure 5.5, a large variation in the photoemission yield is present. This highlights the effects of incorporating additional spectral components. The BG_o is not well described by the traditional two components S_1 and S_2 for two primary reasons; (i) There is a large and well defined contrast in the residuals in Figure 5.5 and (ii) there are drastic changes in the peak positions and widths with the addition of more peaks.

The buffer components that change the most with the addition of more peaks are S_1, S_2, and S_g. A summary of the peak parameters and how they change with n_j for the these buffer components are shown in Table 5.1. A simple 2-component buffer fit gives broad

Table 5.1: Summary of the XSW C 1s spectrum Voigt peak positions, $\Delta E_j = E_j - E_{C_B}$ ($E_{C_B} = 283.70$ eV), Gaussian Width, FW_G, Lorentzian width, FW_L, and total width FW_V obtained from χ^2_g minimization for the n_j dependent components of BG_o. All values are in eV with an approximate systematic and statistical uncertainty of 0.1eV.

n_j	ΔE_{S_2}	FW_G	FW_L	FW_V	ΔE_{S_1}	FW_G	FW_L	FW_V	ΔE_{S_g}	FW_G	FW_L	FW_V
3	1.58	1.16	0.41	1.38	0.74	1.22	0.28	1.38	-	-	-	-
4	1.92	0.77	0.61	1.15	1.23	1.07	0.10	1.07	-	-	-	-
5	2.12	0.35	1.01	1.12	1.51	1.20	0.02	1.21	0.99	1.20	0.30	1.37

S_1 and S_2 features with $I_{S1} < I_{S2}$ similar to the 1:2 ratio reported in ref. [36]. Allowing a third component narrows both S_1 and S_2 and reverses their relative intensities such that $I_{S1} > I_{S2}$ contrary to Emtsev *et al.*, yet consistent with ref. [63]. Instead of identifying another buffer feature, the additional carbon feature identifies another bulk SiC component, $C_{B'}$. From the residuals in Figure 5.5(k), it can be seen that $C_{B'}$ reduces the residuals in the vicinity of E_{C_B}. With the addition of a fifth peak, the residuals is noticeably reduced [see Figure 5.5(l)] and manifests as an additional graphitic feature, S_g, with a binding energy of 0.99 eV, similar to ML (0.77 eV).

Since an upper limit of graphene overgrowth was determined to be less than 3%, S_g is not from graphene overgrowth as its relative fraction is 35% of all buffer components. Furthermore, the width of S_g is 1.43 eV [see Table 5.1], substantially larger than the ML width of 0.57 eV. However, the similarity in binding energy of S_g to ML is suggestive that it may be an additional graphene-like component present in BG_o. This result is confirmed in the following analysis of the photoemission yield. Furthermore, the graphene islands predicted from tight binding calculations of the incommensurate SiC interface in Section 4.2 accommodate the possibility of additional components. Three general types of C in BG_o can be identified from the bonding configuration shown in Figure 4.3: (i) C sp^3 bonded to the interface, (ii) unbonded $sp^3 - sp^2$ C at or near graphene island boundaries, and (iii) sp^2 bonded C in the graphene island.

In contrast to BG_o, the ML XSW C 1s spectra is relatively insensitive to the addition of spectral components. As n_j increases, the additional components merely attempt to account

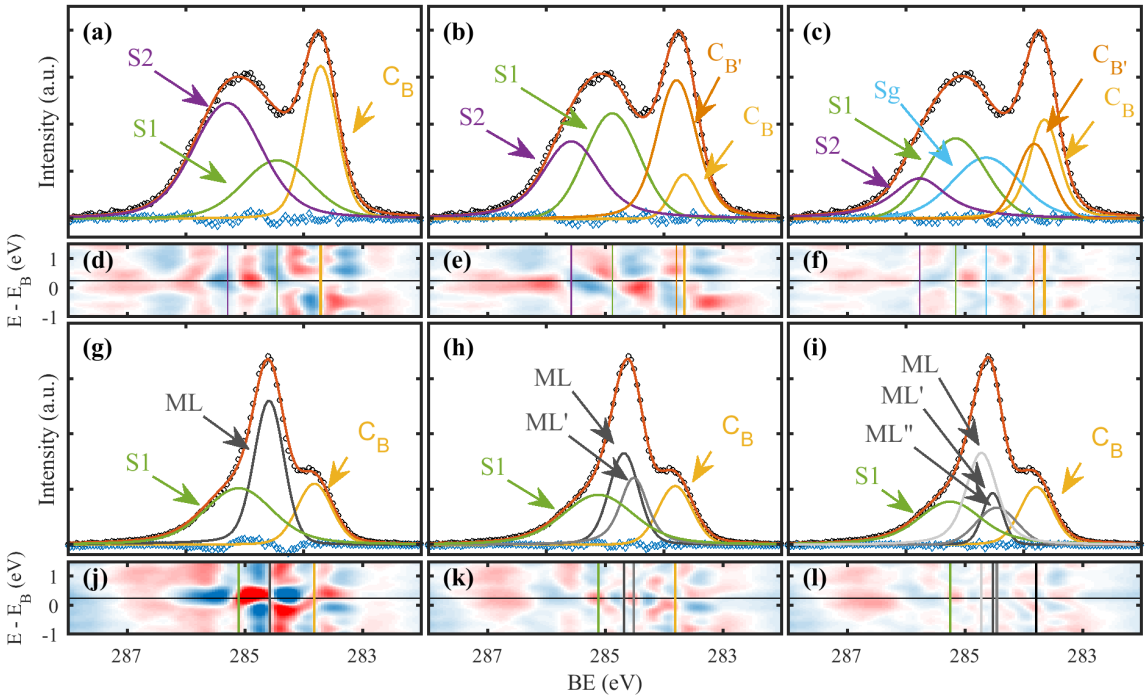

Figure 5.5: Component identification of X-ray standing photoemission C 1s spectra of buffer and monolayer graphene. (a-c) and (g-i) show the C 1s core level spectra taken at $E - E_B = 0.25$ eV for BG_o and ML, respectively. The C 1s spectra was decomposed into three to five components for buffer (a-c) and monolayer (g-i) graphene. The binding energy and width of each component component decomposition was determined using the two step regression procedure described in the main text to find the minimum χ^2_g for the collective C 1s spectra taken at each E. The residuals for E near E_B are shown in (d-f) and (j-l) for the three - five component decomposition from BG_o and ML, respectively. Each residual color map is on the same scale where red (blue) represents positive (negative) residuals with white being zero. Vertical lines represent binding energy of the components in C 1s spectra and the horizontal line represents the E of the spectra shown in (a-c) and (g-i).

Table 5.2: Summary of n_j independent parameters for BG_o and ML. These components showed little influence as a result of incorporating additional spectral features. The peaks are Voigt functions except Gaussian convoluted Doniach Sunjic lineshape for ML. All values are in eV, except for the asymmetry parameter α. E_j is the binding energy and ΔE_j is the binding energy offset from E_{C_B}. FW_G, FW_L, and FW_V are the Gaussian, Lorentzian and Voigt FWHM's. FW_{DJ} and FW_T are the Doniach Sunjic and convoluted FWHM's.

Bulk SiC									
	E_{C_B}	FW_G	FW_L	FW_V	E_{Si_B}	FW_G	FW_L	FW_V	
BG_o	283.65	0.48	0.24	0.62	152.79	0.67	1.18	1.50	
ML	283.78	0.59	0.12	0.66	152.86	0.72	0.78	1.22	
ML									
	ΔE_{S_2}	FW_G	FW_L	FW_V	ΔE_{ML}	FW_G	FW_{DJ}	FW_T	α
ML	1.35	1.04	0.55	1.37	0.77	0.55	0.3	0.57	0.03

for small variations in binding energy of the ML feature. Most notably, only a single BG_{ML} spectral component can be extracted. This may be a result of the strong ML signal obscuring BG_{ML} or there may be less vertical structure compare to BG_o. The largest reduction in χ_g^2 is obtained with addition of a forth component. The fourth component manifests as an additional graphene feature that may arise from bilayer graphene overgrowth. However, measuring the amount of bilayer overgrowth is better suited for x-ray reflectivity measurements since the difference in binding energy between the two monolayer components is only 0.17 eV. Although χ_g^2 decreased dramatically, the general structure of the components remained unchanged. The addition of a fifth component only provides a marginal improvement in χ_g^2 [see Figure 5.4], indicating that the best fit results from $n_j = 4$ for ML.

The results of the n_j independent parameters, such as ML and BG_{ML} are summarized in Table 5.2. For BL_{ML} and ML, the binding energy position was 1.35 eV and 0.77 eV and only varied by $\pm$0.1eV through the addition more peaks. The bulk C and Si components were also independent of the number peaks. The splitting of the ML peak is similar to the splitting of the C_B peak from the BG_o C 1s spectra. The $C_{B'}$ (ML') components only serves to refine the C_B (ML) peak, but due to their close proximity in BE, a reliable and unique photoemission yield for each component cannot be obtained. Instead the C_B and $C_{B'}$ (ML and ML') intensities are summed together to determine the photoemission yield presented

in Figure 5.6. Summation of two (or three when $n_j = 5$ for ML) yields is allowed as this is the same procedure taken to determine the yield from a Gaussian distribution [see Section 2.3]. The binding energy of both C_B and Si_B slightly increase in the ML film which may be related to charge transfer from the bulk to the graphene layers.[36]

Even with the obscuring monolayer, the differences in BG_o and BG_{ML} are quite noticeable. The spread in binding energy of the BG_o ($\approx$2 eV) is much larger than BG_{ML} (1.37 eV) and while BG_{ML} shows little variation with n_j, the BG_o components varied by more than 0.7 eV. The spread in binding energy of BG_o indicate a rich bonding structure that may be expected for an incommensurate system and its evolution with n_j suggests an approach to a better approximation of the buffer binding configuration.

These fits show that multilayer graphene samples complicate XSW analysis of the buffer and interface structure. The challenge of properly decomposing the C 1s spectra in the appropriate number of components will have an impact of the information obtained from an XSW Yield analysis. This means that the systematic errors present in XSW analysis prevent the use of the XSW derived parameters as fixed values within some statistical uncertainty. The true uncertainty of the XSW analysis cannot be obtained due to the presence of systematic errors. Instead, the XSW derived parameters have to be regarded as a starting point for atomic distributions that must be refined by x-ray reflectivity.

5.1.3 XSW Yield Analysis

The connection between x-ray standing waves and x-ray reflectivity is through the parameters derived from the normalized photoemission yield, $Y_j^{\mathbf{G}}(E)$. The photoemission normalized yield is obtained from the integrated intensity for each spectral component as a function of photon energy and is given by:[91]

$$Y_j^{\mathbf{G}} = 1 + R^{\mathbf{G}}(E) + 2P\sqrt{R^{\mathbf{G}}(E)} \int_{vol} \rho_j'(\mathbf{r}) \cos(\phi^{\mathbf{G}}(E) - \mathbf{G} \cdot \mathbf{r}) d\mathbf{r}. \qquad (5.3)$$

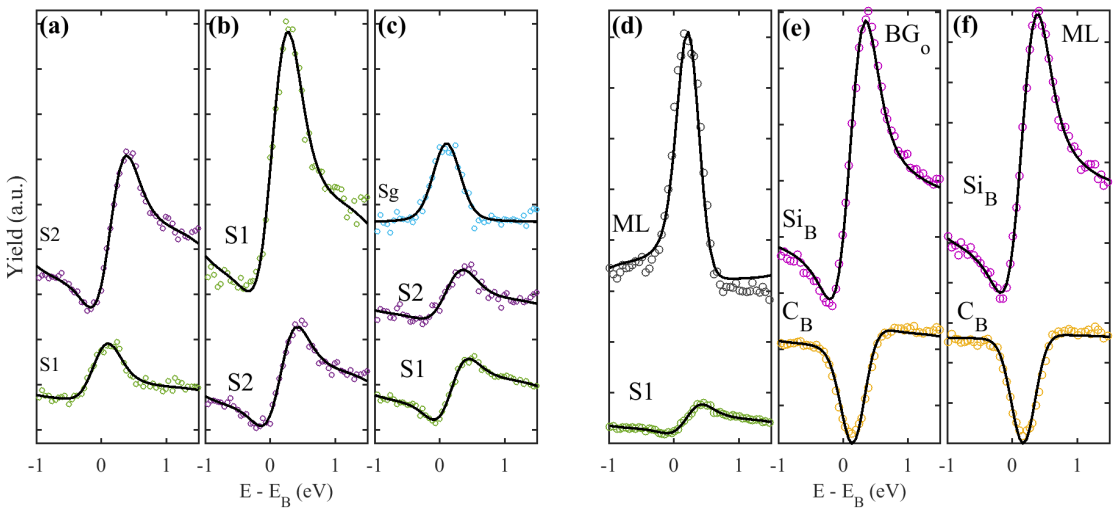

Figure 5.6: X-ray Standing Wave Yield for BG_o and ML. (a)-(c) Photoemission yields obtained for $n_j = 3-5$ of BG_o, respectively. The goodness of fit is insensitive to the choice of n_j. (d) Photoemission yield obtained for ML for all n_j. For ML, the photoemission yield was found to be insensitive to the choice of n_j. (e)-(f) Photoemission yield obtained for C_B (yellow) and Si_B (magenta) for BG_o and ML surfaces. The graphene components are indicated by their color: S_2 (purple), S_1 (green), S_g (blue) and ML (gray). The black lines are the best fit yield according to equation 5.1.3 for each component.

$R^{\mathbf{G}}(E)$ and $\phi^{\mathbf{G}}(E)$ are the energy dependent x-ray reflectivity and phase of the standing wave at the Bragg reflection $\mathbf{G}$. For this study, $\mathbf{G}$ is the SiC(0004) Bragg reflection. Both are calculated using dynamical diffraction theory from the bulk crystal structure [93, 94]. $\rho'_j(\mathbf{r})$ is the density distribution of the atomic species. The simplest density distribution to consider is a delta function. To account for thermal vibrations and static variations, the delta function is typically convoluted with a normalized Gaussian [133, 63, 132]. The parameterized yield is,

$$Y_j^{\mathbf{G}}(E) = 1 + R^{\mathbf{G}}(E) + 2P\sqrt{R^{\mathbf{G}}(E)} f_j \cos(\nu^{\mathbf{G}}(E) - 2\pi P_j^{\mathbf{G}}). \tag{5.4}$$

The reflectivity, $R^{\mathbf{G}}(E)$, and phase $\nu^{\mathbf{G}}(E)$, calculated from the bulk 4H-SiC structure factor using dynamical diffraction theory and broadened according to the instrument resolution [see. Section 2.3 and Figure 2.10]. $f_j = e^{-\sigma^2_{\mathbf{G},j} G^2/2}$ and $P_j^{\mathbf{G}} = \mathbf{G}\cdot\mathbf{r}_j/(2\pi)$ are known as the coherent fraction and the coherent position. These parameters correspond to the am-

plitude and phase of the $\mathbf{G}$ Fourier component. Extraction of f_j and P_j provide estimations of the vertical width and position of each chemical species. Since the SiC(0004) Bragg reflection was chosen, vertical density distribution information is acquired. In addition, the relative coverage the buffer components can be obtained. In order to fit $Y_j^{\mathbf{G}}(E)$ from the integrated intensities, an overall scale factor is required such that $I_j^{\mathbf{G}}(E) = N_j Y_j^{\mathbf{G}}(E)$. The scale factor can be a good measure of coverage as it describes the overall integrated intensity far from the Bragg reflection. This is because the reflectivity goes to zero away from E_B. As such, the fraction or coverage of a buffer layer component is $N_j / \sum N_j$ since S_1, S_2, and S_g are all from the same layer.

Figure 5.6 shows the fitted $I_j^{\mathbf{G}}(E)$ for BG_o and ML graphene and bulk components, respectively. All three scenarios of $n_j = 3-5$ for BG_o are shown in Figure 5.6(a) -(c). The yield parameters are summarized in Table 5.3. Clearly, an excellent fit is obtained for all components, regardless of the accuracy of the spectral decomposition. Consequently, this highlights the importance of obtaining a proper fit of the C 1s spectra prior to obtaining yield parameters.

One observation that is independent of the number of components used in the C 1s fits is that the buffer vertical distribution is large in BG_o and smaller in BG_{ML}. The BG_o width, including σ_j's, range from 1.3-1.7 Å, while BG_{ML} is 1 Å. Interestingly, the component closest to the interface flips from S_2 to S_1 when $n_j = 5$. For this reason, S_1 is now identified as the bonded buffer component, not S_2, favoring the interpretation of Emtsev *et al.* that the buffer component bonded to the interface is at a lower BE. [36] Furthermore, the yield parameters from S_g further support its graphene-like character. S_g is found to be farther from the interface than either S_1 or S_2. It should be noted that the coherent position for S_g and ML are similar. However, other Raman in Figure 5.3 excluded this interpretation. Reflectivity results also exclude monolayer overgrowth and will be discussed below. Furthermore, the S_{ML} coherent position considers contributions from both monolayer and bilayer components, which will consequently provide an inaccurate layer spacing prediction and the

Table 5.3: Summary of XSW results for the graphene components in BG_o and ML. The results for $n_j = 3-5$ for BG_o are shown. The paramters P_j and f_j and the corresponding d_j and σ_j are obtained from equation 5.1.3. For clarity, the distance from the topmost Si layer is reported by subtracting the atomic plane position for the topmost Si place, $d_{Si} = 0.09$ Å, from d_j. Θ_j is the fraction fraction of each component to all buffer components.

j		P_j	$z_j - z_{Si}$ (Å)	f_j	σ_j (Å)	Θ (%)
BG_o ($n_j = 3$)	S_2	-0.02(2)	2.37(4)	0.52(4)	0.46(2)	70(1)
	S_1	0.23(5)	3.01(1)	0.3(1)	0.6(1)	30(1)
BG_o ($n_j = 4$)	S_2	-0.04(2)	2.33(4)	0.56(5)	0.43(3)	24(1)
	S_1	0.07(3)	2.61(7)	0.36(4)	0.58(3)	76(2)
BG_o ($n_j = 5$)	S_2	0.03(5)	**2.5(1)**	0.48(9)	0.48(7)	32(1)
	S_1	-0.07(1)	**2.26(3)**	0.67(5)	0.36(4)	33(1)
	S_g	0.28(2)	3.13(6)	0.7(2)	0.3(1)	36(2)
BG_{ML}		-0.06(2)	2.30(5)	0.41(2)	0.52(3)	-
ML		0.27(2)	5.63(5)	1.0(1)	0.0(1)	-
C_B	BG_o	-0.24(1)	-0.69(2)	0.79(5)	0.27(4)	-
	ML	-0.25(1)	-0.72(2)	0.72(3)	0.33(2)	-
Si_B	BG_o	0.04(1)	0.00(2)	1.00(3)	0.05(4)	-
	ML	0.04(1)	0.00(2)	0.99(3)	0.07(4)	-

similarity between $P^{\mathbf{G}}_{S_g}$ and $P^{\mathbf{G}}_{S_{ML}}$ should not be considered compelling evidence that they are from a similar source. As a result, the identification of S_1 as the closest component becomes even more peculiar because it indicates that the binding energy does not linearly evolve from a sp^3 to sp^2 bonding configuration. These results provide validity and consistency between the seemingly contradictory reports of Emery *et al.* [63] and Emtsev *et al.* [36]. That is, both hybridization and charge transfer are influencing the binding energy of the buffer components.

Another notable feature is that $z_{S_1} \approx 2.3$ Å is farther from the Si and broader than previous reports of 2.1 Å.[63] Because of the larger separation and width, $z_{S_1} - z_{Si}$ cannot be regarded as a bond distance or a component exclusively associated with an sp^3 bond. However, it can be seen that regardless of the n_j used in the spectral decomposition, $z_j - \sigma_j$ for the closest component is consistently 1.9 Å from the topmost interface Si. This result is consistent with recent cross-sectional TEM measurements of the bare buffer surface [116]. While the lower portion of the S_1 distribution distance to the interface is consistent with

sp^3 bond lengths, the upper half is mostly larger than any expected bond length, even when considering the relatively sharp $\sigma_{Si_B} = 0.05$. This would suggest that a significant fraction S_1 is not bonded to Si. In this sense, $\Theta_{S_1}(n_j = 5)$ imposes an upper limit on the number of buffer bonds to the Si interface, rather than an approximate number of interface bonds.

The similarity in width and position of the BG_o indicate some consistency across the different density distributions obtained from the different spectral decompositions. The addition of more spectral components act to refine the distribution. Figure 3.3 demonstrates how the structure of the BG_o density distribution is enhanced by fitting with an increased number spectral components. When $n_j = 3$ the density in nearly unphysical as the large σ_{S_1} and σ_{S_2} places significant density less than 1.9 Å, the approximate Si-C bond length in bulk SiC. As n_j increases, the σ_j's decrease and the density below 1.9 Å decreases. Furthermore the decrease in σ_j's enable the discernment of more structure. Nevertheless, the corrugation remains large but the appearance of multiple features arise and bears some resemblance to TEM measurements.[116]

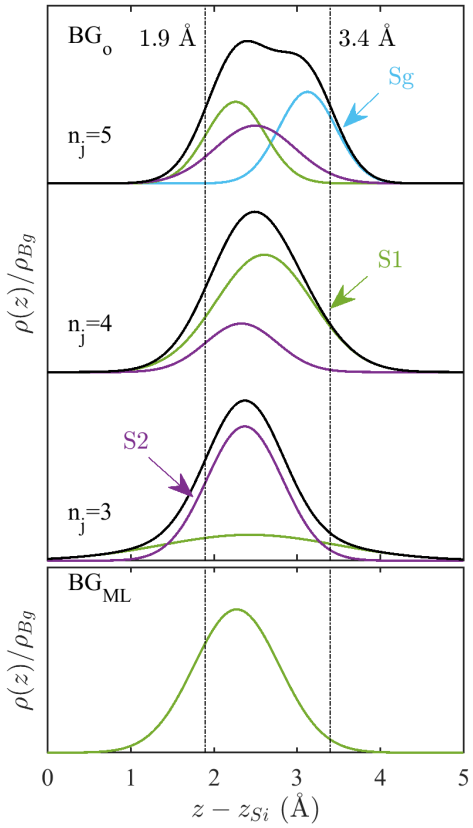

Figure 5.7: XSW derived density distributions of BG_o resulting from the yield obtained from a $n_j = 3 - 5$ spectral component decomposition of the XSW C 1s spectra. As n_j increases, the distribution becomes more refined. However, XSW analysis is statistically limited to $n_j = 5$ [see Figure 5.4]. A similar color scheme is used for the buffer components S_1 (green), S_2 (purple), and S_g (light blue). The intergrated area is proportional to the Θ_j's in Table 5.3. The black curve represents the superposition of all buffer components to give the total buffer density distribution.

5.2 X-ray Reflectivity of the Buffer Layer and Monolayer Graphene on SiC(0001)

While advancements were made in the general properties of the BG_o distribution through XSW analysis, there is some concern as to whether the XSW results is providing a true representation of the buffer density due to the challenges associated with a proper spectral decomposition of the C 1s spectra. For instance, the large width of the density distribution is cause for some concern as it is substantially larger than recent measurements [116]. However, the history of both measured and calculated corrugations spans a wide range from as small as 0.5 Å as large as 4 Å [116, 66, 67, 52, 53, 43], indicating the XSW results may not be unreasonable. Additionally, determination of the SiC interface densities is challenging with XSW since there will be photoemission contributions from equivalent atomic planes from the bulk SiC. The findings from XSW analysis can be refined with x-ray reflectivity analysis as x-ray reflectivity is the best tool for studying the structure and density of buried interfaces.

5.2.1 X-ray Reflectivity Methods

The x-ray scattering experiments were performed at the SOLEIL Synchrotron on the SixS beamline in UHV. The photon energy used in these studies was 12.8 keV for a wavelength of 0.9687Å. The vertical beam width was measured to be 74 μm with an energy resolution of 1 eV. For these experiments, momentum transfer of the incident and reflected beam is defined in terms of hexagonal SiC reciprocal lattice vectors, i.e, $\mathbf{Q} = \mathbf{k}_f - \mathbf{k}_i = h\mathbf{a}^*_{\text{SiC}} + k\mathbf{b}^*_{\text{SiC}} + l\mathbf{c}^*_{\text{SiC}}$, where $a^*_{\text{SiC}} = b^*_{\text{SiC}} = 2\pi/(a_{\text{SiC}}\sqrt{3}/2)$ and $c^*_{\text{SiC}} = 2\pi/c_{\text{SiC}}$ with $a_{\text{SiC}} = 3.08$ Åand $c_{\text{SiC}} = 10.0805$ Åbeing the typical lattice parameters for 4H-SiC. The reciprocal lattice units $(r.l.u.)$ (h, k, l) define a unique momentum transfer. Since these studies are of the on axis SiC(0001) surface, h and k describe momentum transfer parallel to the surface, while l describes momentum transfer perpendicular to the surface. In the reflectivity geometry, there is only perpendicular momentum transfer, i.e. $\mathbf{Q} = \mathbf{Q}_z = l\mathbf{c}^*_{\text{SiC}}$.

Since x-ray reflectivity only depends on l, data can be analyzed by a one-dimensional model that describes the averaged lateral information over the illuminated area.

Reflectivity measurements were collected in a continuous 2θ scan. Initially, rocking scans were collected at selected l throughout the range of interest. Based off these measurements, the horizontal detector slits were set to capture the fully integrated x-ray intensity. Analysis of the reflectivity data was restricted to $l > 0.6$ since the width and shape of the scattered intensity increases due to critical angle effects (e.g. Yoneda wings) at low l [139]. Furthermore, reflectivity at low Q_z is typically used to characterize surface roughness, whereas pertinent information of the interface structure is captured at larger Q_z. It is well known that SiC exhibits quasi-forbidden reflections due to slight deviations from the ideal crystal structure [80]. The quasi-forbidden reflections, along with the bulk SiC reflections at $l = 4$ and $l = 8$ do not primarily describe surface details and for this reason, they are excluded in the model fitting procedure.

5.2.2 Graphene and SiC Interface Reflectivity Model

The model used for analysis is similar to previous studies [63, 59]. A schematic of the model is shown in Figure 5.2.2. Contributions to the x-ray reflectivity comes from three sources: relaxed and/or reconstructed SiC bilayers, buffer graphene and additional graphene layers. The scattered x-ray intensity can then be written as,

$$I_l^{obs} = C(\theta, l) e^{-4\gamma_{\text{SiC}} \sin^2(\pi l/2)} \left| \frac{F_{\text{Bulk}}(l)}{1 - e^{-2\pi i l}} + F_I(l) + \frac{\rho_G}{\rho_{\text{SiC}}} \left(F_{Bg}(l) + F_G(l) \right) \right|^2 . \qquad (5.5)$$

$C(\theta, l)$ contains all the constants and geometrical corrections from the experimental configuration [75, 74]. The corrections relevant for x-ray reflectivity are the illuminated area ($\propto \min(L, d_{h\nu}/\sin\theta)$), Lorentz factor ($\propto 1/\sin\theta$), polarization ($\propto \cos^2(2\theta)$) and rod interception. γ_{SiC} describes half-cell steps on the surface.[59] F_{Bulk} is the structure factor for 4H-SiC.[80] The term $1/(1 - e^{-2\pi i l})$ accounts for surface truncation [140]. The interface

term of the structure factor consists of 4 SiC bilayers,

$$F_I = \sum_{\alpha=\{Si,C\}} \sum_{j=1}^{4} f_\alpha(l)\rho_{\alpha,j} e^{-2\left(\frac{\pi l}{c_{\text{SiC}}}\right)^2 \sigma_{\alpha,j}^2} e^{-i2\pi l z_{\alpha,j}/c_{\text{SiC}}}. \tag{5.6}$$

$f_\alpha(l)$ is the atomic form factor for $\alpha =$ C or Si. The atomic form factor was approximated using a standard exponential parameterization [71]. Each atomic species in the interface SiC bilayers are described by three parameters: a vertical position, $z_{\alpha,j}$, an areal density, $\rho_{\alpha,j}$, and a Gaussian broadening, $\sigma_{\alpha,j}$. When $\rho_{\alpha,j} = 1$, this corresponds to the bulk SiC density, 1.22×10^{15} atoms cm^{-2}. A normalized Gaussian is convoluted with each component to account for both vertical disorder and corrugation with a standard deviation of $\sigma_{\alpha,j}$. This captures information regarding vertical disorder in the topmost interface layers that may arise from the Si sublimation graphene growth process as well as vertical corrugation in the buffer and additional graphene layers. These parameters are relaxed in order to account for surface reconstructions. The connection of $z_{\alpha,j}$ and $\sigma_{\alpha,j}$ to the interface XSW parameters is challenging since each component is approximately at the same position with respect to the standing wave field. These parameters are treated with more flexibility since the Si_B and $\text{C}_\text{B}$yield parameters are an attenuated superposition from multiple layers.

To simplify coverage estimates, the structure factor of the graphene layers, including the buffer layer, are weighted by the density areal densities, $\rho_{G_i}/\rho_{\text{SiC}}$. Since there will be slight differences in the graphene areal density, ρ_{G_i} represents areal density for the respective graphene forms. The buffer layer structure factor is treated differently than the other graphene layers. From the XSW standing analysis, it is clear that multiple components are present in BG_o. For consistency with XSW analysis, 2 and 3-component buffer vertical distribution were considered. To account for this, the buffer layer structure factor is expanded by $n_{Bg} = 2 - 3$ Gaussian broadened components,

$$F_{Bg} = f_C(l) P_{Bg} \sum_{j}^{n_{Bg}} \Theta_j e^{-2\left(\frac{\pi l}{c_{\text{SiC}}}\right)^2 \sigma_j^2} e^{-i2\pi l z_j/c_{\text{SiC}}}. \tag{5.7}$$

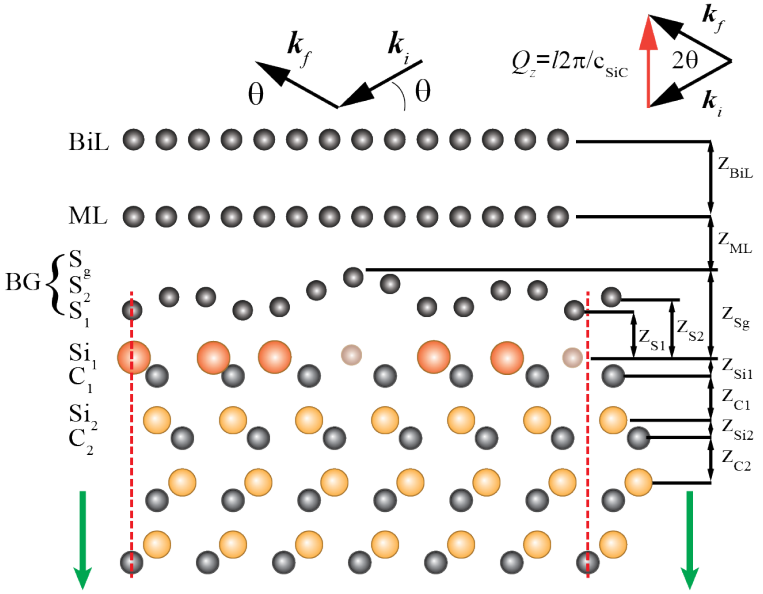

Figure 5.8: Schematic of the model used for SXRD reflectivity analysis. Reflectivity is described by a one dimensional model. For analysis, four interface SiC layers, a three component buffer (the naming convention is consistent with XSW analysis), and up to two graphene layers were considered. The topmost Si and C interface is considered the first SiC bilayer, with the layer number increasing into the bulk. All of the vertical distributions for a given layer are approximated by a guassian distribution described by a width, σ, centered at a position, z, with a density, ρ or coverage Θ. If ρ for the layer is known, then a coverage estimate is obtained. For example, a coverage estimate is obtained for the graphene layers because the in-plane density is known from previous measurements of the lattice parameter [see Chapter 3]. However, the presence of Si vacancies or C substitutions in the SiC interface layers will reduce the average density of the layer.

Here, P_{Bg} represents the coverage of the buffer layer. The vertical distribution can be approximated and modeled by the position (z_j), width (σ_j), and relative fraction (Θ_j, where $\sum_j^{n_{Bg}} \Theta_j = 1$) of the n_{Bg} components. By separating the overall coverage, P_{Bg}, and the relative fraction, Θ_j, the coverage can be determined while constraining Θ_j. In this way, Θ_j is analogous to the values reported in Table 5.3.

The XSW results showed that the graphene components of the ML film were well described by a single component and contained a small fraction of bilayer overgrowth. For this reason, the structure factor for the graphene layers is only described by a single component. Therefore, the structure factor for all graphene layers above the buffer are described in a similar way as the SiC interface bilayers,

$$F_G = f_C(l) \sum_m^M P_m e^{-2\left(\frac{\pi l}{c_{\text{SiC}}}\right)^2 \sigma_m^2} e^{-i2\pi l z_m / c_{\text{SiC}}}. \tag{5.8}$$

M is the total number of graphene layers, P_m, σ_m, and z_m represents the coverage, width and position of each graphene layer. Since there was only a small amount of bilayer graphene present on the ML film, it was unnecessary to assume a constant graphene layer spacing between multiple layers.

5.2.3 Lasso Regression for X-ray Reflectivity

While x-ray reflectivity is a powerful tool for studying the structure of buried interfaces, the phase problem along with intensity data extending many orders of magnitude present challenges with determining the uniqueness of the model used to describe the system. Furthermore, many models require many fitting parameters. For example, the model presented here consists of 55 parameters when including an overall scale factor, bulk lattice parameter, overall Debye-Waller factor, correlation length and adatom species. Generally it is not possible to allow parameters to freely vary and arrive at a physical result. Often, only a few parameters are allowed to vary a time. This challenge involves determination of the relevant

parameters and the correspondence of the model to the physical reality. To address these challenges, a lasso fitting routine is introduced, which stands for least absolute shrinkage and selection operator [141]. Usually, in ordinary least squares regression (OLS), the function minimized, χ^2, is just the sum of the squares of the residuals. To account for the many orders of magnitude, it is typical to weight the residuals by the experimental uncertainty, $\sigma_l = \sqrt{I_l^{obs}}$ [70]. Lasso regression introduces a penalty parameter, Λ, when a parameter deviates from a specified nominal value. χ^2 now has the form,

$$\chi^2 = \frac{1}{N-P}\sum_i^N \left(\frac{I_l^{calc} - I_l^{obs}}{\sqrt{I_l^{obs}}}\right)^2 + \Lambda \sum_j^P |\beta_j - \beta_{j,o}|, \tag{5.9}$$

where N is the number of data points, I_l^{obs} is the measured intensity for a given l, P is the number of parameters, β_j is the optimized parameter and $\beta_{j,o}$ is the default parameter value. Note the parameters β_j correspond to normalized versions of position, width and coverage/density, so that changes in parameters result is similar changes in χ^2.

This regression method allows for a controlled approach to the appropriate model and serves to identify the relevant parameters. For instance, χ^2 is only ever reduced if the increase from the lasso term is smaller than the decrease from the OLS term. This helps to identify the parameters, or combinations thereof, that have the greatest effect on the reflectivity. It can be seen that the choice of Λ is important. If Λ is too large, no parameters will be adjusted. On the other hand, as $\Lambda \to 0$ the regression approaches the OLS minimization procedure and all the aforementioned difficulties.

Because of the ambiguity in choice of Λ, it is still ideal to achieve a minimum in the OLS term. To this end, the regression process starts with the choice of a suitably high Λ. When Λ is high, this selects the parameters that provide the largest reduction in the OLS term. Gradually, Λ is reduced and the default parameters are updated until the model has converged to the minimized result. This enables a seamless connection with the XSW derived parameters and places XSW and reflectivity on an equal footing. The XSW pa-

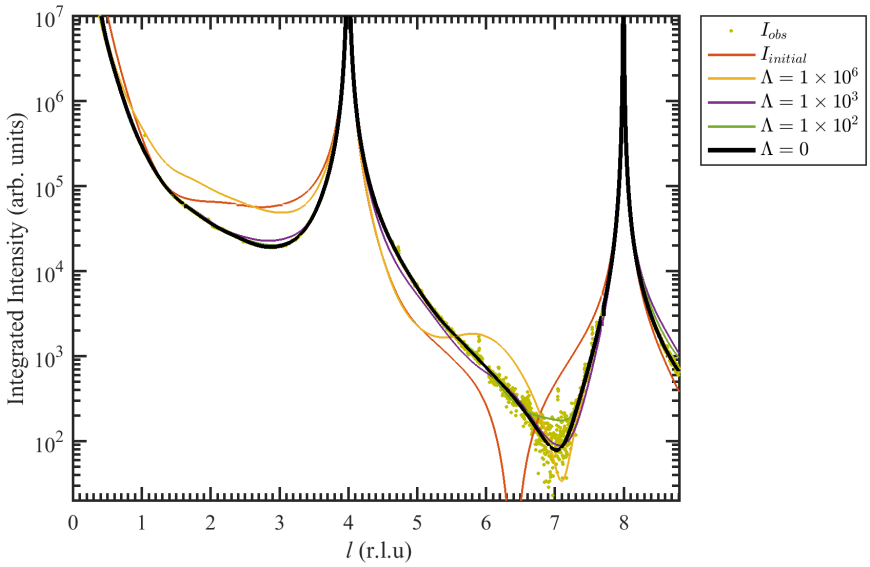

Figure 5.9: Demonstration of the lasso fitting method for BG_o. The initial parameters were from the XSW results for a 3-component buffer and a bulk terminated SiC interface. At first, a large Λ along with a XSW constrained buffer is used. This captures the essential parameters the reduce χ^2. As $\beta_{j,o}$ is updated and Λ is reduced, eventually a completely unconstrained OLS ($\Lambda = 0$) regression is possible.

rameters for S_1 , S_2 , and S_g become the $\beta_{j,o}$ for BG_o and the bulk positions, widths and densities are used as the default values for the SiC interface layers.

Figure 5.9 demonstrates the approach to an optimized fit of the reflectivity data using lasso regression. At first, the parameters for the buffer are constrained, within statistical uncertainty, to the XSW values. The reflectivity of the initial parameters shows little resemblance to measured reflectivity for BG_o. When Λ is high, the fit improves, but still does not accurately describe the reflectivity. As the process of updating $\beta_{j,o}$ and reducing Λ continues, an improved fit is obtained. Eventually, $\beta_{j,o}$ has sufficiently converged that a completely unconstrained fit is possible and provides an excellent fit to the measured reflectivity.

5.2.4 Results and Discussion

The reflectivity and the best fit model is shown in Figure 5.10 for BG_o (a) and ML (b) films. To get a sense of the absolute scale, the reflectivity for bulk terminated SiC is shown. By comparing the deviation in intensity from bulk SiC, it is clear that the changes in reflectivity are small for BG_o, only about a factor of 4-10 [Figure 5.10(a)]. This is a direct consequence of a large vertical "thickness" in the buffer. To understand this, consider that the contribution of σ to the structure factor has the form $e^{-1/2(Q_z\sigma)^2}$. As σ increases, it's contribution to the reflectivity decreases at larger Q_z. Therefore, just by observing the similarity of the BG_o and bulk SiC reflectivity, it can be expected that the vertical distribution is large. From a practical standpoint, the relatively weak signal makes obtaining a reliable fit challenging. Thus, the results from XSW analysis provide critical information for an initial configuration and the issue of a small reflectivity signal can be addressed. In contrast to BG_o, the reflectivity for ML in Figure 5.10(b) clearly has more structure beyond the contribution of bulk SiC. This indicates the presence of more features at well defined vertical distances, as would be expected for multiple graphene layers. One consequence of this difference in vertical distribution between the two surfaces is that even a small partial coverage of monolayer graphene will significantly reduce the sensitivity to the buffer structure. This is the case for previous reflectivity studies and the motivation for the presented work [63, 59].

Table 5.4 summarizes the best fit parameters used to produce the vertical density distribution shown in Figures 5.11 and 5.12 for the 3-component BG_o (a) and ML (b). Both 2 and 3-component buffer distributions were tested. However, the 3-component always provided a better fit ($\chi^2 = 39$ compared to $\chi^2 = 513$ for $n_{Bg} = 2$). The results provide quite a few enlightening observations. First, it shows that S_1 in BG_o is very close to the last Si layer (1.87 ± 0.09 Å), which is close to the bulk Si-C bond of 1.89 Å and very similar to the findings of previous STEM work (1.9 Å).[116] The width of S_1 is also sharp, just like the width of the topmost Si layer. Considered together, the close and well defined distance between the S_1 and Si_1 components suggests the presence of a strong covalent bond. The

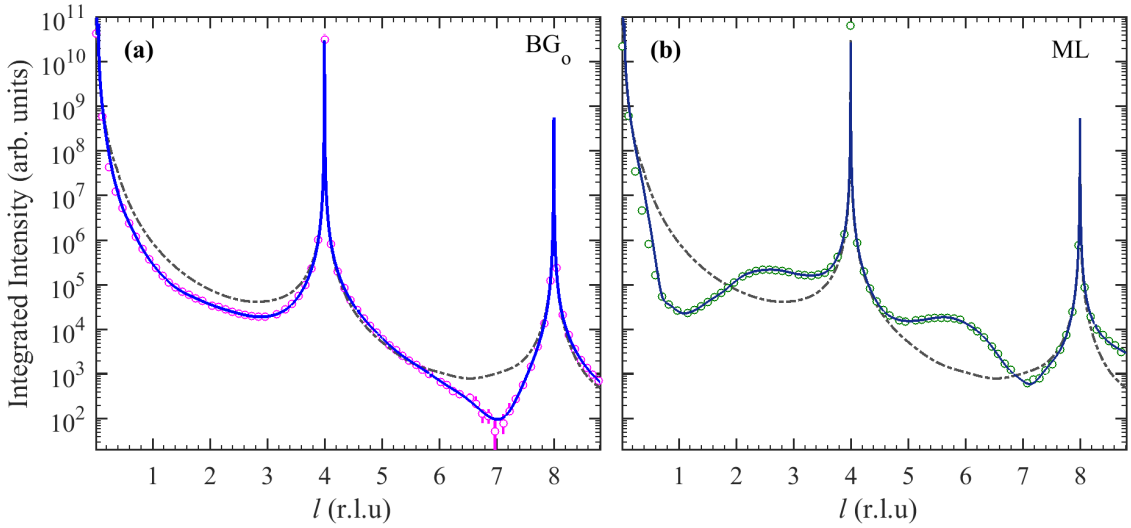

Figure 5.10: X-ray reflectivity of (a) BG_o and (b) ML films. The measured reflectivity is shown as open circles. The error in the measured reflectivity is less than the size of the open circles except near $l = 7$ r.l.u. for BG_o and is shown by vertical lines. The calculated reflectivity BG_o uses a 3-component buffer structure with a small ML coverage and surface surface contamination. For ML, the monolayer and bilayer components are allowed to vary up complete coverage. The reflectivity from a bulk terminated SiC surface (dashed lines) is shown for comparison of intensities above background.

Table 5.4: SXRD reflectivity bet fit parameters. The for definition of separation distances, z, see Figure 5.2.2, the parameters σ, ρ and Θ are defined from the structure factors in equation 5.2.2, and correspond to a vertical width/thickness, density and coverage. When the density is known for a layer, such as graphene, a coverage estimate is obtained, otherwise a layer density is provide. Interface densities are reported as a fraction of their bulk value. Coverages are reported as a fraction of the surface. The coverage for BG_o was 0.98.

Film	j	z (Å)	σ (Å)	ρ or Θ
BG_o	S_1	1.87(0.09)	0.15(0.11)	0.26(0.06)
	S_2	2.71(0.07)	0.27(0.21)	0.47(0.06)
	S_g	3.80(0.10)	0.28(0.10)	0.26(0.04)
	Si_1	0.47(0.02)	0.10(0.05)	0.75(0.10)
	C_1	1.98(0.05)	0.05(0.05)	0.92(0.23)
	Si_2	0.66(0.01)	0.05(0.02)	0.96(0.01)
	C_2	1.86(0.01)	0.05(0.05)	0.93(0.02)
ML	S_1	2.22(0.07)	0.20(0.12)	0.88(0.15)
	ML	3.46(0.03)	0.05(0.08)	0.69(0.01)
	BiL	3.21(0.04)	0.05(0.10)	0.27(0.01)
	Si_1	0.46(0.05)	0.20(0.05)	0.79(0.05)
	C_1	2.08(0.05)	0.24(0.05)	0.80(0.10)
	Si_2	0.68(0.01)	0.15(0.01)	1.00(0.01)
	C_2	1.81(0.02)	0.22(0.01)	0.99(0.03)

XSW results were less suggestive. In the XSW analysis, the S_1 distance was farther (2.26 Å) and broader (0.36 Å) indicating that the multiple components could not be perfectly decomposed.

Compared to the XSW analysis, the decomposition from reflectivity finds that the S_1 fraction is reduced from 33% to $26 \pm 6\%$. This indicates that although the interaction is strong, the amount of bonding is reduced from the XSW result. It should also be emphasized that vertical distance is not a direct correspondance to an sp^3 bond. Rather, 26%, just as S_1 in XSW, still serves as an upper limit to the amount of bonds to the buffer. The STEM results showed that there was a vertical periodic structure in both the buffer layer and the interface [116]. Because of this, σ for the interface and buffer components are an approximation of this corrugation, not a simple estimate of disorder. As a result, a bond will only occur when the corrugation in the interface and buffer produce a *total* distance, not just vertical distance, below some threshold. In fact, the incommensurate tight

binding model demonstrated that the planar distance was the critical factor for bond prediction [see Figure 4.2] and led to a significant reduction in bonding compared to previous commensurate $6\sqrt{3}$ models.

In addition to the incommensurate structure and vertical corrugation reducing the number of bonds to the buffer, the reflectivity results also show that the topmost Si interface layer is depleted to a density of $75 \pm 10\%$ of its bulk value. This places and even lower upper limit on the amount of buffer-interface bonds to $<24\%$. Si depletion may arise from Si vacancies, C substitutions or some combination thereof. XRR cannot distinguish this since Si is a stronger scatter than C. For example, the contribution to the interface structure factor of the top layer is $f_{Si1}\rho_{Si1}e^{-1/2(Q_z\sigma_{Si1})^2}e^{iQ_z z_{Si1}}$. Because the atomic form factor primarily depends on the atomic number, Z, and σ is constant, the Q_z dependence is essentially the same up to a scale factor and the following relation be can obtained,

$$\rho_{Si1} = \rho_{Si1}^{sub} + f_C/f_{Si}\rho_C^{sub}. \tag{5.10}$$

This relationship states that a one-to-one replacement of C substitutions will reduce the scattering from the interface, consistent with the findings from reflectivity. Consequently, additional studies such as TEM would be required to look specifically for vacancy and substitution concentrations at the interface. A depleted Si interface differs from the typically assumed bulk-terminated interface [61, 36]. Such an assumption was based on the lack of spectroscopic evidence. However, this is no longer the case as the XSW analysis of the C 1s BG_o core levels identified additional bulk components that may be related to the interface structure [see Figure 5.5].

A Si depleted density of 75% corresponds 24% of the buffer and places an upper limit on the number bonds. This is an upper limit because not every Si atom may bond to the buffer and the possibility of C substitutions, defined by equation 5.2.4, would act to further reduce the Si density. The XRR derived S_1 density of 26% is in excellent agreement with the Si depletion density. Since both of these results correspond to upper limits on bonding,

the reduced bonding prediction of 15% from incommensurate mutual modulation presented in Chapter 5 is also consistent.

Perhaps one of the more surprising results is the large corrugation (up to 2.4 Å) in BG_o [see Figure 5.12(a)]. The distribution is characterized by the sharp S_1 component and two additional broader components above S_1 . The vertical range of the corrugation is well defined, as evidenced by the relatively sharp σ's compared to the overall vertical distribution. Although the best fit of the BG_o reflectivity is obtained with three buffer components, this large vertical distribution was found to be component independent. This is similar to how a large distribution was obtained from the XSW analysis, regardless of the number components used to fit the C 1s spectra. Figure 5.11 shows the comparison between the density distribution obtained from XRR and XSW. In both cases, the density falls off at nearly the same distance near the interface and covers a large vertical distance. The reflectivity suggests that the density cutoff is much sharper near the interface and extends farther above the surface. Given the challenges of a proper decomposition of the C 1s XSW spectra to obtain accurate yield parameters, the reflectivity density distribution can be regarded as consistent with the XSW result.

The vertical distribution is larger than previous XSW results of 0.9 Å.[63] While the results may appear to be in contradiction, the discrepancy reflects the difference in growth method. Previous studies were on UHV grown samples where it is well known that UHV grown samples have a significant mixture of buffer and multilayer graphene. An important point is that BG_o and BG_{ML} are structurally different. In this case the reflectivity and XSW measurements would be some type of weighted average of BG_o and BG_{ML}. This is consistent their vertical distribution of being between BG_o (2.4 Å) and BG_{ML} (0.4 Å) [see Table 5.4]. Note a 50:50 average of the two buffers gives a corrugation of 1.4 Å, quite similar to the 0.9 Å reported in ref. [63].

A vertical corrugation of 0.9 Å was also observed with cross-sectional STEM.[116] However, TEM will place a lower, not upper, limit on the corrugation. The reasoning be-

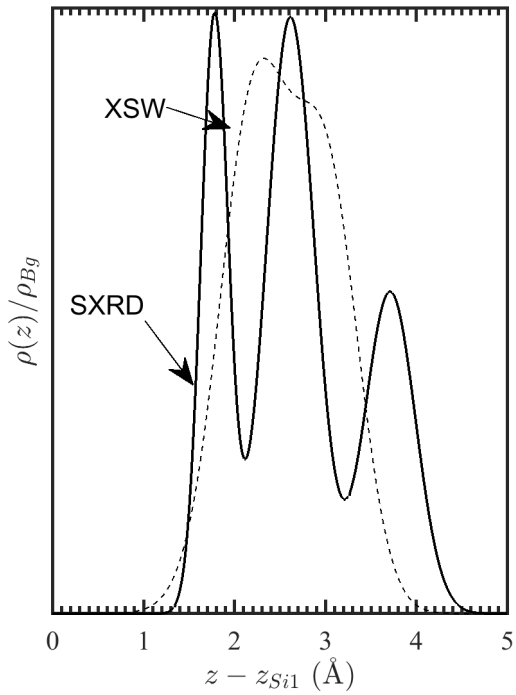

Figure 5.11: Comparison of the BG_o densities derived from SXRD reflectivity (solid line) and XSW (dashed line)

hind this is that It is possible that the particular cross-section observed did not pass through the maximumly corrugated section, or that the interaction with the polymer adhesive reduces the corrugation of BG_o.

More importantly, is it unclear if similar growth conditions were used to prepare the buffer samples and whether BG_o or BG_{ML} was measured. To elaborate on this further, consider the coverages of obtained for ML shown in Table 5.4 and Figure 5.12. It was found that the coverage of BG_{ML} is larger than the ML coverage by 18%. As a result, the reflectivity analysis suggests that the BG_{ML} structure is present not only beneath a graphene monolayer, but also without a monolayer above. A schematic of the coverage results for the ML sample is shown in Figure 5.13. Without the growth temperature fully specified, it is difficult to make direct comparisons to the STEM measurements. However, the bond length and lower limit on the corrugation suggest a consistency between the two reports.

Although more recent reports of buffer graphene have suggested a smaller corrugation

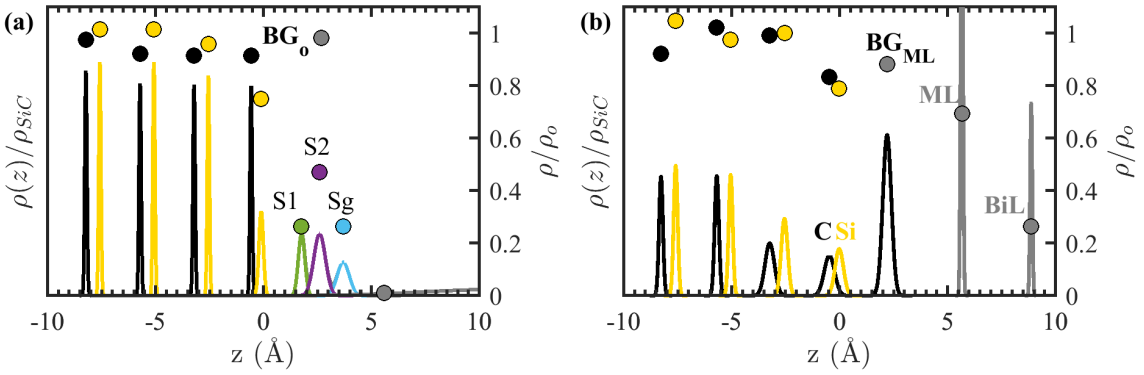

Figure 5.12: Vertical density distribution of BG_o (a) and ML (b) derived from the SXRD best fit parameters. The left axis refers to density distributions of the components. The integrated area of each component describes the total density for the given layer. For clarity, the layer density/coverage is plotted on the left axis. The density/coverage of each layer is normalized to its nominal value, i.e. a value of 1 for a Si (yellow) or C (black) interface layer corresponds to the layer density for bulk SiC. For BG_o in (a) the relative fraction of each component is plotted in green (S_1), purple (S_2) and light blue (S_g), while the overall coverage is shown in gray. Since the density of graphene monolayers is known, the plotted values represent coverage.

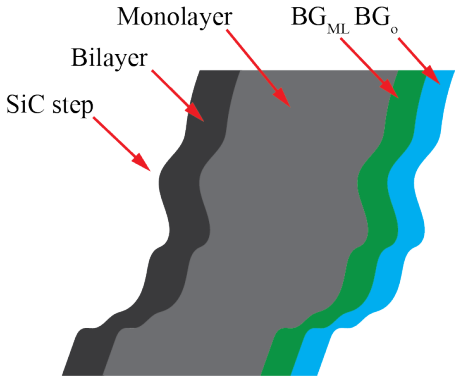

Figure 5.13: Schematic of the graphene coverages obtained from ML. A typical meandering SiC step is show and how monolayer growth propagates outward from the step. Bilayer graphene is closest to the step with the majority of the surface being covered in ML. In the regions where monolayer graphene has not formed, buffer graphene is present. Two buffers may be present on the surface, BG_{ML} and BG_o where BG_{ML} is closer to the ML.

of 0.9 Å, larger corrugations are not absent from the literature [53, 43]. In fact, STM measurements from Riedl *et al.* measured corrugations of certain sample regions up to 4 Å and Chen *et al.* measured 3.2 Å [53, 43]. Between these two reports, Chen *et al.* asserted that the corrugation was a real topographical effect while Riedl *et al.* claimed the corrugation was primarily an electronic effect. From the combination of the presented XSW and SXRD reflectivity analysis, these results support that they were indeed to a large degree topographical corrugations. Furthermore, the notion of a large vertical corrugation is consistent with island formation predicted from the incommensurate modulation model. The regions where bonding occurs form the boundaries between islands and this bonding induces some buckling that increases the distance from the SiC interface.

A dramatic change occurs in the buffer when a monolayer forms above it. The corrugation in BG_{ML} was drastically reduced (0.4 Å) and was well described by a single S_1 buffer component (as opposed to three). Note that while the average distance of BG_{ML} from the interface was 2.22 Å, this distance is much closer than the average distance for BG_o (2.69 Å). Even though a distance of 2.22 Å is slightly farther from the interface than S_1 in BG_o, the vertical width of BG_{ML} along with the width of the interface suggests that at least 30% of BG_{ML} is less than 2.1 Å from the interface indicating a similar, if not larger interaction with the interface. Recent ab initio calculations of the buffer+monolayer system corroborate the reflectivity results [132]. They found that BG_{ML} had a total width of 0.86 Å with a reasonably normal distribution. While their average height above the interface was slightly higher (2.36 Å), the equivalent width of $4\sigma = 0.8$ Å from reflectivity shares excellent agreement with their predicted width. A decrease in corrugation, although not as severe as the experimental observation, is also expected from theoretical calculations that showed corrugations of bare buffer being up to 1.2 Å.[67]

From reflectivity alone, it may be tempting to conclude that BG_{ML} is more ordered because of the decrease in vertical distribution. However, from analysis of the in-plane coherence and strain, it was found that BG_{ML} had the lowest long range order and the high-

est degree of in-plane RMS strain [see Figure 3.1 and Table 3.1]. Moreover, Figure 5.12 shows that the σ's in the interface layer increase and propagate deeper into the bulk. This paints the picture that once the ML is grown at a higher temperature, the interface becomes significantly more disordered. These results have many consequences on the structure and properties of the buffer and reveal the growth mechanisms at play.

In addition to the BG_{ML} having more strain and disorder, it also underwent a phase transition from an incommensurate to a commensurate phase. If the incommensurate phase in the bare buffer is considered to arise from comparable strengths of in-plane σ-bonds and sp^3-bonds with the interface, an increase in RMS strain and disorder may be sufficient to reduce the in-plane interaction strength and cause the periodicities in the buffer to be dominated by the underlying bulk SiC.

Perhaps surprisingly, a depleted Si interface with a similar depletion to BG_o was found for ML, even with the increased disorder. Furthermore, a similar Si depletion was found in previous UHV grown samples [63]. These results suggest that the depleted Si interface structure is an equilibrium structure. If the depletion fraction depended on growth conditions or layer coverage, it would be demonstrated here because in confinement controlled sublimation a nearly complete monolayer will only form at an increased temperature or decreased partial Si pressure compared to BG_o growth conditions. That is, multilayer growth on the Si-face is an activated process. A significant fraction of monolayer growth will not occur at the BG_o growth temperature. The fact that this Si depletion is consistent across growth temperature and growth method strongly point to the Si depleted layer as an equilibrium structure, not a variable factor dependent on growth conditions. This suggests that the incommensurate structure in the BG_o-SiC system is in fact driven by the energy gained in the depleted Si interface and the buffer-SiC bonding. It is expected that future theoretical work will support this assertion.

A depleted equilibrium structure also disrupts typical notions that 3.13 SiC bilayers are consumed to produce a graphene layer. If this were the case, the Si depletion density would

have a dependence on the number of graphene layers. Being that this is not the case, an excess of Si and C are expected to be present of the surface. Figure 5.12(a) demonstrates the presence of this contamination layer and was an essential feature for describing the reflectivity of BG_o at low Q_z.

Comparisons of the graphene coverage and overgrowth between the BG_o and ML surface reveals important distinctions in the growth mechanisms as well. At the BG_o growth temperature of 1400°C , there is nearly complete coverage ($\Theta_{BG_o} \approx 1$) and only a small fraction of graphene overgrowth ($<3\%$). This is contrasted with the ML surface that does not have a complete BG_{ML} or monolayer coverage, yet has a substantial coverage of bilayer graphene. The fact that the coverage of BG_{ML} is less than BG_o is not an inconsistency, but an observation that provides additional insights. It indicates that not all of the buffer from the ML surface was converted to the BG_{ML} form and a small fraction of BG_o may still be present on the surface. The remaining coverage of BG_o cannot be easily resolved from the reflectivity measurements for two reasons: (i) it's coverage is small and (ii) it's vertical distribution is large. The low coverage will provide diminishing diffracted intensity and the large vertical distributions in BG_o will reduce the diffracted intensity at higher Q_z. This means that the well defined vertical positions from the ML surface will dominate the reflectivity and a small fraction of BG_o will not substantially alter the results. See Figure 5.13 for a visual representation of these results.

Based off the coverages reported in Table 5.4 for ML, there are regions on the surface where BG_{ML} is present without a monolayer above. This provides evidence that the structure of BG_{ML} is also a result of its interaction with the interface, and influenced to a lesser degree by the monolayer above. These differences in layer coverages reveal differences in the graphene formation mechanism consistent with current kinetic models that graphene growth propagates from SiC step edges [97, 142, 143]. In this context, excellent layer control in BG_o is possible because the energy barrier for Si sublimation increases once a full buffer has formed and sublimation becomes more favorable at step edges.[144, 145, 146] A

consequence of this energy barrier is an increase in disorder of the interface due to trapped Si. As a result, Si sublimation continues to decrease with with increasing graphene layer coverage. However, the energy barrier increase is not as large compared to when buffer forms because Si sublimation remains favorable at step edges. Therefore, increased coverages of bilayer overgrowth can be expected on ML films when compared to monolayer overgrowth on BG_o films.

These changes in the buffer are consistent with the changes observed in the electronic structure with ARPES. Figure 3.5 showed how the π-bands change in BG_{ML}. There appeared to be at least a change in the doping level, if not a change in the band gap and band structure. Since the BG_{ML} is less corrugated and on average closer than BG_o, this may enable more charge transfer from SiC.[87, 147, 88] Also, the ϵ_2 band appeared to become less dispersive that correlates with increases in disorder inducing localization.[148]

5.3 Summary

In this Chapter, I presented a detailed XSW and XRR analysis of the buffer layer and monolayer graphene surfaces on SiC(0001). Using improved growth, a fully covered buffer layer was produced with minimal monolayer overgrowth. This enabled critical constraints on the analysis of photoemission and x-ray measurements and resolved ongoing discrepancies from earlier works, such as which spectral component is associated with buffer layer bonds to interface Si. Additionally, I went on to show that the SiC interface structure consists on an equilibrium concentration of Si vacancies with some C substitutions.

From XSW analysis and using the improved buffer layer samples, the BE component of the C 1s spectra associated with buffer carbon bonded to interface Si was correctly identified as S_1 (285.1 eV). It was found also that the amount of buffer C sp^3 bonded to Si was less than 24%, measurably lower than the amount predicted from ab initio calculations using a bulk terminated interface. However, the reflectivity results showed that the interface cannot be bulk terminated, but is Si depleted from 20-35% depending on the number of C

substitutions. This consequently reduces that number of sp^3 bonds allowed to buffer carbon to be significantly less than the 78% of interface Si predicted from ab initio calculations.

The reduction in the number of bonds can account for the large vertical corrugation of 2.4 Å in the bare buffer layer. A drastic change was observed in the buffer layer at the higher temperatures used or monolayer growth. Namely, the corrugation was reduced to $<$1 Å, there was an increase in system disorder and the average vertical position became much closer to the interface. These finding are consistent with the buffer layer becoming commensurate with bulk SiC and the changes in the electronic structure when a monolayer forms.

CHAPTER 6
CONCLUSIONS AND OUTLOOK

6.1 Thesis Summary

This thesis provided a detailed look into the structure and properties of the first layer of graphene grown on SiC(0001), often called the "buffer layer." One of the primary challenges facing the development of graphene electronic is a viable semiconducting form of graphene. This fact motivated a closer look at the buffer layer because initial calculations and measurements found it to be a wide band gap insulator with significant surface states [36, 64]. The presence of localized surface states was a significant issue for the buffer layer grown in UHV. Recently, it was shown that the buffer can be a semiconductor with a band gap $>$0.5 eV when using improved growth methods [62]. This result was not measured nor predicted theoretically.

This thesis resolved the issue of the semiconducting buffer through detailed surface x-ray diffraction measurements of the buffer-SiC interface in Chapter 3 and a corresponding study of tight binding calculations of the electronic structure based off of the SXRD results in Chapter 4. First, I showed that the buffer layer and the SiC interface were incommensurate, not the $(6\sqrt{3}\times6\sqrt{3})_{\mathrm{SiC}}\mathrm{R}30^{\circ}$ reconstruction assumed for the past forty years. A detailed analysis revealed a new understanding of this incommensurate interaction called an incommensurate mutual modulation. Based on the symmetry of the diffraction measurements, it was determined that the strength of the interactions caused graphene to distort the SiC interface and the SiC interface to distort the graphene. One implication of this finding was that the comparable strengths of intralayer and interlayer interactions produced competing periodicities that produced a new incommensurate period not found in either system.

Within this incommensurate model, the highly ordered interaction was determined to

predict the diffracted intensity with excellent agreement. The results showed that the in-plane bonds of the SiC interface were strongly modulated with density changes up to 30% compared to the nominal bulk areal density. On the other hand, while the graphene was indeed modulated, the in-plane bond distortion was found to be small, $<1\%$. Using this structure for determining the structural positions of the Si in the SiC interface, a tight binding model was developed to calculate the band structure of the buffer π-bands. It was found that an onsite potential based on in-plane bond distance provided the best estimate for the influence of interface Si on the graphene π-bands. Using this model for bonding criteria, the tight binding model was found to reproduce the band structure predictions from ab initio calculations of an unmodulated bulk terminated interface. This verification paved the way for addressing the incommensurate mutual modulation. The effect of different modulation amplitudes were studied to find that the experimentally determined modulation could open a substantial band gap up to 0.8 eV and provided excellent agreement with ARPES measurements. Moreover, band gap formation was found to be robust to changes in modulation amplitude and period. It was demonstrated that the band gap increased with increasing modulation amplitude and was stable within the experimental uncertainty of the modulation amplitude and period.

Having established the importance of incommensurate mutual modulation on the electronic properties of the buffer layer, I went on to address the mechanisms driving the incommensuration. Such a task is necessary if a proper understanding of the incommensuration can help establish pathways for methods of graphene band gap engineering. From this endeavor, it was found that not all buffer layers were the same and that different growth temperatures would provide different electronic and structural properties. For example, the bare buffer layer grown at 1400°C is highly ordered, incommensurate and semiconducting. However, the buffer layer that forms at higher growth temperatures where a monolayer is above the buffer is more disordered, commensurate and nearly metallic.

The measurements from Chapter 3 addressed only lateral information. To gain a better

understanding of these changes, detailed x-ray standing wave and x-ray reflectivity measurements were conducted to obtain detailed information regarding the vertical distributions and densities of the buffer layer and it interface layers. The results showed that the incommensurate bare buffer layer was highly corrugated with a vertical distribution spanning 1.7-2.5 Å. Its closest point to the interface was $\sim 1.87(9)$ Å, and given its similarity to the SiC bond distance of 1.89 Å, this provides evidence that some carbon atoms in the buffer layer are sp^3 bonded to Si in the interface. Although the bond it strong, the amount is significantly less than that predicted from ab initio calculations. Previous calculations predicted 78% of the interface Si was bonded to the buffer carbon. However, reflectivity results showed that the interface Si was depleted by 25%, potentially even more if C substitutions are present, indicating an upper limit on the number bonds to buffer carbon.

When considered together, the SXRD, XRR, and XSW results produce a clearer picture of the incommensurate BG_o-SiC interface. A schematic visual representation of the essential results are shown Figure 6.1. The result suggest that the presence of an ordered distribution of Si vacancies with possible C substitutions in the topmost SiC interface layer may be driving the incommensurate modulation. Furthermore, Si depletion is consistent with the fact that large density fluctuations were predicted in the SiC interface in Section 3.2. Where Si is present, the buffer graphene forms a strong sp^3 bond, that is labeled S_1. In the region of depleted Si, the interaction with the buffer layer is reduced and the buffer expands away from the surface. The result is a periodic, though incommensurate, vertical pinning and buckling in the buffer layer. From the schematic, it is clear that there are two types of buffer C not bonded to interface Si: (i) the sp^2 graphene in the graphene island (S_g), and $sp^2 - sp^3$ hybrid graphene near sp^3 carbon (S_2). The results suggest that island formation occurs in the regions of Si depletion. However, due to the higher density of graphene, there is still unbonded graphene in the regions of increased Si concentration. With these considerations it is reasonable to expect a 3-component density distribution similar to the results from XSW and XRR.

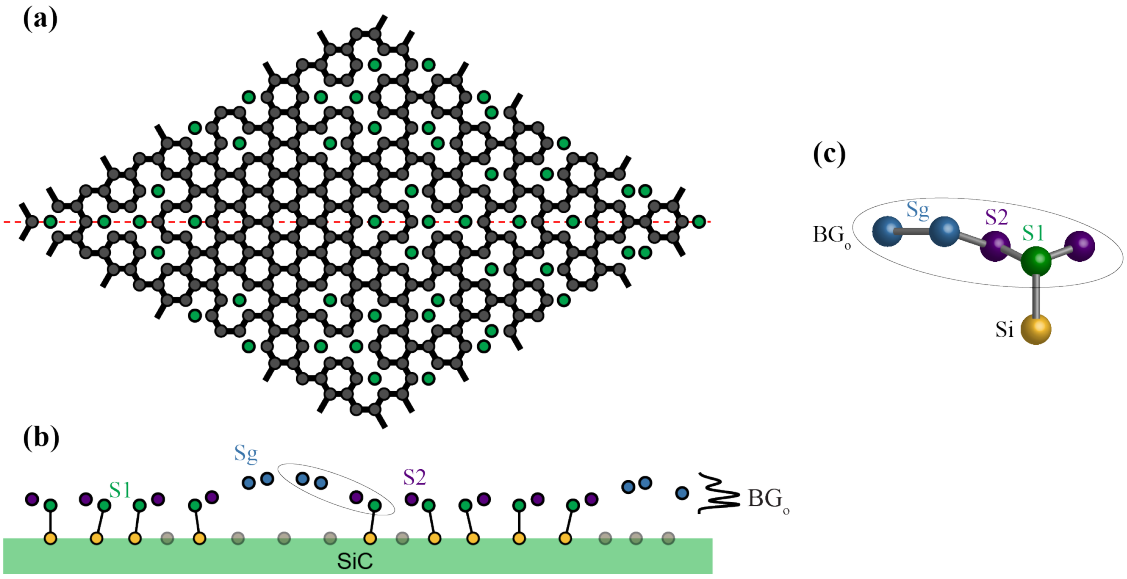

Figure 6.1: Schematic of the bonding and corrugation that arises from from the incommensurate BG_o. (a) The BG_o bonding configuration predicted from the incommensurate modulation of the SiC interface shown in Figure 4.3. (b) a vertical cut of the red line in (a) demonstrating the presence of Si vacancies (white), vertical corrugation and the necessary incorporation of 3 buffer components. S_1 (green) describes the buffer bonded to Si (yellow), S_2 (purple) describes unbonded buffer near S_1 , and S_g (blue) describes the unbonded buffer in the graphene islands. The x-ray reflectivity derived buffer density distribution is shown to demonstrate the feasibility of the vertical density distribution and its consistency with the bonding predicition.

Drastic differences are observed in the buffer layer when a monolayer forms above. The higher growth temperatures increase the disorder in the interface and the random strain in the buffer layer. As such, the system becomes commensurate as the ordered periodicities from bulk SiC dominate. This incommensurate-commensurate phase transition is accompanied with a decrease in the vertical corrugation and the average position of the buffer layer becomes closer to the interface compared to the bare buffer. These results are consistent with observed band structure changes where the semiconducting bands became more localized and experienced changes in doping.

6.2 Future Work

The results of this thesis have opened many new and exciting routes to graphene electronics. Perhaps one of the more exciting prospects of these results is the demonstration that the electronic structure of the buffer layer can be controlled and altered. Up until this point, studies have demonstrated that the buffer can be converted to quasi-free standing graphene, but these results show that different buffer layers are also possible. Such a concept was not anticipated prior to this work. It was assumed that the strong interaction between the buffer layer and SiC meant the properties were fixed. Compounding this with the observation of localized surface states of early measurements meant that not only were the properties of the buffer layer fixed, they were unfavorable.

At present, it is unclear if the bare buffer layer in its current state will have the appropriate transport properties for technological applications. Transport properties of incommensurate systems is still an ongoing field of research. Although the buffer layer is ordered structurally, the aperiodic nature of incommensurate systems may lead to electronic disorder. There are some signs of this from ARPES measurements. There are many splittings of the π-bands at larger energy, the width of the dispersive bands are large compared to monolayer graphene and the bandwidth of the ϵ_2 band is small indicating the state may be weakly localized. It may therefore be necessary to alter the interaction of the SiC interface

to produce a more *electronically* ordered interaction.

The results of this thesis suggests a path forward. X-ray reflectivity analysis of the buffer layer and monolayer samples showed that a depleted Si equilibrium structure is present in the interface layers. This equilibrium structure was observed in UHV grown samples. A consequence of this is that changing the growth conditions, such as partial Si pressure or temperature, may not alter the electronic properties other than to improve sample order. Such an endeavor may be a worthwhile path as there is a trade off between growth temperature and Si partial pressure. Too low a pressure increases sample inhomogeneity while too high a temperature increases the disorder in the interface. It may be that the current growth conditions can be further optimized.

Alternatively, the equilibrium structure suggests that tailoring the buffer properties may require post-processing, structured growth, or a different growth environment. One post-processing option includes Si intercalation to alter the interface bonding configuration. Intercalation of the buffer layer at this point has focused on the production of quasi-freestanding graphene.[61, 132, 149, 150, 110] From the reflectivity analysis in Chapter 5, I showed that Si can interact strongly with the buffer layer. If Si vacancies are present in the interface, as opposed to C substitutions, incorporation of Si into the interface layer may alter the structure of the buffer. It may potentially, saturate dangling bonds, increase the interaction such that bulk periodicities may dominate to establish a commensurate structure and change the electronic properties. At present, there have been a few studies of Si intercalation of graphene on SiC(0001) suggesting the formation of quasi-freestanding graphene [151, 152]. Currently there has not been ARPES measurements to validate these claims, the results suggest that controlling the Si concentration available for intercalation can control whether the buffer layer is a semiconductor or quasi-freestanding graphene.

Another route for changing the electronic structure of the buffer layer is through structured growth. Incommensurate systems necessarily need long range order for the incommensurate structure to be measured and established. It is well known that defects can pin

the incommensurate structure to force commensuration [112]. The long range order determined for the buffer layer was 60 nm [see Table 3.1]. Current electron beam lithography methods can routinely pattern features below this threshold on SiC. By patterning trenches into the SiC substrate smaller than 60 nm to produce buffer nanoribbons by methods similar to refs. [47, 48], the long range order can be reduced and the properties of the buffer controlled. Just like edge terminations, such as armchair or zig-zag, in graphene nanoribbons produce significantly different properties, such considerations are likely relevant for buffer nanoribbons.

Finally, I suggest that the introduction of partial pressures of other chemical species during the growth of the buffer layer may provide another route towards tailoring the band gap and electronic properties of the buffer layer. The equilibrium interface structure suggests that changing the Si partial pressure may not have a dramatic effect on the structure and properties of the buffer layer. Incorporation of other partial pressures such as nitrogen, germanium or fluorine may develop another equilibrium structure. Such methods may have an advantage over intercalation. Most studies of post-processing methods to alter graphene, such as lithography or hydrogenation, increase the disorder in the system because the method is inherently random at the atomic scale. By introducing controlled "contamination" during the growth process, the minimum energy configuration may be more easily attainable.

The results of this thesis pave the way for new routes towards the development of graphene based electronics. The buffer has many promising characteristics making it suitable for use in electronics. It is crystallographically aligned with SiC and large and homogeneous areas can more easily be produced compared to monolayer graphene on SiC(0001) or SiC($000\bar{1}$). Furthermore, the semiconducting properties of the buffer layer is a "bulk" property, i.e. advanced lithography or post-processing in not required to open band gaps. As such new device architectures can be imagined, such as the pnp junction proposed in Figure 3.5 or others that exploit the intrinsic band gap of the buffer along with its malleabil-

ity.

REFERENCES

[1] C. Berger, Z. Song, T. Li, X. Li, A. Y. Ogbazghi, R. Feng, Z. Dai, A. N. Marchenkov, E. H. Conrad, P. N. First, and W. A. de Heer, "Ultrathin epitaxial graphite: 2D electron gas properties and a route toward graphene-based nanoelectronics," *J. Phys. Chem. B*, vol. 108, no. 52, pp. 19 912–19 916, 2004.

[2] C. Berger, Z. Song, X. Li, X. Wu, N. Brown, C. Naud, D. Mayou, T. Li, J. Hass, A. N. Marchenkov, E. H. Conrad, P. N. First, and W. A. de Heer, "Electronic confinement and coherence in patterned epitaxial graphene," *Science*, vol. 312, no. 5777, pp. 1191–1196, 2006.

[3] A. K. Geim and K. S. Novoselov, "The rise of graphene," *Nat. Mater.*, vol. 6, no. 3, pp. 183–191, 2007.

[4] K. S. Novoselov, A. K. Geim, S. V. Morozov, D. Jiang, Y. Zhang, S. V. Dubonos, I. V. Grigorieva, and A. A. Firsov, "Electric field effect in atomically thin carbon films," *Science*, vol. 306, no. 5696, pp. 666–669, 2004.

[5] R. Saito, G. Dresselhaus, M. S. Dresselhaus, and Others, *Physical properties of carbon nanotubes*. World Scientific, 1998, vol. 35.

[6] A. A. Ahmadieh and H. A. Rafizadeh, "Dispersion curves and elastic constants of graphite," *Phys. Rev. B*, vol. 7, no. 10, pp. 4527–4537, 1973.

[7] J. B. Nelson and D. P. Riley, "The thermal expansion of graphite from 15°C to 800°C: part I. experimental," *Proc. Phys. Soc.*, vol. 57, no. 6, p. 477, 1945.

[8] Y. Baskin and L. Meyer, "Lattice constants of graphite at low temperatures," *Phys. Rev.*, vol. 100, no. 2, p. 544, 1955.

[9] A. Bosak, M. Krisch, M. Mohr, J. Maultzsch, and C. Thomsen, "Elasticity of single-crystalline graphite: inelastic x-ray scattering study," *Phys. Rev. B*, vol. 75, no. 15, p. 153 408, 2007.

[10] G. D. Barrera, J. A. O. Bruno, T. H. K. Barron, and N. L. Allan, "Negative thermal expansion," *J. Phys Cond. Mat.*, vol. 17, no. 4, R217, 2005.

[11] M. Weinert, E. Wimmer, and A. J. Freeman, "Total energy all electron density functional method for bulk solids and surfaces," *Phys. Rev. B*, vol. 26, no. 8, pp. 4571–4578, 1982.

[12] H. Şahin, S. Cahangirov, M. Topsakal, E. Bekaroglu, E. Akturk, R. T. Senger, and S. Ciraci, "Monolayer honeycomb structures of group-IV elements and III-V binary compounds: First-principles calculations," *Phys. Rev. B*, vol. 80, no. 15, p. 155 453, 2009.

[13] S. Wang, "Studies of physical and chemical properties of two-dimensional hexagonal crystals by first-principles calculation," *J. Phys. Soc. Jap.*, vol. 79, no. 6, p. 64 602, 2010.

[14] J. Zhao, H. Liu, Z. Yu, R. Quhe, S. Zhou, Y. Wang, C. C. Liu, H. Zhong, N. Han, J. Lu, Y. Yao, and K. Wu, "Rise of silicene: A competitive 2D material," *Prog. Mater. Sci.*, vol. 83, pp. 24–151, 2016.

[15] H. Liu, A. T. Neal, Z. Zhu, Z. Luo, X. Xu, D. Tománek, and P. D. Ye, "Phosphorene: an unexplored 2D semiconductor with a high hole mobility," *ACS Nano*, vol. 8, no. 4, pp. 4033–4041, 2014.

[16] J. A. Sears, M. Songvilay, K. W. Plumb, J. P. Clancy, Y. Qiu, Y. Zhao, D. Parshall, and Y.-J. Kim, "Magnetic order in α-$RuCl_3$: a honeycomb-lattice quantum magnet with strong spin-orbit coupling," *Phys. Rev. B*, vol. 91, no. 14, p. 144 420, 2015.

[17] B. Radisavljevic, A. Radenovic, J. Brivio, V. Giacometti, and A. Kis, "Single-layer MoS_2 transistors," *Nat. Nano.*, vol. 6, no. 3, pp. 147–150, 2011.

[18] P. R. Wallace, "The band theory of graphite," *Phys. Rev.*, vol. 71, no. 9, pp. 622–634, 1947.

[19] C. Coletti, S. Forti, A. Principi, K. V. Emtsev, A. A. Zakharov, K. M. Daniels, B. K. Daas, M. V. S. Chandrashekhar, T. Ouisse, D. Chaussende, A. H. MacDonald, M. Polini, and U. Starke, "Revealing the electronic band structure of trilayer graphene on SiC: an angle-resolved photoemission study," *Phys. Rev. B*, vol. 88, no. 15, p. 155 439, 2013.

[20] A. Grüneis, C. Attaccalite, L. Wirtz, H. Shiozawa, R. Saito, T. Pichler, and A. Rubio, "Tight-binding description of the quasiparticle dispersion of graphite and few-layer graphene," *Phys. Rev. B*, vol. 78, no. 20, p. 205 425, 2008.

[21] H. Raza, *Graphene nanoelectronics: metrology, synthesis, properties and applications*. Springer Science & Business Media, 2012.

[22] K. Wakabayashi, K.-i. Sasaki, T. Nakanishi, and T. Enoki, "Electronic states of graphene nanoribbons and analytical solutions," *Sci. Technol. Adv. Mater.*, vol. 11, no. 5, p. 54 504, 2010.

[23] M. Vanević, V. M. Stojanović, and M. Kindermann, "Character of electronic states in graphene antidot lattices: flat bands and spatial localization," *Phys. Rev. B*, vol. 80, no. 4, p. 45 410, 2009.

[24] Y.-W. Son, M. L. Cohen, and S. G. Louie, "Energy gaps in graphene nanoribbons," *Phys. Rev. Lett.*, vol. 97, no. 21, p. 216 803, 2006.

[25] V. Barone, O. Hod, and G. E. Scuseria, "Electronic structure and stability of semiconducting graphene nanoribbons," *Nano Lett.*, vol. 6, no. 12, pp. 2748–2754, 2006.

[26] M. Y. Han, J. C. Brant, and P. Kim, "Electron transport in disordered graphene nanoribbons," *Phys. Rev. Lett.*, vol. 104, no. 5, p. 56 801, 2010.

[27] M. Y. Han, B. Özyilmaz, Y. Zhang, and P. Kim, "Energy band-gap engineering of graphene nanoribbons," *Phys. Rev. Lett.*, vol. 98, no. 20, p. 206 805, 2007.

[28] V. M. Pereira, A. H. Castro Neto, and N. M. R. Peres, "Tight-binding approach to uniaxial strain in graphene," *Phys. Rev. B*, vol. 80, no. 4, p. 45 401, 2009.

[29] C. Chamon, "Solitons in carbon nanotubes," *Phys. Rev. B*, vol. 62, no. 4, pp. 2806–2812, 2000.

[30] I. I. Naumov and A. M. Bratkovsky, "Gap opening in graphene by simple periodic inhomogeneous strain," *Phys. Rev. B*, vol. 84, no. 24, p. 245 444, 2011.

[31] C. Gutierrez, C.-J. Kim, L. Brown, T. Schiros, D. Nordlund, E. B. Lochocki, K. M. Shen, J. Park, and A. N. Pasupathy, "Imaging chiral symmetry breaking from Kekule bond order in graphene," *Nat Phys*, vol. 12, no. 10, pp. 950–958, 2016.

[32] D. Haberer, D. V. Vyalikh, S. Taioli, B. Dora, M. Farjam, J. Fink, D. Marchenko, T. Pichler, K. Ziegler, S. Simonucci, M. S. Dresselhaus, M. Knupfer, B. Büchner, and A. Grüneis, "Tunable band gap in hydrogenated quasi-free-standing graphene," *Nano Lett.*, vol. 10, no. 9, pp. 3360–3366, 2010.

[33] Y. Zhang, T.-T. Tang, C. Girit, Z. Hao, M. C. Martin, A. Zettl, M. F. Crommie, Y. R. Shen, and F. Wang, "Direct observation of a widely tunable bandgap in bilayer graphene," *Nature*, vol. 459, no. 7248, pp. 820–823, 2009.

[34] S. Y. Zhou, G.-H. Gweon, A. V. Fedorov, P. N. First, W. A. de Heer, D.-H. Lee, F. Guinea, A. H. Castro Neto, and A. Lanzara, "Substrate-induced bandgap opening in epitaxial graphene," *Nat. Mater*, vol. 6, no. 10, pp. 770–775, 2007.

[35] C. Enderlein, Y. S. Kim, A. Bostwick, E. Rotenberg, and K. Horn, "The formation of an energy gap in graphene on ruthenium by controlling the interface," *New J. Phys.*, vol. 12, no. 3, p. 33 014, 2010.

[36] K. V. Emtsev, F. Speck, T. Seyller, L. Ley, and J. D. Riley, "Interaction, growth, and ordering of epitaxial graphene on SiC(0001) surfaces: a comparative photoelectron spectroscopy study," *Phys. Rev. B*, vol. 77, no. 15, p. 155 303, 2008.

[37] W. A. de Heer, C. Berger, M. Ruan, M. Sprinkle, X. Li, Y. Hu, B. Zhang, J. Hankinson, and E. H. Conrad, "Large area and structured epitaxial graphene produced by confinement controlled sublimation of silicon carbide," *Proc. Nat. Acad. Sci.*, vol. 108, no. 41, pp. 16 900–16 905, 2011.

[38] A. Reina, X. Jia, J. Ho, D. Nezich, H. Son, V. Bulovic, M. S. Dresselhaus, and J. Kong, "Large area, few-layer graphene films on arbitrary substrates by chemical vapor deposition," *Nano Lett.*, vol. 9, no. 1, pp. 30–35, 2009.

[39] S. Stankovich, D. A. Dikin, R. D. Piner, K. A. Kohlhaas, A. Kleinhammes, Y. Jia, Y. Wu, S. T. Nguyen, and R. S. Ruoff, "Synthesis of graphene-based nanosheets via chemical reduction of exfoliated graphite oxide," *Carbon N. Y.*, vol. 45, no. 7, pp. 1558–1565, 2007.

[40] A. J. Van Bommel, J. E. Crombeen, and A. Van Tooren, "LEED and auger electron observations of the SiC(0001) surface," *Surf. Sci.*, vol. 48, no. 2, pp. 463–472, 1975.

[41] K. V. Emtsev, A. Bostwick, K. Horn, J. Jobst, G. L. Kellogg, L. Ley, J. L. McChesney, T. Ohta, S. A. Reshanov, J. Rohrl, E. Rotenberg, A. K. Schmid, D. Waldmann, H. B. Weber, and T. Seyller, "Towards wafer-size graphene layers by atmospheric pressure graphitization of silicon carbide," *Nat. Mater.*, vol. 8, no. 3, pp. 203–207, 2009.

[42] K. V. Emtsev, T. Seyller, F. Speck, L. Ley, P. Stojanov, J. D. Riley, and R. C. G. Leckey, "Initial stages of the graphite-SiC(0001) interface formation studied by photoelectron spectroscopy," *Mater. Sci. Forum*, vol. 556-557, pp. 525–528, 2007.

[43] C. Riedl, U. Starke, J. Bernhardt, M. Franke, and K. Heinz, "Structural properties of the graphene-SiC(0001) interface as a key for the preparation of homogeneous large-terrace graphene surfaces," *Phys. Rev. B*, vol. 76, no. 24, p. 245 406, 2007.

[44] R. M. Tromp and J. B. Hannon, "Thermodynamics and kinetics of graphene growth on SiC(0001)," *Phys. Rev. Lett.*, vol. 102, no. 10, p. 106 104, 2009.

[45] F. Owman and P. Mårtensson, "The SiC(0001) $6\sqrt{3} \times 6\sqrt{3}$ reconstruction studied with STM and LEED," *Surf. Sci.*, vol. 369, no. 1-3, pp. 126–136, 1996.

[46] J. Hass, W. A. de Heer, and E. H. Conrad, "The growth and morphology of epitaxial multilayer graphene," *J. Phys. Condens. Matter*, vol. 20, no. 32, p. 323 202, 2008.

[47] J. Hicks, A. Tejeda, A. Taleb-Ibrahimi, M. S. Nevius, F. Wang, K. Shepperd, J. Palmer, F. Bertran, P. Le Fevre, J. Kunc, W. A. de Heer, C. Berger, and E. H. Conrad, "A wide-bandgap metal-semiconductor-metal nanostructure made entirely from graphene," *Nat. Phys.*, vol. 9, no. 1, pp. 49–54, 2013.

[48] M. S. Nevius, F. Wang, C. Mathieu, N. Barrett, A. Sala, T. O. Menteç, A. Locatelli, and E. H. Conrad, "The bottom-up growth of edge specific graphene nanoribbons," *Nano Lett.*, vol. 14, no. 11, pp. 6080–6086, 2014.

[49] M.-H. Tsai, C. S. Chang, J. D. Dow, and I. S. T. Tsong, "Electronic contributions to scanning-tunneling-microscopy images of an annealed β-SiC(111) surface," *Phys. Rev. B*, vol. 45, no. 3, pp. 1327–1332, 1992.

[50] J. Hass, F. Varchon, J. E. Millán-Otoya, M. Sprinkle, N. Sharma, W. A. de Heer, C. Berger, P. N. First, L. Magaud, and E. H. Conrad, "Why multilayer graphene on 4H-SiC(000$\overline{1}$) behaves like a single sheet of graphene," *Phys. Rev. Lett.*, vol. 100, no. 12, p. 125 504, 2008.

[51] M. Sprinkle, J. Hicks, A. Tejeda, A. Taleb-Ibrahimi, P. Le Fèvre, F. Bertran, H. Tinkey, M. C. Clark, P. Soukiassian, D. Martinotti, J. Hass, and E. H. Conrad, "Multilayer epitaxial graphene grown on the 4H-SiC(000$\overline{1}$) surface; structure and electronic properties," *J. Phys. D. Appl. Phys.*, no. 37, p. 374 006,

[52] G. M. Rutter, N. P. Guisinger, J. N. Crain, E. A. A. Jarvis, M. D. Stiles, T. Li, P. N. First, and J. A. Stroscio, "Imaging the interface of epitaxial graphene with silicon carbide via scanning tunneling microscopy," *Phys. Rev. B*, vol. 76, no. 23, p. 235 416, 2007.

[53] W. Chen, H. Xu, L. Liu, X. Gao, D. Qi, G. Peng, S. C. Tan, Y. Feng, K. P. Loh, and A. T. S. Wee, "Atomic structure of the 6H-SiC(0001) nanomesh," *Surf. Sci.*, vol. 596, no. 13, pp. 176–186, 2005.

[54] Y. Qi, S. H. Rhim, G. F. Sun, M. Weinert, and L. Li, "Epitaxial graphene on SiC(0001): more than just honeycombs," *Phys. Rev. Lett.*, vol. 105, no. 8, p. 85 502, 2010.

[55] I. Forbeaux, J. M. Themlin, and J. M. Debever, "Heteroepitaxial graphite on 6H-SiC(0001): interface formation through conduction-band electronic structure," *Phys. Rev. B*, vol. 58, no. 24, pp. 16 396–16 406, 1998.

[56] P. Mallet, F. Varchon, C. Naud, L. Magaud, C. Berger, and J.-Y. Veuillen, "Electron states of mono- and bilayer graphene on SiC probed by scanning-tunneling microscopy," *Phys. Rev. B*, vol. 76, no. 4, p. 41 403, 2007.

[57] C. Riedl, C. Coletti, and U. Starke, "Structural and electronic properties of epitaxial graphene on SiC(0001): A review of growth, characterization, transfer doping and hydrogen intercalation," *J. Phys. D. Appl. Phys.*, vol. 43, no. 37, p. 374 009, 2010.

[58] A. Charrier, A. Coati, T. Argunova, F. Thibaudau, Y. Garreau, R. Pinchaux, I. Forbeaux, J.-M. Debever, M. Sauvage-Simkin, and J.-M. Themlin, "Solid-state decomposition of silicon carbide for growing ultra-thin heteroepitaxial graphite films," *J. Appl. Phys.*, vol. 92, no. 5, p. 5, 2002.

[59] J. Hass, J. E. Millán-Otoya, P. N. First, and E. H. Conrad, "Interface structure of epitaxial graphene grown on 4H-SiC(0001)," *Phys. Rev. B*, vol. 78, no. 20, p. 205 424, 2008.

[60] S. Goler, C. Coletti, V. Piazza, P. Pingue, F. Colangelo, V. Pellegrini, K. V. Emtsev, S. Forti, U. Starke, F. Beltram, and S. Heun, "Revealing the atomic structure of the buffer layer between SiC(0001) and epitaxial graphene," *Carbon N. Y.*, vol. 51, pp. 249–254, 2013.

[61] C. Riedl, C. Coletti, T. Iwasaki, A. A. Zakharov, and U. Starke, "Quasi-free-standing epitaxial graphene on SiC obtained by hydrogen intercalation," *Phys. Rev. Lett.*, vol. 103, no. 24, p. 246 804, 2009.

[62] M. S. Nevius, M. Conrad, F. Wang, A. Celis, M. N. Nair, A. Taleb-Ibrahimi, A. Tejeda, and E. H. Conrad, "Semiconducting graphene from highly ordered substrate interactions," *Phys. Rev. Lett.*, vol. 115, no. 13, p. 136 802, 2015.

[63] J. D. Emery, B. Detlefs, H. J. Karmel, L. O. Nyakiti, D. K. Gaskill, M. C. Hersam, J. Zegenhagen, and M. J. Bedzyk, "Chemically resolved interface structure of epitaxial graphene on SiC(0001)," *Phys. Rev. Lett.*, vol. 111, no. 21, p. 215 501, 2013.

[64] F. Varchon, R. Feng, J. Hass, X. Li, B. N. Nguyen, C. Naud, P. Mallet, J.-Y. Veuillen, C. Berger, E. H. Conrad, and L. Magaud, "Electronic structure of epitaxial graphene layers on SiC: effect of the substrate," *Phys. Rev. Lett.*, vol. 99, no. 12, p. 126 805, 2007.

[65] A. Mattausch and O. Pankratov, "Ab initio study of graphene on SiC," *Phys. Rev. Lett.*, vol. 99, no. 7, p. 76 802, 2007.

[66] S. Kim, J. Ihm, H. J. Choi, and Y.-W. Son, "Origin of anomalous electronic structures of epitaxial graphene on silicon carbide," *Phys. Rev. Lett.*, vol. 100, no. 17, p. 176 802, 2008.

[67] F. Varchon, P. Mallet, J. Y. Veuillen, and L. Magaud, "Ripples in epitaxial graphene on the Si-terminated SiC(0001) surface," *Phys. Rev. B*, vol. 77, no. 23, p. 235 412, 2008.

[68] T. Cavallucci and V. Tozzini, "Multistable rippling of graphene on SiC: a density functional theory study," *J. Phys. Chem. C*, vol. 120, no. 14, pp. 7670–7677, 2016.

[69] G. Sclauzero and A. Pasquarello, "Carbon rehybridization at the graphene/SiC(0001) interface: effect on stability and atomic-scale corrugation," *Phys. Rev. B*, vol. 85, no. 16, p. 161 405, 2012.

[70] I. K. Robinson and D. J. Tweet, "Surface x-ray-diffraction," *Rep. Prog. Phys.*, vol. 55, no. 5, pp. 599–651, 1992.

[71] P. J. Brown, A. G. Fox, E. N. Maslen, M. A. O'Keefe, and B. T. M. Willis, "Intensity of diffracted intensities," in *Int. Tables Crystallogr. Vol. C Math. Phys. Chem. tables*, E Prince, Ed. Dordrecht: Springer Netherlands, 2004, pp. 554–595, ISBN: 978-1-4020-5408-2.

[72] D. T. Cromer, "Calculation of anomalous scattering factors at arbitrary wavelengths," *J. Appl. Crystallogr.*, vol. 16, no. 4, p. 437, 1983.

[73] E Conrad, "Diffraction methods, ch. 7," in *Handbook of Surface Science*, U. W. N., Ed., vol. Volume 1 - Physical Structure, Elsevier Science B. V., 1996, pp. 271–360, ISBN: 1573-4331.

[74] O. Robach, Y. Garreau, K. Aïd, and M. B. Véron-Jolliot, "Corrections for surface x-ray diffraction measurements using the *Z*-axis geometry: finite size effects in direct and reciprocal space," *J. Appl. Crystallogr.*, vol. 33, no. 4, pp. 1006–1018, 2000.

[75] E. Vlieg, "Integrated intensities using a six-circle surface x-ray diffractometer," *J. Appl. Crystallogr.*, vol. 30, no. 5 Part 1, pp. 532–543, 1997.

[76] P. Coppens, *Synchrotron radiation crystallography*, D. Cox, E. Vlieg, and I. K. I. K. Robinson, Eds. London: London: Academic Press, 1992.

[77] G. S. Brown and M. D. E., Eds., *Handbook on Synchrotron Radiation, Vol. 3*. Elseveir, 1991, pp. 221–266.

[78] E. D. Specht and F. J. Walker, "A method for the accurate determination of crystal truncation rod intensities by x-ray diffraction," *J. Appl. Cryst.*, vol. 26, no. 2, pp. 166–171, 1993.

[79] M. Lohmeier and E. Vlieg, "Angle calculations for a six-circle surface x-ray diffractometer," *J. Appl. Crystallogr.*, vol. 26, no. 5, pp. 706–716, 1993.

[80] A. Bauer, P. Reischauer, J. Kräusslich, N. Schell, W. Matz, and K. Goetz, "Structure refinement of the silicon carbide polytypes 4H and 6H: unambiguous determination of the refinement parameters," *Acta Crystallogr. Sect. A*, vol. 57, no. 1, pp. 60–67, 2001.

[81] H Hertz, "Ueber einen einfluss des ultravioletten lichtes auf die electrische entladung," *Ann. Phys.*, vol. 267, no. 8, pp. 983–1000, 1887.

[82] A Einstein, "Über einen die erzeugung und verwandlung des lichtes betreffenden heuristischen gesichtspunkt," *Ann. Phys.*, vol. 322, no. 6, pp. 132–148, 1905.

[83] C. S. Fadley, "Basic concepts of x-ray photoelectron spectroscopy," *Electron Spectrosc. theory, Tech. Appl.*, vol. 2, pp. 1–156,

[84] A. Bostwick, T. Ohta, T. Seyller, K. Horn, and E. Rotenberg, "Quasiparticle dynamics in graphene," *Nat. Phys.*, vol. 3, no. 1, pp. 36–40, 2007.

[85] Y. Liu, G. Bian, T. Miller, and T.-C. Chiang, "Visualizing electronic chirality and berry phases in graphene systems using photoemission with circularly polarized light," *Phys. Rev. Lett.*, vol. 107, no. 16, p. 166 803, 2011.

[86] E. L. Shirley, L. J. Terminello, A. Santoni, and F. J. Himpsel, "Brillouin-zone-selection effects in graphite photoelectron angular distributions," *Phys. Rev. B*, vol. 51, no. 19, pp. 13 614–13 622, 1995.

[87] S. Mammadov, J. Ristein, R. J. Koch, M. Ostler, C. Raidel, M. Wanke, R. Vasiliauskas, R. Yakimova, and T. Seyller, "Polarization doping of graphene on silicon carbide," *2D Mater.*, vol. 1, no. 3, p. 35 003, 2014.

[88] J. Ristein, S. Mammadov, and T. Seyller, "Origin of doping in quasi-free-standing graphene on silicon carbide," *Phys. Rev. Lett.*, vol. 108, no. 24, p. 246 104, 2012.

[89] A. Damascelli, "Probing the electronic structure of complex systems by ARPES," *Phys. Scr.*, vol. 2004, no. T109, p. 61, 2004.

[90] M. Sprinkle, D. Siegel, Y. Hu, J. Hicks, A. Tejeda, A. Taleb-Ibrahimi, P. Le Fèvre, F. Bertran, S. Vizzini, H. Enriquez, S. Chiang, P. Soukiassian, C. Berger, W. A.

de Heer, A. Lanzara, and E. H. Conrad, "First direct observation of a nearly ideal graphene band structure," *Phys. Rev. Lett.*, vol. 103, no. 22, p. 226 803, 2009.

[91] J. Zegenhagen, "Surface structure determination with x-ray standing waves," *Surf. Sci. Rep.*, vol. 18, no. 78, pp. 202–271, 1993.

[92] I. A. Vartanyants and M. V. Kovalchuk, "Theory and applications of x-ray standing waves in real crystals," *Rep. Prog. Phys.*, vol. 64, no. 9, p. 1009, 2001.

[93] M. J. Bedzyk, "X-ray standing wave techniques," in *Encycl. Condens. Matter Phys.* Elseveir, 2005, vol. 6, pp. 330–341.

[94] A. Authier, "Dynamical theory of x-ray diffraction," in *Int. Tables Crystallogr. Vol. B Reciprocal Sp.* U Shmueli, Ed. Dordrecht: Springer Netherlands, 2001, pp. 534–551, ISBN: 978-1-4020-5407-5.

[95] D. P. Woodruff, "Surface structure determination using x-ray standing waves," *Rep. Prog. Phys.*, vol. 68, no. 4, pp. 743–798, 2005.

[96] I. A. Vartanyants and J. Zegenhagen, "Photoelectric scattering from an x-ray interference field," *Solid State Commun.*, vol. 113, no. 6, pp. 299–320, 1999.

[97] M. Hupalo, E. H. Conrad, and M. C. Tringides, "Growth mechanism for epitaxial graphene on vicinal 6H-SiC(0001) surfaces: a scanning tunneling microscopy study," *Phys. Rev. B*, vol. 80, no. 4, p. 41 401, 2009.

[98] J. Robinson, X. Weng, K. Trumbull, R. Cavalero, M. Wetherington, E. Frantz, M. LaBella, Z. Hughes, M. Fanton, and D. Snyder, "Nucleation of epitaxial graphene on SiC(0001)," *ACS Nano*, vol. 4, no. 1, pp. 153–158, 2010.

[99] Z. H. Ni, W. Chen, X. F. Fan, J. L. Kuo, T. Yu, A. T. S. Wee, and Z. X. Shen, "Raman spectroscopy of epitaxial graphene on a SiC substrate," *Phys. Rev. B*, vol. 77, no. 11, p. 115 416, 2008.

[100] F. Fromm, P. Wehrfritz, M. Hundhausen, and T. Seyller, "Looking behind the scenes: raman spectroscopy of top-gated epitaxial graphene through the substrate," *New J. Phys.*, vol. 15, no. 11, p. 113 006, 2013.

[101] W. Strupinski, K. Grodecki, P. Caban, P. Ciepielewski, I. Jozwik-Biala, and J. M. Baranowski, "Formation mechanism of graphene buffer layer on SiC(0001)," *Carbon N. Y.*, vol. 81, pp. 63–72, 2015.

[102] J. Röhrl, M. Hundhausen, K. V. Emtsev, T. Seyller, R. Graupner, and L. Ley, "Raman spectra of epitaxial graphene on SiC(0001)," *Appl. Phys. Lett.*, vol. 92, no. 20, p. 201 918, 2008.

[103] L. M. Malard, M. A. Pimenta, G. Dresselhaus, and M. S. Dresselhaus, "Raman spectroscopy in graphene," *Phys. Rep.*, vol. 473, no. 56, pp. 51–87, 2009.

[104] R. Beams, L. G. Cançado, and L. Novotny, "Raman characterization of defects and dopants in graphene," *J. Phys. Condens. Matter*, vol. 27, no. 8, p. 83 002, 2015.

[105] T. Schumann, M. Dubslaff, M. H. Oliveira, M. Hanke, J. M. J. Lopes, and H. Riechert, "Effect of buffer layer coupling on the lattice parameter of epitaxial graphene on SiC(0001)," *Phys. Rev. B*, vol. 90, no. 4, p. 41 403, 2014.

[106] J. A. Robinson, M. Hollander, M. LaBella, K. A. Trumbull, R. Cavalero, and D. W. Snyder, "Epitaxial graphene transistors: enhancing performance via hydrogen intercalation," *Nano Lett.*, vol. 11, no. 9, pp. 3875–3880, 2011.

[107] L. B. Biedermann, M. L. Bolen, M. A. Capano, D. Zemlyanov, and R. G. Reifenberger, "Insights into few-layer epitaxial graphene growth on $4\mathrm{H}{-}\mathrm{SiC}(000\overline{1})$ substrates from STM studies," *Phys. Rev. B*, vol. 79, no. 12, p. 125 411, 2009.

[108] J van Landuyt, G van Tendeloo, and S Amelinckx, "Electron diffraction patterns of distortion modulated structures," *Phys. Status Solidi A*, vol. 26, no. 1, K9–K11, 1974.

[109] J. Hass, R. Feng, T. Li, X. Li, Z. Zong, W. A. de Heer, P. N. First, E. H. Conrad, C. A. Jeffrey, and C. Berger, "Highly ordered graphene for two dimensional electronics," *Appl. Phys. Lett.*, vol. 89, no. 14, p. 3, 2006.

[110] A. L. Walter, H. Sahin, J. Kang, K.-J. Jeon, A. Bostwick, S. Horzum, L. Moreschini, Y. J. Chang, F. M. Peeters, K. Horn, and E. Rotenberg, "New family of graphene-based organic semiconductors: an investigation of photon-induced electronic structure manipulation in half-fluorinated graphene," *Phys. Rev. B*, vol. 93, no. 7, p. 75 439, 2016.

[111] F. Fromm, M. H. Oliveira Jr, A. Molina-Sánchez, M. Hundhausen, J. M. J. Lopes, H. Riechert, L. Wirtz, and T. Seyller, "Contribution of the buffer layer to the raman spectrum of epitaxial graphene on SiC(0001)," *New J. Phys.*, vol. 15, no. 4, p. 43 031, 2013.

[112] H. Z. Cummins, "Experimental studies of structurally incommensurate crystal phases," *Phys. Rep.*, vol. 185, no. 56, pp. 211–409, 1990.

[113] J. M. Perez-Mato, G. Madariaga, and M. J. Tello, "Diffraction symmetry of incommensurate structures," *J. Phys. C Solid State Phys.*, vol. 19, no. 15, p. 2613, 1986.

[114] G. Trambly de Laissardière, D. Mayou, and L. Magaud, "Localization of dirac electrons in rotated graphene bilayers," *Nano Lett.*, vol. 10, no. 3, pp. 804–808, 2010.

[115] M. Koshino, "Interlayer interaction in general incommensurate atomic layers," *New J. Phys.*, vol. 17, no. 1, p. 015 014, 2015.

[116] M. N. Nair, I. Palacio, A. Celis, A. Zobelli, A. Gloter, S. Kubsky, J.-P. Turmaud, M. Conrad, C. Berger, W. de Heer, E. H. Conrad, A. Taleb-Ibrahimi, and A. Tejeda, "Band gap opening induced by the structural periodicity in epitaxial graphene buffer layer," *Nano Lett.*, 2017.

[117] J. Zabel, R. R. Nair, A. Ott, T. Georgiou, A. K. Geim, K. S. Novoselov, and C. Casiraghi, "Raman spectroscopy of graphene and bilayer under biaxial strain: bubbles and balloons," *Nano Lett.*, vol. 12, no. 2, pp. 617–621, 2012.

[118] F. Speck, J. Jobst, F. Fromm, M. Ostler, D. Waldmann, M. Hundhausen, H. B. Weber, and T. Seyller, "The quasi-free-standing nature of graphene on H-saturated SiC(0001)," *Appl. Phys. Lett.*, vol. 99, no. 12, p. 122 106, 2011.

[119] J. Jobst, D. Waldmann, F. Speck, R. Hirner, D. K. Maude, T. Seyller, and H. B. Weber, "Quantum oscillations and quantum hall effect in epitaxial graphene," *Phys. Rev. B*, vol. 81, no. 19, p. 195 434, 2010.

[120] J. Hicks and E. H. Conrad, "Graphene investigated by synchrotron radiation," *MRS Bull.*, vol. 37, no. 12, pp. 1203–1213, 2012.

[121] M. Rubio-Roy, F. Zaman, Y. Hu, C. Berger, M. W. Moseley, J. D. Meindl, and W. A. de Heer, "Structured epitaxial graphene growth on SiC by selective graphitization using a patterned AlN cap," *Appl. Phys. Lett.*, vol. 96, no. 8, p. 082 112, 2010.

[122] R. Puybaret, J. Hankinson, J. Palmer, C. Bouvier, A. Ougazzaden, P. L. Voss, C. Berger, and W. A. de Heer, "Scalable control of graphene growth on 4H-SiC C-face using decomposing silicon nitride masks," *J. Phys. D Appl. Phys.*, vol. 48, no. 15, p. 152 001, 2015.

[123] P. Bak, "Commensurate phases, incommensurate phases and the devil's staircase," *Rep. Prog. Phys.*, vol. 45, no. 6, p. 587, 1982.

[124] J. Voit, L. Perfetti, F. Zwick, H. Berger, G. Margaritondo, G. Grüner, H. Höchst, and M. Grioni, "Electronic structure of solids with competing periodic potentials," *Science*, vol. 290, no. 5491, pp. 501–503, 2000.

[125] J. B. Sokoloff, "Unusual band structure, wave functions and electrical conductance in crystals with incommensurate periodic potentials," *Phys. Rep.*, vol. 126, no. 4, pp. 189–244, 1985.

[126] ——, "Band structure and localization in incommensurate lattice potentials," *Phys. Rev. B*, vol. 23, no. 12, pp. 6422–6429, 1981.

[127] I. Deretzis, G. Calogero, G. G. N. Angilella, and A. L. Magna, "Role of basis sets on the unfolding of supercell band structures: from tight-binding to density functional theory," *Eur. Lett.*, vol. 107, no. 2, p. 27 006, 2014.

[128] A. L. de Parga, F. Calleja, B. Borca, M. C. G. Passeggi, J. J. Hinarejos, F. Guinea, and R. Miranda, "Periodically rippled graphene: Growth and spatially resolved electronic structure," *Phys. Rev. Lett.*, vol. 100, no. 5, p. 56 807, 2008.

[129] S.-H. Lee, H.-J. Chung, J. Heo, H. Yang, J. Shin, U.-I. Chung, and S. Seo, "Band gap opening by two-dimensional manifestation of peierls instability in graphene," *ACS Nano*, vol. 5, no. 4, pp. 2964–2969, 2011.

[130] K. Okahara, K. Tanaka, H. Aoki, T. Sato, and T. Yamabe, "Band structures of carbon nanotubes with bond-alternation patterns," *Chem. Phys. Lett.*, vol. 219, no. 5, pp. 462–468, 1994.

[131] W. Norimatsu and M. Kusunoki, "Transitional structures of the interface between graphene and 6H-SiC(0001)," *Chem. Phys. Lett.*, vol. 468, no. 13, pp. 52–56, 2009.

[132] J. Sforzini, L. Nemec, T. Denig, B. Stadtmüller, T.-L. Lee, C. Kumpf, S. Soubatch, U. Starke, P. Rinke, V. Blum, F. C. Bocquet, and F. S. Tautz, "Approaching truly freestanding graphene: the structure of hydrogen-intercalated graphene on 6H-SiC(0001)," *Phys. Rev. Lett.*, vol. 114, no. 10, p. 106 804, 2015.

[133] J. D. Emery, Q. H. Wang, M. Zarrouati, P. Fenter, M. C. Hersam, and M. J. Bedzyk, "Structural analysis of PTCDA monolayers on epitaxial graphene with ultra-high vacuum scanning tunneling microscopy and high-resolution x-ray reflectivity," *Surf. Sci.*, vol. 605, no. 17-18, pp. 1685–1693, 2011.

[134] J.-P. Rueff, J. M. Ablett, D. Céolin, D. Prieur, T. Moreno, V. Balédent, B. Lassalle-Kaiser, J. E. Rault, M. Simon, and A. Shukla, "The GALAXIES beamline at the SOLEIL synchrotron: Inelastic x-ray scattering and photoelectron spectroscopy in the hard x-ray range," *J. Synchrotron Radiat.*, vol. 22, no. 1, pp. 175–179, 2015.

[135] J. J. Olivero and R. L. Longbothum, "Empirical fits to the Voigt line width: a brief review," *J. Quant. Spectrosc. Radiat. Transf.*, vol. 17, no. 2, pp. 233–236, 1977.

[136] S. Doniach and M. Sunjic, "Many-electron singularity in x-ray photoemission and x-ray line spectra from metals," *J. Phys. C Solid State Phys.*, vol. 3, no. 2, pp. 285–291, 1970.

[137] J. Kunc, Y. Hu, J. Palmer, C. Berger, and W. A. de Heer, "A method to extract pure raman spectrum of epitaxial graphene on SiC," *Appl. Phys. Lett.*, vol. 103, no. 20, p. 201 911, 2013.

[138] J. Palmer, J. Kunc, Y. Hu, J. Hankinson, Z. Guo, C. Berger, and W. A. de Heer, "Controlled epitaxial graphene growth within removable amorphous carbon corrals," *Appl. Phys. Lett.*, vol. 105, no. 2, p. 23 106, 2014.

[139] Y. Yoneda, "Anomalous surface reflection of x-rays," *Phys. Rev.*, vol. 131, no. 5, pp. 2010–2013, 1963.

[140] I. K. Robinson, "Crystal truncation rods and surface roughness," *Phys. Rev. B*, vol. 33, no. 6, pp. 3830–3836, 1986.

[141] R. Tibshirani, "Regression shrinkage and selection via the lasso," *J. R. Stat. Soc. Ser. B*, vol. 58, no. 1, pp. 267–288, 1996.

[142] F. Ming and A. Zangwill, "Model and simulations of the epitaxial growth of graphene on non-planar 6H-SiC surfaces," *J. Phys. D. Appl. Phys.*, vol. 45, no. 15, p. 154 007, 2012.

[143] ——, "Model for the epitaxial growth of graphene on 6H-SiC(0001)," *Phys. Rev. B*, vol. 84, no. 11, p. 115 459, 2011.

[144] H. Kageshima, H. Hibino, H. Yamaguchi, and M. Nagase, "Stability and reactivity of steps in the initial stage of graphene growth on the SiC(0001) surface," *Phys. Rev. B*, vol. 88, no. 23, p. 235 405, 2013.

[145] ——, "Theoretical study on epitaxial graphene growth by Si sublimation from SiC(0001) surface," *Jpn. J. Appl. Phys.*, vol. 50, no. 9, p. 095 601, 2011.

[146] S. Tanaka, K. Morita, and H. Hibino, "Anisotropic layer-by-layer growth of graphene on vicinal SiC(0001) surfaces," *Phys. Rev. B*, vol. 81, no. 4, p. 41 406, 2010.

[147] S. Kopylov, A. Tzalenchuk, S. Kubatkin, and V. I. Fal'ko, "Charge transfer between epitaxial graphene and silicon carbide," *Appl. Phys. Lett.*, vol. 97, no. 11, p. 112 109, 2010.

[148] S. Y. Zhou, G.-H. Gweon, and A. Lanzara, "Low energy excitations in graphite: the role of dimensionality and lattice defects," *Ann. Phys. (N. Y).*, vol. 321, no. 7, pp. 1730–1746, 2006.

[149] K. V. Emtsev, A. A. Zakharov, C. Coletti, S. Forti, and U. Starke, "Ambipolar doping in quasifree epitaxial graphene on SiC(0001) controlled by Ge intercalation," *Phys. Rev. B*, vol. 84, no. 12, p. 125 423, 2011.

[150] I. Gierz, T. Suzuki, R. T. Weitz, D. S. Lee, B. Krauss, C. Riedl, U. Starke, H. Höchst, J. H. Smet, C. R. Ast, and K. Kern, "Electronic decoupling of an epitaxial graphene monolayer by gold intercalation," *Phys. Rev. B*, vol. 81, no. 23, p. 235 408, 2010.

[151] C. Xia, S. Watcharinyanon, A. A. Zakharov, R. Yakimova, L. Hultman, L. I. Johansson, and C. Virojanadara, "Si intercalation/deintercalation of graphene on 6H-SiC(0001)," *Phys. Rev. B*, vol. 85, no. 4, p. 45 418, 2012.

[152] M. G. Silly, M. D'Angelo, A. Besson, Y. J. Dappe, S. Kubsky, G. Li, F. Nicolas, D. Pierucci, and M. Thomasset, "Electronic and structural properties of graphene-based metal-semiconducting heterostructures engineered by silicon intercalation," *Carbon N. Y.*, vol. 76, pp. 27–39, 2014.